IMPERIAL COLLEGE OF SCIENCE, TECHNOLOGY AND MEDICINE

UNIVERSITY OF LONDON

DETERMINATION OF MATERIAL PROPERTIES USING GUIDED WAVES

by

Thomas Karl Vogt

A thesis submitted to the University of London for the degree of

Doctor of Philosophy

Department of Mechanical Engineering

Imperial College of Science, Technology and Medicine

London SW7 2BX

October 2002

Abstract

The thesis examines the possibility of using an ultrasonic guided wave system for the determination of material properties. The system considered consists of a cylindrical waveguide which is partly embedded in another material whose acoustic properties are to be determined. Two main ideas are investigated.

The first idea is based on the fact that, when a waveguide is embedded in another material, a guided wave in the waveguide will be attenuated due to the leakage of bulk waves into the surrounding material. The rate of leakage depends on both the material properties of the waveguide and the embedding material. The propagation characteristics such as the phase velocity and the attenuation can be predicted using software that has been developed in the laboratory as part of previous investigations. With these predictions it is possible to relate a measured attenuation to material properties such as the viscosity of a liquid. Experimental results show the validity of these predictions.

The second idea uses the fact that, when the waveguide enters the material under investigation, the guided wave will be scattered at the entry point due to the change in surface impedance. Since the magnitude of the reflected guided wave depends on the properties of the embedding material, it can in principle be used for materials characterisation. Finite Element (FE) modelling and a theoretical scattering analysis have been carried out in order to calculate reflection coefficients for different material properties. Both these methods agree very well with each other and with experimental results.

As one of the possible applications, the cure monitoring of epoxy resins has been investigated in more detail. Both methods have been successfully applied to the monitoring of bulk samples, yielding accurate quantitative results of epoxy shear velocity. For the monitoring of adhesive cure in automotive joints, the reflection coefficient method seems most suitable. However, it was found that the geometry of the joints influences the reflection of guided waves. This effect has been investigated using FE modelling. In this case, due to the uncertainty of the geometry in the industrial environment, the reflection coefficient can be determined only qualitatively.

Acknowledgements

I would like to sincerely thank my supervisors, Mike Lowe and Peter Cawley, for their invaluable guidance and support during my work. Also, I would like to acknowledge the input of the current and former members of the NDT group. Much in this thesis is based on their previous work and experience, which they were always willing to discuss in detail.

I also thoroughly enjoyed working with Marion Unwin and Richard Challis from the University of Nottingham, and thank them for their co-operation.

Furthermore, I must acknowledge the Engineering and Physical Sciences Research Council (EPSRC), which has funded this work, and Ford Motor Company and Jaguar Cars Limited for their collaboration in this project.

Finally, I would like to express personal thanks to my family and of course to Carola for their encouragement and support throughout my studies.

Contents

List of Figures

List of Tables

Nomenclature

a	amplitude of incident mode (Q-normalised)
A	amplitude, amplitude of incident mode (P-normalised)
A_1	shape factor
$\mathbf{A}$	vector potential
α	attenuation
α_η	viscosity-induced attenuation
b	amplitude of scattered mode (Q-normalised)
B	amplitude of scattered mode (P-normalised)
c_E	bar velocity
c_{gr}	group velocity
c_l	longitudinal bulk velocity
c_{ph}	phase velocity
c_s	shear bulk velocity
d	joint thickness
δ	meniscus angle
Δx	element length (Finite Element)
Δt	time step (Finite Element)
e	total energy density
E	Young's modulus, total energy
ε	strain, error
η	dynamic shear viscosity
f	frequency
$[\mathbf{G}]$	global matrix
H	magnetic field
i	$\sqrt{-1}$, imaginary unit
I	electric current
$\mathbf{I}$	identity matrix
k	complex wavenumber

continued on next page

continued from previous page

L, l	length
λ	wavelength, Lamé constant
λ'	viscous Lamé constant
M, $\mathbf{M}$	magnetization
μ	Lamé constant, angular wavenumber
μ'	viscous Lamé constant
ν	Poisson's ratio, angular wavenumber
ω	circular frequency
p	power flow density
P	average power flow
ϕ	scalar potential
Q	see definition of Eq. (5.15)
r	radius
R	radius, reflection coefficient
ρ	density
ρ_f	density of fluid
ρ_s	density of solid
S	surface, scattering parameter, sensitivity
t	time
T	absolute temperature, stress, transmission coefficient, time
$\mathbf{T}$	stress tensor
ϑ	leakage angle
u, $\mathbf{u}$	displacement
V	volume
ξ	real part of the wavenumber in the axial direction (for guided waves)

Chapter 1

Introduction

1.1 Motivation

There is both a practical and a scientific interest in developing a technique for the measurement of material properties based on ultrasonic guided waves.

The initial motivation for the practical aspect of such a technique comes from automotive industry, where adhesive joining of metal structures is becoming increasingly popular [1]. This is due to the fact that adhesively joined structures exhibit a higher structural integrity compared to riveted or spot welded ones. Other advantages include reduced weight, improved corrosion performance and broader design possibilities. Especially in cases where safety-critical structures are involved, this requires the correct choice and cure of the adhesive. However, controlling the cure process of adhesive bonds in large metal structures can be difficult because of temperature variations in the cure ovens and the sensitivity of adhesive cure to temperature. A measurement technique is therefore needed to monitor and assess the progress of cure in industrial environments. Such a technique would not only be useful in development stages but also as an online spot check technique during car manufacture.

The photograph in Fig. 1.1 shows the inside of a car boot, and arrows indicate as an example a joint which needs to be monitored. It can be seen that in general spot welding or riveting is used together with the adhesive, which is mainly due to the fact that, before cure, the adhesive cannot keep the different metal structures

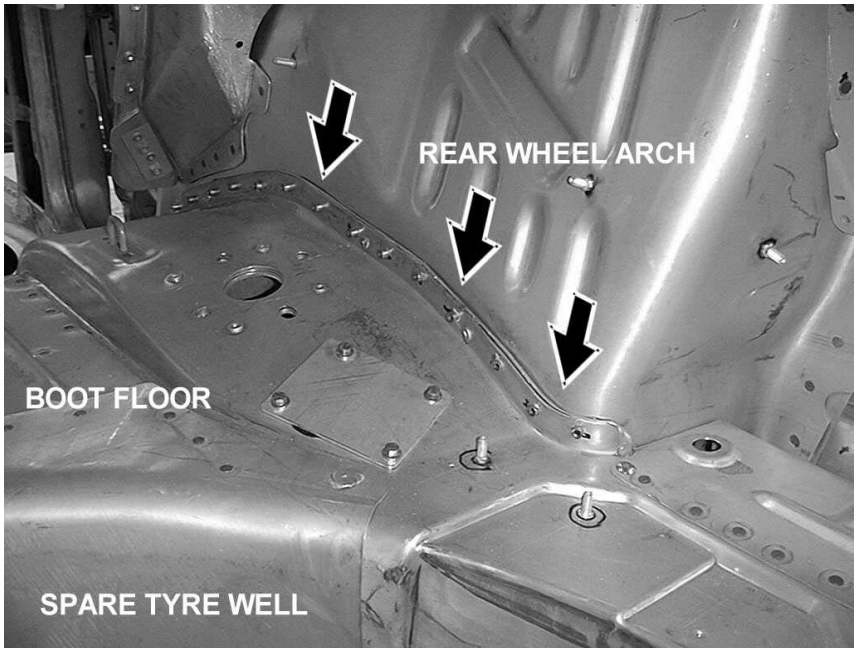

Figure 1.1: Photograph of the interior of a car boot. The arrows indicate an example of an adhesive joint.

together. There are a number of cure monitoring techniques available, which will be reviewed in Sec. 6.2. However, these are not suitable in this particular application due to the limited accessibility of the joints and due to oven temperatures as high as 200 °C.

The idea investigated in this thesis is to use a wire waveguide which is partly embedded in the adhesive. A wire waveguide is preferred over, for example, a strip waveguide because reflections from the edges of the strip may interfere with the guided wave of interest and can thus complicate the analysis. Characteristically, the bond-lines are approximately 0.2–1 mm thick and 20 mm wide, which restricts the radius of the waveguide and the embedded length. An ultrasonic guided wave is excited by a transducer at the free end of the wire, and propagates along the wire. Where the wire is embedded, the guided wave will interact with the adhesive in a characteristic way, depending on the material properties of the adhesive. Thus, the wire can be used as a sensor for material properties. Due to the long range propagation characteristics of guided waves, it is possible to place the testing equipment including the transducer outside the oven. A steel waveguide is chosen because of

the availability of the material and its low intrinsic attenuation. Glass waveguides may also be used (see, for example, [2]), however, steel waveguides were considered more robust for the industrial application.

The physical and chemical processes occurring during the cure of epoxy resins are still not fully understood. A guided wave technique, which could be used in conjunction with other existing techniques to research these processes, would present a significant contribution in the effort to complete the understanding of cure processes. For example, with conventional ultrasonic bulk wave techniques it is often not possible to determine the shear properties of an epoxy resin in the very early stages of cure because of high bulk shear attenuation [3]. Due to the different measurement principles characteristic to the waveguide techniques, which will be introduced below, it is possible to estimate the state of cure during the entire cure cycle, including the interval at the onset of cure where conventional bulk wave techniques fail.

The use of such instrumentation is not just limited to the cure monitoring of epoxy resins, but has a much wider applicability for the measurement of the acoustic properties of materials in general. A very interesting prospect is the use of the guided wave technique where conventional ultrasonic bulk wave techniques fail. As an example, the measurement of the bulk longitudinal and shear velocity in wet sands was realised by Long *et al.* [4] using the waveguide technique presented in this thesis. Other applications include the use for industrial process monitoring of liquids and for viscometric studies.

This investigation is therefore concerned with the development of measurement techniques for the determination of material properties using ultrasonic guided waves in wires. The aim of this work can be summarised in the following objectives:

- to identify suitable waveguide techniques for the measurement of material properties,
- to apply existing and develop new modelling techniques to relate the results from measurements to actual material properties,

– to experimentally verify the validity of the modelling techniques, and

– to apply these waveguide techniques to the cure monitoring of epoxy resins.

1.2 Background

An embedding material affects the propagation of a guided wave in several ways which can be used to determine its material properties, and they will be reviewed thoroughly in Sec. 4.2. Two techniques are examined in detail in this work.

The first method is based on the fact that, when the waveguide is embedded in another medium, the guided wave will be attenuated due to the leakage of bulk waves into the surrounding material (see schematic in Fig. 1.2). The rate of leakage depends both on the material properties of the waveguide and the embedding material. As a general rule of thumb, the higher the impedance mismatch between the two materials, the lower is the attenuation. The attenuation also depends on the waveguide mode and on the frequency. The existing modelling tool DISPERSE [5, 6], which was developed in the NDT laboratory at Imperial College, can be used to relate the material properties of the waveguide and the embedding medium to the attenuation of a guided mode. Thus, if the material properties of the waveguide are known, the measurement of attenuation allows for the prediction of the material properties of the surrounding material. In the following, this method will be referred to as the "attenuation method".

The second method is based on the fact that a guided wave is partly reflected from the point where the free waveguide enters into another medium due to the change in surface impedance (see Fig. 1.3). In the following, this reflection is referred to as the "entry reflection". As a general rule of thumb in this case, the higher the change in surface impedance, the larger is the magnitude of the entry reflection. Like the attenuation, the magnitude of the entry reflection also depends on the waveguide mode and the frequency. The prediction of the entry reflection is not as straightforward as for the attenuation method. Finite Element (FE) modelling

presents a powerful tool, however, the computational analysis can be tedious. In an alternative approach, the entry reflection coefficient can be calculated using a modal scattering analysis, whose theoretical foundations are developed in the thesis. This is much more efficient than FE modelling, especially where a small element size and time step would be required due to low velocities in the embedding material. The numerical implementation of the modal analysis can be used to relate the reflection coefficient to the material properties of the embedding medium. Therefore, the measurement of the reflection coefficient allows for the prediction of the properties of the embedding medium. This method will be referred to as the "reflection method".

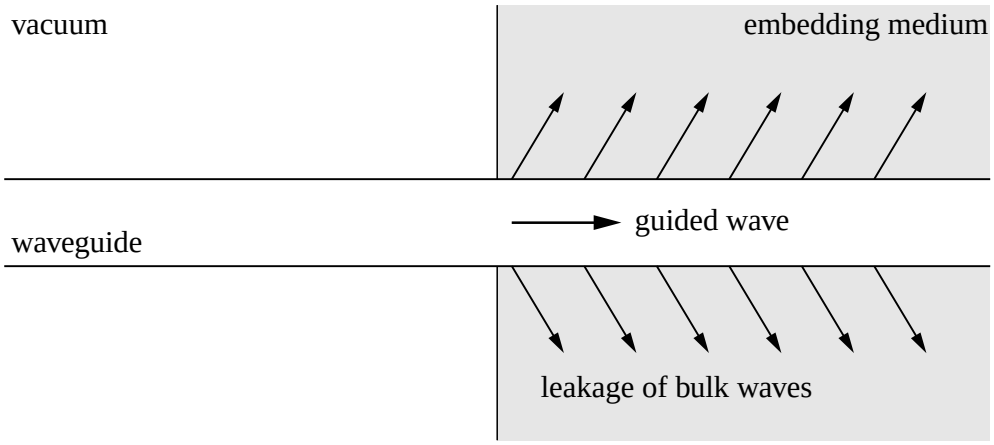

Figure 1.2: Schematic of the process of guided wave attenuation due to the leakage of bulk waves into the medium surrounding the waveguide.

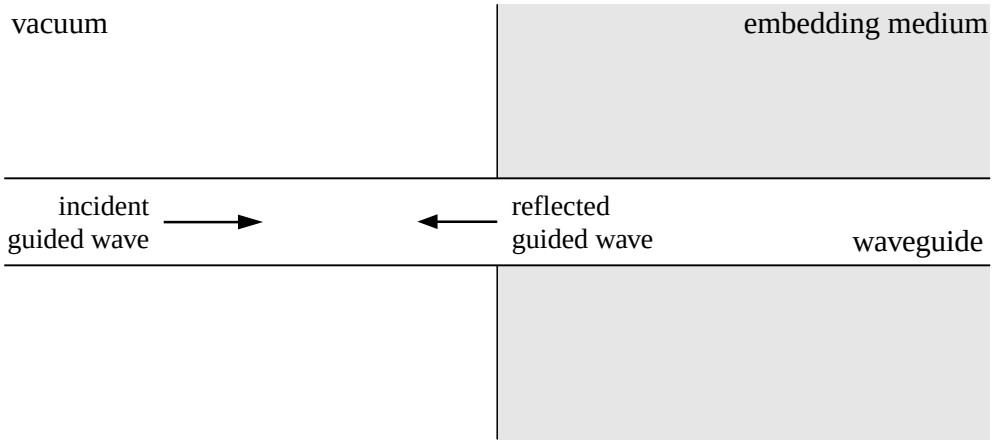

Figure 1.3: Schematic of the process of guided wave reflection from a change in surface impedance.

1.3 Outline of Thesis

The thesis is divided into several chapters. Due to the diverse nature of the topics covered by each chapter, relevant literature is reviewed separately at the beginning of each chapter. In the following, the figures belonging to a particular chapter will be placed at the end of that chapter. Subsequent to the introductory remarks in this chapter, the thesis is structured in the following way.

Chapter 2 reviews the basic theory of bulk waves and guided waves in cylindrical structures and introduces the necessary notations. Since this is well documented in literature, it will be restricted to explanations which are essential for the understanding of the remaining chapters. On the basis of the properties of guided modes presented in that chapter, a choice of the suitable modes for the testing techniques is made.

Chapter 3 introduces experimental techniques which are used throughout the thesis. This includes a description of the transduction mechanisms to excite guided waves in wires and the typical experimental set-up. For accurate predictions it is necessary to know the material properties of the waveguide. The basic measurement techniques to determine these properties are outlined.

The following chapter explains in detail the attenuation method. The main modelling tool used for the predictions is the software DISPERSE, and using this tool the method is validated experimentally. As an example, the testing procedures to determine the shear velocity of viscous liquids are set out. These testing techniques are designed to be also applicable to the cure monitoring of epoxy resins.

As explained in Sec. 1.2, the modelling of the entry reflection coefficient is realised by a modal scattering analysis. The theoretical foundations and its numerical implementation are developed in Ch. 5. This analysis is validated experimentally and by FE modelling. Keeping the initial motivation to monitor the cure of epoxy resins in mind, the examples given concentrate on the cases where a steel waveguide is partly embedded in an epoxy resin.

In Ch. 6, the attenuation and reflection methods are applied to the cure monitoring of bulk samples of epoxy resin. A review of existing cure monitoring methods is given, and the applicability of the wire waveguide methods is discussed. The theoretical predictions are experimentally verified for both the attenuation and the reflection method.

Finally, with respect to the cure monitoring application in joints, Ch. 7 examines the dependence of the entry reflection coefficient on the geometry of the adhesive joint. The geometrical features of a meniscus, which may occur when the wire enters the adhesive, and the thickness of the bond-line are studied using two- and three-dimensional FE modelling.

The thesis concludes with a summary of the work undertaken and an outlook for possible further research.

Chapter 2

Guided Waves in Cylindrical Structures

2.1 Background

The aim of this chapter is to introduce fundamental concepts of acoustic wave propagation in cylindrical structures. In an unbounded, infinite, elastic medium, acoustic waves can either propagate as homogeneous or inhomogeneous bulk shear and longitudinal waves. In bounded media such as wires, plates and pipes, different modes of guided waves can propagate which can be thought of as a superposition of these bulk wave solutions of the unbounded medium. Especially in the case where the waveguide is embedded in another medium, inhomogeneous bulk waves play an important role in the process of guided wave propagation. Characteristic features of guided modes in cylindrical structures such as their dependence on the frequency, called dispersion, and the radial distribution of the field variables over the cross-section of the waveguide, called the mode shape, are discussed.

2.2 Wave Propagation in Infinite Media

The theory of wave propagation in unbounded, isotropic media is well documented in many textbooks (see, for example, [7, 8, 9, 10, 11, 12]) and is therefore only outlined briefly in this section. However, it is necessary to introduce notation and some characteristics which are needed later for the understanding of wave propagation in

waveguides.

Starting with the equation of motion, the particle displacement $\mathbf{u}$ in a material of density ρ is related to the stress tensor $\mathbf{T}$ by

$$\rho\frac{\partial^2\mathbf{u}}{\partial t^2} = \nabla\cdot\mathbf{T} \tag{2.1}$$

(see, for example, [8]). Here, body forces such as gravity are neglected. Furthermore, for small stresses, Hooke's law states that, in an isotropic elastic medium, the displacements are linearly related to the stress according to the following relationship:

$$\mathbf{T} = \lambda\mathbf{I}\nabla\cdot\mathbf{u} + \mu(\nabla\mathbf{u} + \mathbf{u}\nabla), \tag{2.2}$$

where λ and μ are the Lamé constants and $\mathbf{I}$ is the identity matrix. Combining these two equations gives a single equation for the displacement, $\mathbf{u}$:

$$\rho\frac{\partial^2\mathbf{u}}{\partial t^2} = (\lambda+2\mu)\nabla(\nabla\cdot\mathbf{u}) + \mu\nabla\times(\nabla\times\mathbf{u}). \tag{2.3}$$

The Helmholtz decomposition [13], which states that any vector can be written in terms of a scalar potential, ϕ, and a vector potential, $\mathbf{A}$, is used to derive the standard wave equations:

$$\mathbf{u} = \nabla\phi + \nabla\times\mathbf{A}. \tag{2.4}$$

This expression is substituted into Eq. (2.3), which, after some algebra, becomes:

$$\nabla\left[\rho\frac{\partial^2\phi}{\partial t^2} - (\lambda+2\mu)\nabla^2\phi\right] + \nabla\times\left[\rho\frac{\partial^2\mathbf{A}}{\partial t^2} - \mu\nabla^2\mathbf{A}\right] = 0, \tag{2.5}$$

where ∇^2 is the three-dimensional Laplace operator. This equation is fulfilled if both terms in the brackets vanish, and therefore

$$\frac{\partial^2\phi}{\partial t^2} = c_l^2\nabla^2\phi \qquad \text{and} \qquad \frac{\partial^2\mathbf{A}}{\partial t^2} = c_s^2\nabla^2\mathbf{A}. \tag{2.6}$$

These are the wave equations, with the constants c_l and c_s being the bulk velocities of longitudinal and shear waves, respectively. In an elastic isotropic medium, they are real valued:

$$c_l = \sqrt{\frac{\lambda+2\mu}{\rho}} \qquad \text{and} \qquad c_s = \sqrt{\frac{\mu}{\rho}}. \tag{2.7}$$

Solutions to the wave equations in (2.6) are sought in the form $e^{-i(\mathbf{kr}-\omega t)}$, where $\mathbf{k}$ is the wavenumber, ω is the circular frequency, and $\mathbf{r}$ is the coordinate vector. It follows that

$$\mathbf{k}^2 = \frac{\omega^2}{c^2}, \tag{2.8}$$

where c stands for either the longitudinal bulk velocity, c_l, or the shear bulk velocity, c_s. Note that in this case the right hand side of this equation is pure real. However, the wavenumber, $\mathbf{k}$, can in general be complex:

$$\mathbf{k} = \mathbf{k}_{\mathrm{re}} + i\mathbf{k}_{\mathrm{im}}, \tag{2.9}$$

where $\mathbf{k}_{\mathrm{re}}$ and $\mathbf{k}_{\mathrm{im}}$ are the real and the imaginary part of the wavenumber, respectively. Equation (2.8) can thus be written as

$$\mathbf{k}_{\mathrm{re}}^2 + 2i\mathbf{k}_{\mathrm{re}}\mathbf{k}_{\mathrm{im}} - \mathbf{k}_{\mathrm{im}}^2 = \frac{\omega^2}{c^2}. \tag{2.10}$$

It therefore follows that the real part of the wavenumber must be orthogonal to the imaginary part:

$$\mathbf{k}_{\mathrm{re}}\mathbf{k}_{\mathrm{im}} = 0. \tag{2.11}$$

The real part of the wavenumber represents the phase propagation, and the phase velocity c_{ph}, which is the speed at which the wave crests propagate, is defined as

$$k_{\mathrm{re}} = \frac{\omega}{c_{ph}}. \tag{2.12}$$

The imaginary part on the other hand represents a spatial attenuation. Of course, since the medium is assumed to be elastic, there can be no attenuation in the direction of propagation, however, the fields may decay in the direction normal to the direction of propagation. When $\mathbf{k}_{\mathrm{im}} = 0$, the equation simplifies to

$$k_{\mathrm{re}} = \frac{\omega}{c}. \tag{2.13}$$

In this case, the bulk velocity equals the phase velocity, and the wave is said to be *homogeneous*. This is not the case when $\mathbf{k}_{\mathrm{im}} \neq 0$, since then

$$k_{\mathrm{re}}^2 - k_{\mathrm{im}}^2 = \frac{\omega^2}{c^2}, \tag{2.14}$$

and the phase velocity is smaller than the bulk velocity. These waves are called *inhomogeneous* [14].

So far, the material has been modelled as elastic. In order to model viscoelastic materials, the hysteretic damping model is adopted [15]. For time harmonic propagation with $e^{i\omega t}$, an imaginary component is added to the real Lamé constants, and the longitudinal and shear bulk velocities are now given by the complex expressions

$$c_l = \sqrt{\frac{(\lambda + 2\mu) + i(\lambda' + 2\mu')}{\rho}} \qquad \text{and} \qquad c_s = \sqrt{\frac{\mu + i\mu'}{\rho}}, \tag{2.15}$$

where λ' and μ' are the viscous constants of the material. As an example, the special case of a viscous liquid is discussed in Sec. 4.3.

2.3 Wave Propagation in Free Waveguides

2.3.1 Guided waves

Guided wave propagation in cylindrical structures has been treated by many researchers (see, for example, [16, 17, 18, 19, 20, 21, 22]), and only a brief overview is given here. The waveguides used in this work are wires, and therefore the treatment of guided wave propagation will be limited in the following to solid cylinders. Nevertheless, many of the features of guided waves are of a general nature which are similar in other structures. Time harmonic propagation in the direction of the axis of the waveguide is considered, which is chosen to be the z-direction in the cylindrical coordinate system (r,Θ,z).

A guided wave is characterised by its generally complex wavenumber in the direction of propagation, $k = \xi - i\alpha$, or, alternatively, by its phase velocity, c_{ph}, and attenuation, α. In general, these quantities depend on the frequency f, and this relationship is referred to as *dispersion*. A guided wave can be thought of as a superposition of partial bulk waves which are reflected within the waveguide boundaries (see, for example, [8], p. 78). At the boundary to another medium, these waves have to fulfill boundary conditions, where Snell's law must be obeyed [13]. According to this law,

the wavenumber component of the guided wave in the z-direction, k, must be equal to the z-component of the wavenumber of the partial wave, k'_z:

$$k = k'_z. \tag{2.16}$$

Also the frequency, f, must be the same for all waves at the interface. In a free waveguide surrounded by vacuum, the stresses normal to the waveguide surface must be zero. It follows that all the bulk waves are totally reflected within the waveguide, and the guided wave is attenuated due to intrinsic losses of the waveguide material only. Thus, in a perfectly elastic free wire, the attenuation of a guided wave is zero, and the wave is fully characterised by its phase velocity dispersion relationship. An exception to this are the non-propagating and inhomogeneous waveguide modes, which are discussed in detail in Sec. 5.2.3 and in App. A.

The waveguide can of course consist of a number of layers itself. In order to find the acoustic parameters of guided waves for arbitrary multilayered systems, a general purpose software tool, DISPERSE, was developed in the laboratory. This work was started by Lowe [15] to model guided wave propagation in multilayered embedded plates and cylindrical structures in vacuum, and was further extended to model multilayered embedded cylindrical systems by Pavlakovic [5].

With the information about the geometrical and mechanical parameters in a multilayered waveguide in vacuum, the displacements and stresses can be expressed in terms of the amplitudes of all the partial bulk waves that can exist in each layer. Combining these with the boundary conditions at each interface, DISPERSE assembles a global matrix, $[\mathbf{G}]$, which relates the partial wave amplitudes to the physical constraints of the whole system, and solves

$$[\mathbf{G}]\{A\} = 0, \tag{2.17}$$

where $\{A\}$ is a vector of the partial wave amplitudes. The above equation is satisfied when the determinant of the global matrix vanishes, and solutions are sought in the complex wavenumber - frequency space. Roots occur for distinctive combinations of complex wavenumber in the axial direction, k, and frequency, f. Those roots that

connect together to a line - a dispersion curve - are found to belong to a specific mode of propagation.

More precisely, a guided wave in a cylinder or wire can be described by general expressions for the field variables such as stresses and displacements. For example, the displacement field, $\mathbf{u}$, of a guided wave can be written as

$$\mathbf{u}(r, \Theta, z, t) = \mathbf{u}(r) e^{i\nu\Theta} e^{-i(kz-\omega t)}, \tag{2.18}$$

where $\omega = 2\pi f$ is the circular frequency, ν is the angular wavenumber, and $\mathbf{u}(r)$ is a radial distribution function characteristic to each mode (see Sec. 2.3.3). Since only propagation in the direction of the axis of the cylinder is considered, and the field variables such as displacements and stresses must be continuous in the angular direction, ν must be a whole number. It is commonly referred to as the circumferential order.

2.3.2 Dispersion Curves

Three different families of modes are present in wire waveguides: longitudinal, torsional, and flexural modes. Each family of modes itself comprises an infinite number of modes. The modal fields of longitudinal and torsional modes are axi-symmetric, which means that the angular wavenumber is zero. For flexural modes, $\nu \geq 1$.

As an example, Fig. 2.1 shows the phase velocity dispersion curves in a steel wire surrounded by vacuum as predicted with DISPERSE. The material properties for steel are given in Tab. 2.1. The mode naming convention in this thesis follows the one laid out by Silk and Bainton [23]. Longitudinal and torsional modes are denoted according to the convention L(0,n) and T(0,n), respectively. In this notation, the first number indicates the circumferential order, being zero for both longitudinal and torsional modes, whereas the second number is a counter in order to distinguish between the modes of one family. Flexural modes are abbreviated according to the notation F(ν,n).

For elastic wire waveguides, the dispersion curves depend on the product of frequency

Table 2.1: Material parameters used for the analysis in Ch. 2.

Material	c_l [m/s]	c_s [m/s]	ρ [kg/m^3]
Steel	5960	3260	7932
Water	1480	-	1000

and the radius of the waveguide. This means that, for example, the phase velocity in a 1 mm radius wire at a certain frequency is the same as in a 2 mm radius wire at half that frequency.

Since the phase velocity in general depends on the frequency, a wave packet which propagates along the waveguide will not retain its original shape [24]. The further it propagates, the more it will disperse out. Therefore, for long range testing, it is convenient to work with modes that show no or only little dispersion.

2.3.3 Mode Shapes

The fields of every mode have a characteristic radial distribution function, referred to as the mode shape. The different mode families are best distinguished by considering the components of their displacement mode shape $\mathbf{u}(r) = (u_r, u_\Theta, u_z)(r)$:

– longitudinal (L) modes: $u_r, u_z \neq 0$ and $u_\Theta = 0$,
– torsional (T) modes: $u_r, u_z = 0$ and $u_\Theta \neq 0$,
– flexural (F) modes: $u_r, u_\Theta, u_z \neq 0$.

All mode shape predictions are also made using DISPERSE. Figure 2.2(a) shows as an example the displacement mode shape of T(0,1) in a steel wire at a frequency-radius product of 0.1 MHz mm. It exhibits shear displacements in the angular direction only, and propagates at the bulk shear velocity of the waveguide. The mode shape of L(0,1) at this frequency-radius product however is dominated by the axial displacements; there is only little displacement in the radial direction, and no displacement in the angular direction (see Fig. 2.2(b)). In the low frequency-radius

limit, this mode approaches the bar velocity (see also Sec. 3.4.2).

2.4 Wave Propagation in Embedded Waveguides

2.4.1 Leaky guided waves

As mentioned before, a guided wave can be thought of as a superposition of partial bulk waves which are reflected within the waveguide boundaries. Total reflection occurs when the waveguide is surrounded by vacuum. However, if the waveguide is surrounded by another medium, which extends infinitely in the radial direction, the partial waves may also be transmitted across the interface. Thus, bulk waves are excited in the embedding medium, radiating away from the waveguide. Thereby, energy is carried away, and consequently the guided wave, which is propagating in the axial direction, is attenuated.

When leakage occurs, Snell's law not only determines the leakage angle, ϑ, via the relationship

$$\xi = |\mathbf{k}'_{\mathrm{re}}| \sin \vartheta, \tag{2.19}$$

where ξ is the real wavenumber of the guided wave (see Fig. 2.3), and $\mathbf{k}'$ is the wavenumber of the leaky partial wave, but also requires the radiating bulk waves to be inhomogeneous. According to Snell's law, both the real and the imaginary part of the wavenumber component in the axial direction of the leaking bulk wave must be equal to that of the guided wave. The fact that, in an elastic medium, the attenuation of the bulk wave must be normal to the direction of propagation, results in an imaginary wavenumber component in the outward radial direction. This is explained in detail in Sec. 5.3.4, where its implications on waveguide orthogonality are discussed.

However, the guided wave can be non-leaky, that means it is not attenuated even if the waveguide is surrounded by another medium. This is the case when the phase velocity of the guided wave is lower than any of the bulk velocities in the embedding medium. Then, the bulk waves propagate parallel to the interface, that means the

real part of the wavenumber is purely in the z-direction, and form part of the guided wave. With the condition that the energy of the guided wave must be finite, the fields in the embedding material decay in the outward radial direction, so the energy is trapped close to the waveguide surface. Examples for these types of waves are interface waves such as the Scholte wave (see, for example, [25, 11], and also App. B). However, in the applications discussed in this paper, the guided wave will always be leaky.

The rate of leakage depends on both the material properties of the waveguide and the embedding material. As a general rule of thumb, the smaller the difference in the acoustic impedances of the materials, the higher is the attenuation due to the larger transmission coefficient of the partial bulk waves across the interface. On the other hand, if the difference in the acoustic impedance is large, the attenuation will be small. For this reason, the attenuation of, for example, a steel wire surrounded by air is negligible and the system can, to a very good approximation, be modelled as a steel wire being surrounded by vacuum. Also note that, if the embedding material is an ideal liquid, only longitudinal waves may be radiated, whereas if it is a solid, both longitudinal and shear bulk waves may be radiated.

2.4.2 Dispersion Curves

Figure 2.4 shows as an example the phase velocity and attenuation dispersion curves for a steel bar embedded in water. For clarity, only the fundamental modes are shown. The material properties for this analysis are given in Tab. 2.1.

It has been mentioned before that, if the waveguide and the embedding material are elastic, the phase velocity dispersion curves for solid cylinders scale with the product of frequency and the radius of the wire. Moreover, at a particular frequency-radius product, the dispersion curves also scale with the product of attenuation and radius. For example, the guided wave attenuation for a 1 mm radius steel wire immersed in water at a certain frequency is exactly twice as high than that for a 2 mm radius steel wire at half that frequency.

In this example, water is modelled as an ideal or non-viscous liquid. Therefore, only longitudinal bulk waves radiate from the steel bar into the water. It can be seen that the attenuation of the lowest order longitudinal mode, L(0,1), at low frequencies is very small and increases at higher frequencies. The fundamental torsional mode, T(0,1), is not attenuated at all. The reason for this is best understood by considering the mode shapes.

2.4.3 Mode Shapes

In order to explain the physics behind the process of leakage, the mode shapes for the torsional mode, T(0,1), and the longitudinal mode, L(0,1), for a steel bar embedded in water at the frequency-radius products of 0.1 MHz mm are given in Fig. 2.5(a) and (b). Additionally, the mode shape of L(0,1) at 0.5 MHz mm is plotted in Fig. 2.5(c). The half-space occupied by the water has been arbitrarily truncated at a distance equal to three times the radius of the waveguide.

It can be seen that for the torsional mode the displacements in water are exactly zero. This is due to the fact that the modal displacements on the surface of the waveguide are entirely in the angular direction, which are in-plane displacements. Since the embedding water does not support shear stresses, the surface displacements do not couple into the water, and leakage cannot occur. For this reason, the attenuation of T(0,1) in non-viscous liquids is zero. The case where the embedding liquid has shear viscosity is discussed in detail in Ch. 4.

The longitudinal mode, however, has surface displacements in the radial direction, i.e. an out-of-plane component. These displacements do couple into the water and excite longitudinal bulk waves which radiate and cause the mode to be attenuated. In the zero frequency limit, the radial displacements vanish and there are only axial displacements. Therefore the attenuation tends to zero in this limit since the axial in-plane displacements do not couple into the water. At higher frequencies, the ratio between radial to axial displacements increases, so that also the attenuation increases. It should be noted that the undulating displacements in the water arise from the phase relations of the leaking waves, which are originating at different axial

positions along the waveguide.

In general, it can be said that, if there are only in-plane displacements on the surface of the waveguide, attenuation is entirely caused by shear leakage. If there are both in-plane and out-of-plane displacements, both longitudinal and shear leakage contributes to the attenuation.

2.5 Choice of waveguide modes for testing

On the basis of the properties of guided waves that have been presented in this chapter, a choice can be made as to which modes are most suitable for measuring material properties, always also having in mind the industrial application to the cure monitoring of epoxy resins in joints.

Firstly, the presence of numerous waveguide modes in the experiment complicates the analysis because signals from different modes might interfere. In an application where thin wires are used, these cannot be separated by methods which are used for example in pipe testing, where an array of transducers is used to separate modes according to their characteristic mode shapes [26] (see also Sec. 3.2). For this reason, it is preferable to work with fundamental modes at frequencies where no other propagating modes of higher order are present, even though there are high frequency applications where this is not a problem (see, for example, [27, 28]). This greatly simplifies the interpretation of a received time trace. Therefore, only the fundamental modes T(0,1), L(0,1), and F(1,1) are considered further.

Secondly, the effect of dispersion has to be kept as small as possible, especially in an application where long range testing is necessary. An ultrasonic pulse which is dispersed out too much may not have sufficient amplitude compared to the background noise to give reliable results. In this respect, the torsional mode, T(0,1), is most suitable, because it shows no dispersion at all, but also the longitudinal mode, L(0,1), shows very little dispersion at low frequencies and can therefore be used for these purposes.

Thirdly, the excitability of waveguide modes in thin wires has to be considered. As will be discussed in Sec. 3.2, the possibilities are in this case limited to the fundamental modes. The excitation of the longitudinal and the torsional modes can be achieved easily using magnetostrictive transduction, which is a non-contact excitation method. Additionally, longitudinal modes can be excited using piezoelectric transducers.

Having narrowed down the number of suitable waveguide modes in wires to the fundamental longitudinal and torsional modes, it is important to check whether these modes are sensitive to any of the properties of an embedding material. This is discussed in Ch. 4 and Ch. 5.

2.6 Summary

Some fundamental theory behind the propagation of bulk waves in unbounded media and of guided waves in cylindrical structures has been presented.

In an elastic, isotropic material, there are two modes of propagation: longitudinal and shear waves. These waves may be homogeneous, in which case the wavenumber is purely real, or they may be inhomogeneous. Then, the wavenumber is complex, but in addition, the real part of the wavenumber must be normal to its imaginary part.

In a cylinder, there are three types of guided modes: longitudinal, torsional, and flexural. Of each type there is an infinite number of modes, which in general are characterised by a complex wavenumber which depends on the frequency. Each mode has a characteristic radial distribution function which is called its mode shape. When the waveguide is embedded in another medium, the guided wave may be attenuated, the rate of attenuation depending on the material properties of the waveguide and the embedding material, the waveguide geometry, the waveguide mode, and the frequency.

For the applications investigated in this thesis, the fundamental longitudinal and torsional waveguide modes in cylinders have been identified as most suitable. This is because of the practical issues such as the difficulty of interpreting data when many modes are present, the excitability of waveguide modes, and dispersion.

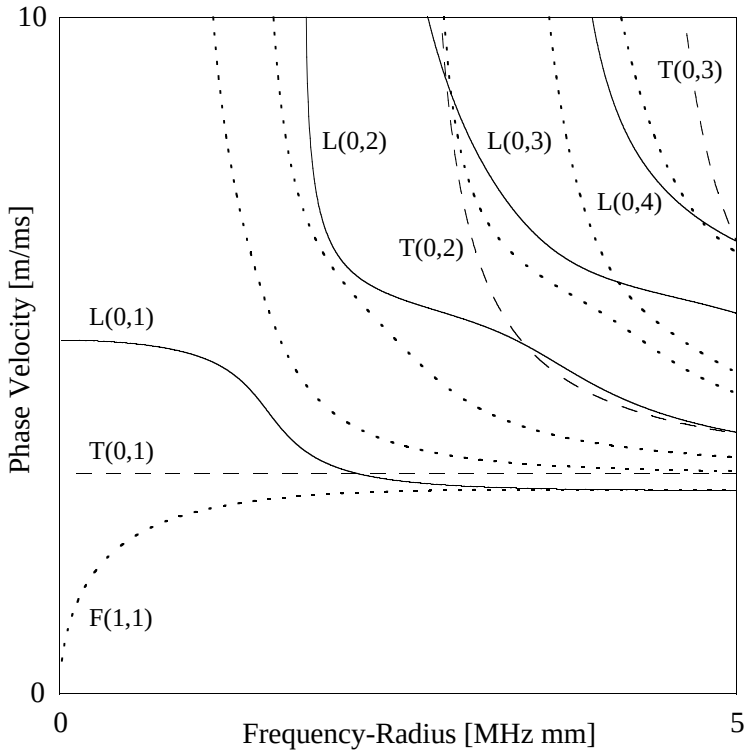

Figure 2.1: Phase velocity dispersion curves for a steel wire in vacuum. Longitudinal modes are plotted in solid lines (—), torsional modes in dashed lines (- -), and flexural modes in dotted lines ($\cdots$). For clarity, higher order flexural modes are not labelled.

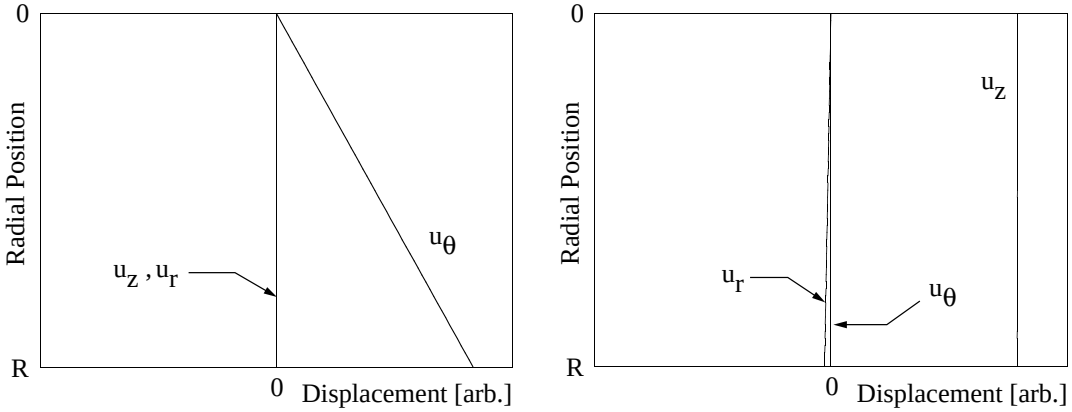

(a) T(0,1) at 0.1 MHz mm **(b)** L(0,1) at 0.1 MHz mm

Figure 2.2: Displacement mode shapes for a steel cylinder in vacuum.

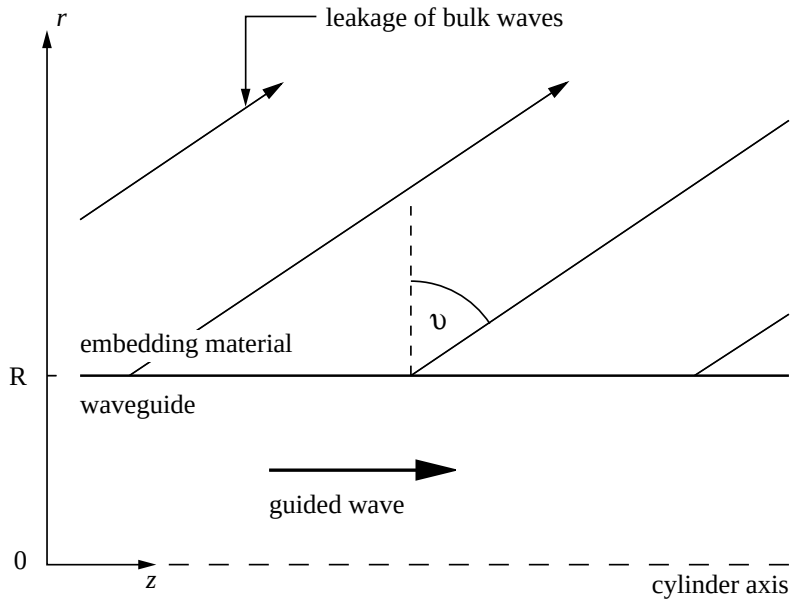

Figure 2.3: Schematic showing the leakage of bulk waves at an angle ϑ, which is given by Snell's law.

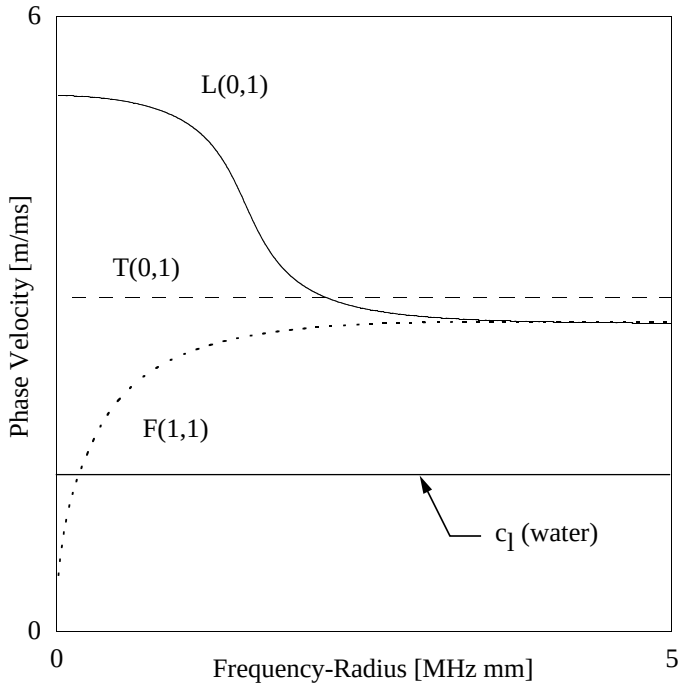

(a)

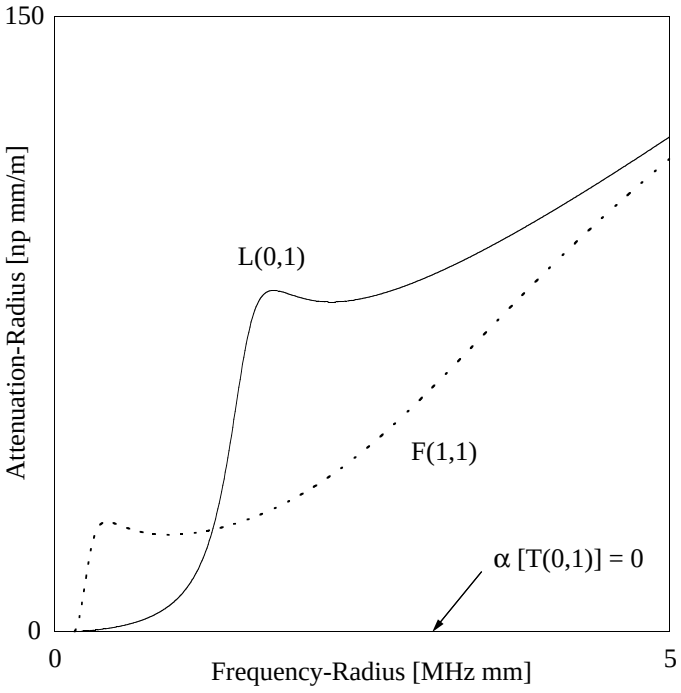

(b)

Figure 2.4: (a) Phase velocity and (b) attenuation dispersion curves for a steel bar embedded in non-viscous water. Note that T(0,1) has zero attenuation, and that F(1,1) becomes non-leaky once its phase velocity drops below the bulk velocity of water.

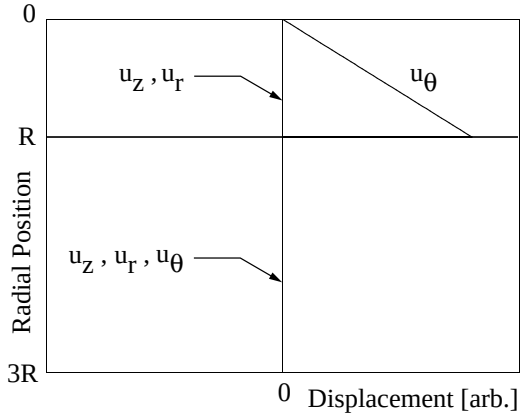

(a) T(0,1) at 0.1 MHz mm

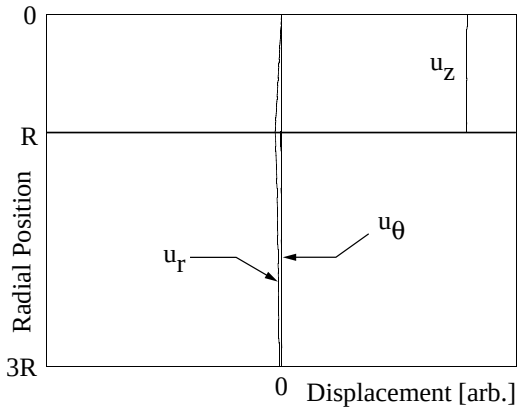

(b) L(0,1) at 0.1 MHz mm

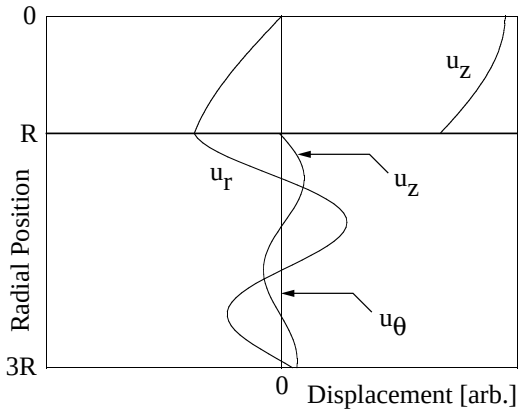

(c) L(0,1) at 1 MHz mm

Figure 2.5: Displacement mode shapes for a steel bar immersed in water.

Chapter 3

Experimental Techniques

3.1 Background

This chapter introduces the general experimental concepts used in this work. The transduction mechanisms based on magnetostriction and piezoelectricity will be presented in Sec. 3.2. Since the effect of magnetostriction is less well-known than that of piezoelectricity, a brief introduction of the physical foundations will be given. This ensures that the peculiarities of the magnetostrictive transduction system can be understood. For further information on the physics behind magnetostriction, the reader will be referred to more detailed literature [29, 30, 31]. On the other hand, the use of piezoelectric materials is well-known, and the physical foundations are well documented in literature [8, 32]. Therefore, mainly the application to the excitation of waveguide modes will be discussed. It should be noted that there exist other electro-magnetic transducer (EMAT) systems which are not based on magnetostriction and which have been used for example for the excitation of guided waves in tubes [33]. However, these systems have a lower sensitivity than magnetostrictive systems, are are therefore not pursued here.

Furthermore, the general experimental set-up, which is common in the waveguide experiments, is presented. The experimental procedures, which are different for the attenuation and the reflection coefficient measurements, will be discussed separately in Sec. 4.4 and Sec. 5.7, respectively.

In order to determine the material properties of a material embedding a waveguide, it is also necessary to know the material properties of the waveguide itself. The techniques applied to measure the waveguide properties are presented in Sec. 3.4. It is assumed that the density of the waveguide material, ρ, is known, and that the waveguide material is elastic and isotropic.

3.2 Excitation of Waveguide Modes

3.2.1 Magnetostrictive Excitation

When a material is exposed to a magnetic field, it may be strained and change its dimensions. This effect is referred to as *magnetostriction* [29]. Conversely, when a magnetostrictive material is strained, a magnetic field is generated. This is called *inverse magnetostriction*. The source of this effect lies mainly in the so-called spin-orbit coupling in atoms, i.e. the coupling between the net magnetic moment of atoms and their electron clouds (see, for a detailed explanation, [29]). As the spins of the atoms of a particular magnetic domain align themselves in the external magnetic field, the non-spherical electron clouds are also rotated. This results in a change of the dimensions of the whole domain.

There are a number of magnetostrictive effects, which are described in detail in Ref. [31]. Two of those are important in the context of this work. The first effect refers to the change in dimension in the direction of the applied magnetic field. For example, a magnetostrictive cylindrical rod changes its length when subjected to an axial magnetic field. This longitudinal effect is called the *Joule effect*. The second effect refers to a twisting motion due to a combination of circular and axial magnetic fields. This is called the *Wiedemann effect*. These effects can be exploited for the excitation of longitudinal and torsional waveguide modes in cylindrical waveguides, and have been researched extensively by Tzannes [34]. Magnetostrictive excitation of waveguide modes has also been used by other authors [35, 36, 37], and a general review is given in [38]. A detailed discussion regarding torsional modes in magnetostrictive cylinders was given by Aime *et al.* [39].

Figure 3.1(a) shows a schematic of a magnetostrictive transduction system. When an alternating current with frequency ω flows through a coil, which acts as a transducer, an axial magnetic field is created inside the coil. As will be explained further below, in order to excite longitudinal modes of the same frequency, the section of the magnetostrictive waveguide, which is inside the coil, has to be permanently axially magnetised (see Fig. 3.1(b)). In order to excite torsional modes, this section has to be permanently magnetised in the circular direction. The interaction of the time varying axial magnetic field produced by the coil and the permanent magnetic field in the wire generates stress waves in the waveguide via the Joule or the Wiedemann effect. Conversely, a stress wave of frequency ω causes an alternating magnetic field via the inverse magnetostrictive effects. This induces an alternating current of frequency ω in the coil, which then acts as a receiver. Also for reception, the material has to be permanently magnetised.

For transmission, the section of the waveguide where the coil is placed has to be magnetised permanently in order to avoid the *double frequency effect* [29]. This is explained by means of Fig. 3.2, which shows schematically the development of the variables magnetisation, M, and strain, ε, during one cycle of an external, alternating magnetic field, $H(t)$. Consider a magnetostrictive material which has been magnetised beforehand in a large magnetic field of magnitude H_0, as depicted in the graphs on the left hand side of Fig. 3.2. With no external field present, there is a remnant magnetisation, M_0. During one cycle of an alternating magnetic field of frequency ω and maximum amplitude H_0, the magnetisation completes a whole hysteresis loop. At the same time, the strain completes two whole loops, and therefore a wave with frequency 2ω is excited in the material. This is called the double frequency effect. However, if the magnetic field applied by the transmitting coil, H_{coil}, which is used to excite the guided waves, is small compared to H_0, the magnetisation will oscillate around the value of M_0 with the same frequency ω. Hence, also the strains will oscillate around the value ε_0 with that same frequency. This is shown on the right hand side of Fig. 3.2. In a completely demagnetised sample, the field H_{coil} would cause the magnetisation to go through a whole hysteresis loop and hence produce stress waves of twice the frequency.

For the reception of guided waves the reason for permanent magnetisation lies not in the double frequency effect, but in the fact that a stress only causes a change in magnetisation in a magnetised sample. This can be seen in Fig. 3.3, which schematically shows the dependence of magnetisation, M, on the applied magnetic field, H, for both zero stress, $T = 0$, and non-zero stress, $T = T_1$. A sample which has been previously magnetised changes magnetisation from point "A" to point "B" when no external field is present. However, at the origin the curves for zero and non-zero stress meet, and a stress applied to a demagnetised section produces no magnetisation. For a more detailed explanation see [29].

As can be seen from the figures in this section, magnetostriction is a non-linear effect, and the direction of the strain does not depend on the sense of the applied magnetic field. In the context of the Joule effect, for example, a rod of magnetostrictive material is said to show negative magnetostriction if, compared to the demagnetised state, it contracts axially when a magnetic field is applied, and positive magnetostriction if it lengthens. The schematic in Fig. 3.2 thus shows a material with positive magnetostriction.

Materials with large magnetostrictive coefficients are for example FeNi- and FeCo-alloys. One particular FeCo-alloy, containing 49% Fe, 49% Co, and a balance of vanadium and manganese, is known under the trade names Permendur and Remendur. It can be obtained, for example, from Panametrics Inc. in the form of circular waveguides of approximately 1.5 mm diameter and 1 m length (KT55 kit, [40]). Transducers were also obtained from Panametrics Inc. and they were used in some of the experiments (see Fig. 3.4(a) for a photograph). These are optimised to work at around 100 kHz.

It is straightforward to self-manufacture such transducers, since the basic components consists only of a coil made of thin copper-wire which is wound around a bobbin. In the experiments presented in the remainder of the thesis, a teflon-tube with an inner diameter of 1.5 mm and a wall thickness of 1 mm was used as a bobbin. The copper wire (0.2 mm diameter) was wound in three to four layers around the

bobbin to form a coil and fixed using instant glue. The length of the coil was about 5 mm (see photograph in Fig. 3.4(b)). By comparison, the wavelength of the fundamental torsional mode in a Permendur bar at 100 kHz is approximately 32 mm. With these transducers, it was possible to excite guided modes up to a frequency of around 400 kHz.

The permanent axial magnetisation of the magnetostrictive wire is in general achieved by placing a bar magnet parallel to the section of the wire which is located inside the coil. Circumferential magnetisation may be achieved by applying a constant DC-current through the wire, since an electrical current in the axial direction produces a circumferential magnetic field. This has the advantage that constant circumferential magnetisation is ensured, but is on the other hand not practical due to the additional electrical connections which have to be made to the magnetostrictive wire. Instead, the wire can be magnetised before the experiment by applying a high DC-current along the wire for a very short time.

3.2.2 Piezoelectric Excitation

Piezoelectric materials are widely used in all fields of ultrasonics as a means of exciting stress waves in materials (see, for example, [41]). When an electric field is applied to a piezoelectric material, it changes dimensions, the stress being linearly related to the electric field [32]. Inversely, an electric field is generated when the material is strained. Piezoelectric discs or plates which are coupled to another material will excite stress waves in that material when an alternating electric field is applied to them. The frequency of the stress waves is equal to that of the alternating electric field.

In order to excite a particular waveguide mode, it is possible to place piezoelectric elements on the surface of the waveguide such that the displacements match the mode shape of the desired mode on this surface. This is being used for example in pipe testing, where an array of transducers is used to excite and receive longitudinal, torsional and flexural modes [26]. For example, in order to excite a torsional mode in a pipe, piezoelectric plates, which are poled such that they exhibit shear strains

for an applied electric field across the thickness, are placed around the circumference of the pipe such that the displacements of each element are in the circumferential direction.

However, such an arrangement using multiple elements is not feasible in thin wires but is, depending on the radius of the wire, limited to a very small number because of the small surface area. Nevertheless, longitudinal modes can be generated in a straightforward way by placing a single piezoelectric disc at the top end of the wire or bar (see Fig. 3.5). An alternating voltage applied to the electrodes of the disc, which is poled such that it operates in the thickness mode, creates axial displacements over the cross-section of the waveguide. This matches closely the mode shape of the lowest order longitudinal mode, L(0,1), and hence this mode is excited. Care has to be taken to ensure that the end of the wire is as square as possible and that the piezoelectric disc is centred on the axis of the wire such that the excitation of flexural modes is avoided. The diameter of the disc can be chosen such that it is the same as that of the wire. However, this becomes difficult once the wire diameter is below about 1 mm. Then, the diameter of the disc generally has to be chosen larger than the wire diameter because of the difficultly in handling during transducer assembly and poor material availability.

A typical arrangement for the excitation of the longitudinal mode, L(0,1), is shown in Fig. 3.5(a). The transduction system consists of the piezoelectric disc and a steel backing, the disc being directly coupled to the wire. In the case that the diameter of the disc can be chosen to be the same as that of the wire, the disc can simply be attached using general purpose, low viscosity adhesive (for example instant glue), with which very thin bond-lines can be achieved. This is important because in this design, the electrical connection to the electrodes of the disc is via capacitive coupling. As can be seen in the schematic in Fig. 3.5(a), the actual connections to the signal generator are made to the wire and to the backing, in general using crocodile clips. It was found that the noise level is generally smaller when the ground electrode is connected to the side of the disc which connects to the wire. This may be due to the fact that otherwise the wire acts as an antenna.

The diameter of the steel backing is always chosen to be the same as that of the piezoelectric disc. The purpose of the backing is to generate a reaction and thus a significant force in the wire. The transducer is operated below its resonance frequency so as to avoid distortion of the input pulse shape. It should be noted that the backing thus limits the upper operating frequency, depending on the dimensions of the disc and the backing. The effect of the backing geometry on the resonance was investigated by Allin [42]. Nevertheless, this arrangement was found to be better suited for higher frequencies (above around 400 kHz) than the magnetostrictive transducer.

In the case where the wire diameter is smaller than that of the disc, the wire is soldered to the disc (see Fig. 3.5(b)). For this, a solder pellet is first placed on a disc and melted using a soldering iron. The end of the wire, which has been prepared using solder flux, is placed carefully into the middle of the molten pellet, and then the solder is allowed to cool. This way the disc is firmly attached to the wire. It should also be noted that in this arrangement the electrical connection is made to the solder pellet instead of the wire because, in thin wires of the order of about 0.5 mm or less, scattering of the ultrasonic guided wave occurs even from very minor disturbances such as touching the surface with a crocodile clip. An alternative way of attaching the wire to the piezoelectric disc has been investigated by Atkins [43]. Atkins used a cone of epoxy resin instead of solder, and studied the effects of the cone geometry on the excitation of the longitudinal mode. However, it was found that the solder gave satisfactory results and was much easier to manufacture.

The torsional mode, T(0,1), may also be excited using piezoelectric transduction. Figure 3.5(c) shows a schematic of the arrangement in this case. Two piezoelectric shear elements are placed on opposite sides of the wire, and they are excited with the same input signal. The displacements and the polarisation of the shear transducers are such that a torsional momentum is created. However, it was found that, in thin wires it was difficult to maintain axi-symmetry and hence flexural modes were likely to be excited as well. Therefore the magnetostrictive system was favoured for torsional waves.

3.3 Experimental Setup

3.3.1 Waveguide system

The general set-up for the experiments conducted in this work is shown in Fig. 3.6. When magnetostrictive excitation is used, a magnetostrictive wire, acting both as a transduction wire and a delay line, is connected to a measurement wire, which can be chosen to have a different diameter than the magnetostrictive wire. In general, the measurement wires used in the experiments were made of stainless steel, but other suitable wire materials may be used. With piezoelectric excitation, the magnetostrictive wire is replaced by a steel wire.

The guided wave, which is generated in the transduction wire, propagates along the wire until it is partly reflected from the interface with the measurement wire. This reflection serves as a reference in successive experiments to cancel out effects such as changes in the excitation amplitude. The part of the guided wave which is transmitted into the measurement wire interacts with the embedding material. The reflection method experiments record the reflection which occurs at the point where the wire enters the surrounding material, whereas the attenuation method measurements monitor the reflection from the remote free end of the measurement wire.

As an example, Fig. 3.7 shows the pulse-echo time trace of the torsional mode, T(0,1), in a steel wire connected to a magnetostrictive wire in air. The excitation signal can be seen at the start of the time trace. The first reflection corresponds to the reference reflection from the joint between the magnetostrictive and the steel wire, whereas the second signal is the reflection from the free end of the steel wire. The following signal is the second reverberation between the joint and the free end of the steel wire.

Ideally, the geometry of the interface between the transduction and the measurement wire is perfectly axi-symmetric. Then, below the cut-off frequencies of higher order modes, the lowest order fundamental modes L(0,1) and T(0,1) do not scatter,

by symmetry, into propagating modes other than themselves. The scattering of torsional waves from a diameter step in a cylindrical waveguide was studied in detail by Engan [44]. The theoretical results presented in his paper can be used to estimate the reflection and transmission of the incoming torsional wave for different diameters of the transduction and the measurement wire. However, it should be noted that here the two adjoining wires may have different material properties and that the connection is not perfect, and thus such a prediction can only give an indication.

The connection between the transduction wire and the measurement wire is best accomplished by drilling a hole approximately 1–2 mm deep into the larger diameter wire at one of its ends, with a diameter matching that of the smaller diameter wire. The smaller diameter wire is then glued into the hole using instant glue. This makes a bond which is at the same time firm enough for the measurements, but can also be detached afterwards by a combination of heat and mechanical treatment. This is especially important when using the magnetostrictive wire, which is relatively expensive, because in experiments such as cure monitoring of epoxy resins, the measurement wire has to be disposed of after the experiment. It is also possible to use solder instead of glue, however, it was found not to be as practical as gluing.

In early experiments, the piezoelectric transducers were directly attached to measurement wires of 0.5 mm diameter or less to excite longitudinal modes. In this case, the reference reflection was obtained by simply introducing a sharp kink in the wire at a suitable location. This is due to the fact that any change in the curvature of the wire presents a discontinuity in the waveguide geometry (see, for example, [45]). Surprisingly, with a longitudinal mode being incident, it was found in the experiments that the scattering into flexural modes is small. The advantage of this method was that the magnitude of the reflection from the kink and hence of the transmitted signal could be controlled by adjusting the kink angle. The more acute the angle, the higher is the reflection.

In the previous paragraph, the effect of a change in curvature was mentioned. Thin wires are usually delivered on reels and tend to curl when taken off the reel. The

wire generally shows a constant curvature along its length. In vacuum, as long as the radius of the curvature is large compared to the wavelength of the guided wave, this effect can be neglected and the wire can be modelled as a straight wire. However, when the waveguide is embedded in another material, this curvature may have an effect on the attenuation of the guided wave. Beard has found that this effect is significant for high frequency modes, but not as significant for low frequency modes such as the ones used in this work [46]. Therefore, the effect of curvature is neglected here.

3.3.2 Instrumentation

The experiments presented in this thesis make use of a range of instruments. The core of the experimental set-up consists of the *Wavemaker*-instrument, which is purpose built by Macro Design Ltd. [47], and a digital oscilloscope. Alternatively, a *DUI* (Desktop Ultrasonic Instrument) from NDT Solutions Ltd. [48] may be used. Both the *Wavemaker* and the *DUI* can be used to drive piezoelectric and magnetostrictive transducers. Additionally, a computer is used for data capture.

The *Wavemaker* is capable of driving the ultrasonic transducers with a range of different pulse shapes, and can be operated in pulse-echo or pitch-catch mode. The frequency of the input signal to the transducers can be changed almost continuously in the range between 0.05 – 4 MHz, and the received signal can be amplified by up to 60 dB. A LeCroy-oscilloscope is connected to the *Wavemaker* and is used to display and, if necessary, average the received signals. A computer is in turn connected to the oscilloscope via a GPIB-interface, and the software *Spectrum*, a tool which was developed in the NDT laboratory at Imperial College, reads the received waveforms from the oscilloscope and stores them to disk for further processing. This set-up is preferred in the development stages of a technique because of the versatility of its individual components.

In place of this, the *DUI* combines a *Wavemaker* and an oscilloscope, though with limited options, and it can be directly controlled via a computer. The internal arbitrary function generator and a number of pre-set waveforms allows any desired

waveform to be sent, and it can be used both in pulse-echo and in pitch-catch modes. It is better suited for automated operations such as cure monitoring experiments, where numerous waveforms have to be stored in a certain time-interval.

3.4 Measurement of Waveguide Properties

3.4.1 Shear Velocity and Shear Modulus

The shear bulk velocity, c_s, of the waveguide material in a rod can be determined easily by measuring the velocity of the fundamental torsional mode, T(0,1). As mentioned before, T(0,1) propagates at exactly the shear bulk velocity of the waveguide material. The phase velocity, which is the speed at which the wave crests propagate, and the group velocity, which is the speed at which a wave packet propagates along a waveguide in vacuum, are identical due to the non-dispersive nature of the torsional mode. Therefore, the measurement of the velocity of a pulse is identical to a phase velocity measurement. In an experiment, successive reflections from the end of the wire in a pulse-echo arrangement are monitored. From the time for a round trip of a signal, T, and the length of the waveguide, l, the velocity is calculated according to

$$c = \frac{2l}{T}. \tag{3.1}$$

Of course, the longer the distance l, the more accurate the measurement becomes. The shear velocity calculated this way is, in elastic materials of density ρ, related to the shear modulus, μ, by

$$c_s = \sqrt{\frac{\mu}{\rho}}. \tag{3.2}$$

3.4.2 Young's Modulus

As mentioned before, the fundamental longitudinal mode, L(0,1), in a cylinder in vacuum approaches the bar velocity, c_E, in the zero frequency-radius limit. This velocity is related to Young's modulus in the following way:

$$c_E = \sqrt{\frac{E}{\rho}}. \tag{3.3}$$

However, care has to be taken in this case since the longitudinal mode is dispersive. Group and phase velocity of the guided wave are only equal in the zero frequency-radius limit. As an example, the group velocity, which is in free waveguides defined by

$$c_{gr} = \frac{\partial \omega}{\partial \xi}, \tag{3.4}$$

where ξ is the real part of the axial wavenumber of the guided mode (see Sec. 2.3), is plotted together with the phase velocity in Fig. 3.8 for a steel bar in vacuum. It can be seen that the phase velocity is almost constant and equal to the bar velocity over an extended frequency range, but that the group velocity deviates more from this value at higher frequencies than the phase velocity. However, in the practical application, it is easier and more straightforward to measure the group velocity using a narrow-band tone-burst (20 cycles or more). It has thus to be ensured that the measurement frequency is chosen small enough such that the error, $\Delta c = c_E - c_{gr}$, is kept as small as possible.

3.4.3 Young's Modulus and Poisson's Ratio

A numerically more demanding way to determine Young's modulus, E, and at the same time the Poisson ratio, ν, of the waveguide material is to measure the phase velocity of L(0,1) over a range of frequencies. For this, a low frequency, broad-band signal is used to excite L(0,1), which then propagates along a wire of a given length and is reflected from the free end of the wire. The experiment is repeated with the same wire or wire type for a different length. For example, the wire under investigation can be cut down to a smaller length. Software developed by Long *et al.* [49] can then be used to extract the phase velocity from the two signals which have travelled over different lengths.

Nagy and Kent have presented an approximate formula for the dependence of the phase velocity of L(0,1) on the Poisson ratio at low frequency-radius products [50], and also used this formula to determine Poisson's ratio from experimental results. However, the experiments presented in Ref. [50] were based on the measurement of group velocity rather than phase velocity. Expressed in the notation used in this

thesis the relationship given by Nagy and Kent is:

$$c_{ph} = c_E \left[1 - \frac{1}{4}\nu^2(\xi R)^2 + O(\xi R)^4\right], \tag{3.5}$$

where R is the radius of the waveguide. Note that, because dispersion is small at low frequency-radius products, the term ξR is also small.

In the above equation, the axial wavenumber of the guided wave, ξ, implicitly contains the phase velocity, since $\omega = c_{ph}\xi$. Using this equation to eliminate the wavenumber in Eq. (3.5), and neglecting terms of order higher than two yields:

$$c_{ph} = c_E \left[1 - \frac{1}{4}\nu^2 \left(\frac{\omega R}{c_{ph}}\right)^2\right]. \tag{3.6}$$

This is an equation of the form

$$Y = c_E\,[1 - \nu^2 X], \tag{3.7}$$

with

$$Y = c_{ph} \qquad \text{and} \qquad X = \left(\frac{\omega R}{2c_{ph}}\right)^2. \tag{3.8}$$

The variables X and Y are known from the experiment, and a simple linear curve fit can be used to determine c_E and ν. Figure 3.9 shows the range of validity of this approximation for the example of a steel bar in vacuum by comparison to the phase velocity predicted by the software *Disperse*.

As an example, Fig. 3.10 shows an experimentally obtained and processed phase velocity dispersion curve of L(0,1) in a 2.5 mm radius steel bar and the corresponding curve fit. In this case, the bar velocity was evaluated as $c_E = 4.822\,\mathrm{m/ms}$ and Poisson's ratio as $\nu = 0.333$. The curve fit only shows a small standard deviation of $\Delta Y = 0.6\,10^{-3}\,\mathrm{m/ms}$. It should be noted that these values may deviate considerably from the bulk value due to anisotropy of the waveguide material caused by the process of manufacture (see, for example, [51]). Even though the error in this example is small, the accuracy of this method is limited since the dispersion is inevitably small at low frequency-radius products. Therefore, whenever it is possible to use the fundamental longitudinal and torsional modes, the methods presented in Sec. 3.4.1 and Sec. 3.4.2 are preferred.

Poisson's ratio may also be derived from the bar velocity and the shear bulk velocity in the following way [32]:

$$\nu = \frac{1}{2}\left(\frac{c_E}{c_s}\right) - 1. \tag{3.9}$$

3.4.4 Derivation of Longitudinal Bulk Velocity

The longitudinal bulk velocity of the waveguide material, c_l, is derived from those quantities which are experimentally determined as described in the above sections. Young's modulus, E, and the Poisson ratio, ν, are related to the longitudinal bulk velocity by [32]

$$c_l = \sqrt{\frac{E}{\rho}\frac{1-\nu}{(1+\nu)(1-2\nu)}} = c_E\sqrt{\frac{1-\nu}{(1+\nu)(1-2\nu)}}. \tag{3.10}$$

Alternatively, the bulk shear velocity, c_s, and Poisson's ratio can be combined to yield the longitudinal bulk velocity [32]:

$$c_l = c_s\sqrt{\frac{1-\nu}{\frac{1}{2}-\nu}}. \tag{3.11}$$

3.5 Summary

The experimental concepts which are used in this work have been discussed. Magnetostrictive transduction is applied to excite both the fundamental torsional and the longitudinal mode up to a frequency of approximately 400 kHz. Piezoelectric transducers directly attached to the wire are used to excite the fundamental longitudinal mode. These can be applied at higher frequencies than the magnetostrictive transducers.

The experimental setup generally consists of a transducer, a transduction wire, which also acts as a delay line, and a measurement wire. From the point where the two wires are connected, a reference reflection of the incident guided mode is obtained. The measurement wire is embedded in the material under investigation, and reflections arriving later in time than the reference reflection have interacted with the surrounding material.

The waveguide properties are determined either by the direct measurement of the shear velocity and the bar velocity in cylindrical waveguides or by a more sophisticated method, which is based on the measurement of the phase velocity dispersion of the fundamental longitudinal mode. This method yields Young's modulus and Poisson's ratio of the waveguide material. All other material properties of the elastic wire can be derived from these quantities.

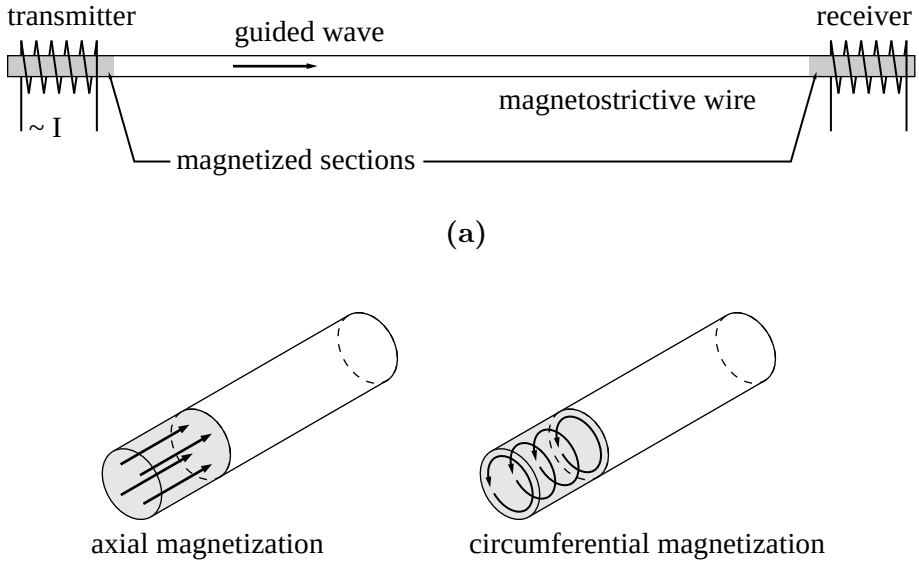

Figure 3.1: (a) Schematic of a magnetostrictive transduction system. The shaded areas indicate permanently magnetised sections. (b) Illustration of axial and circumferential magnetisation in these sections. The arrows indicate the direction of the magnetisation, **M**.

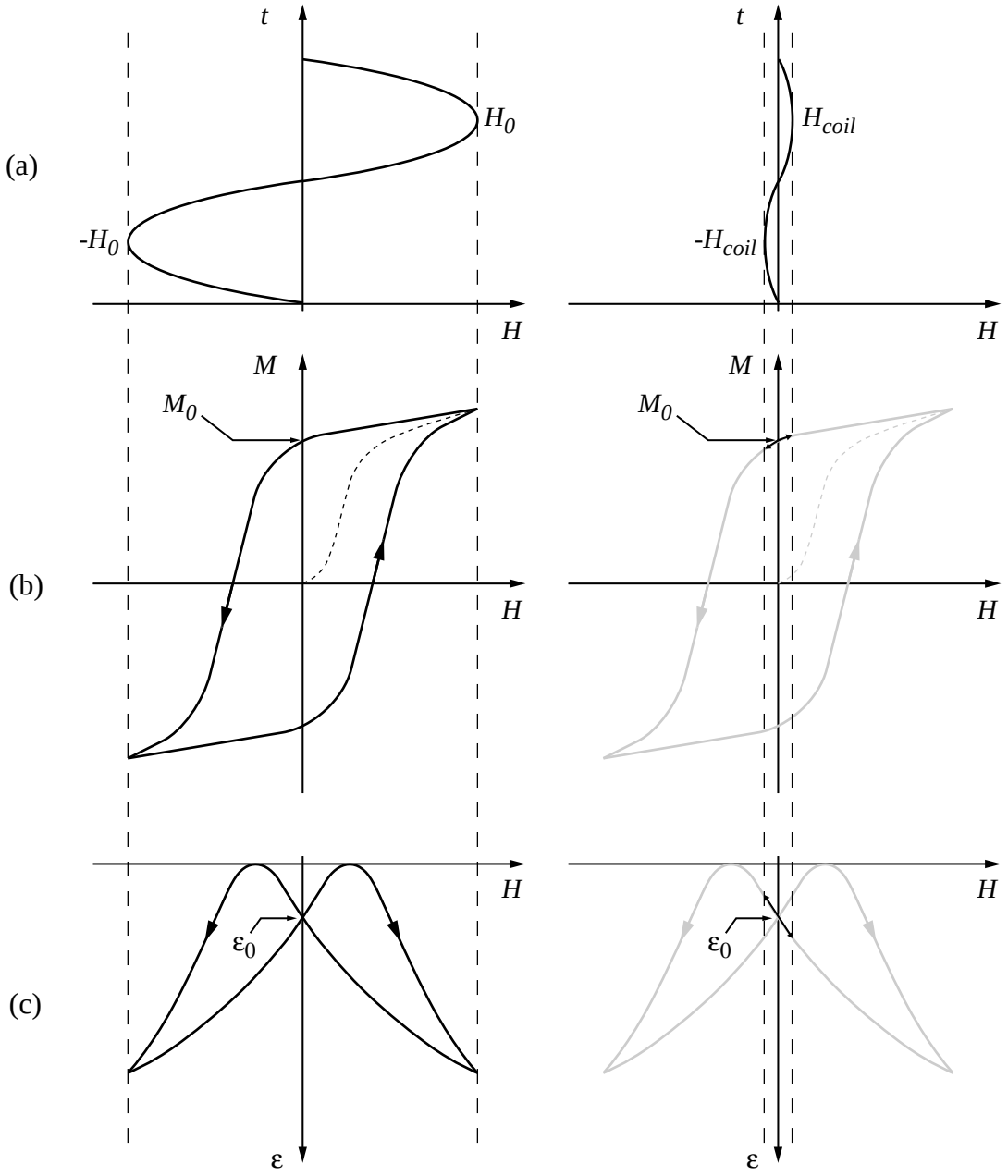

Figure 3.2: Schematic of the development of magnetisation and strain in a magnetostrictive material. (a) Time-varying, external magnetic field $H(t)$, (b) magnetisation $M(H)$, and (c) strain $\varepsilon(H)$. In the graph on the left hand side, the material is magnetised in a large magnetic field, H_0, whereas in the graph on the right hand side, this material is subsequently subjected to a much smaller field, H_{coil}. See text for the explanation of the double frequency effect.

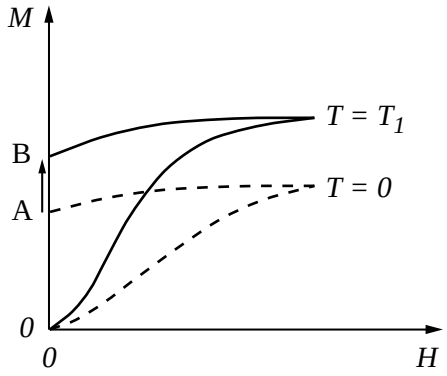

Figure 3.3: Schematic of the influence of stress, T, on the magnetisation, M. The curves show the hysteresis loop as the material is being magnetised by an external field, H, for the first time. Stress has no influence on a completely demagnetised sample.

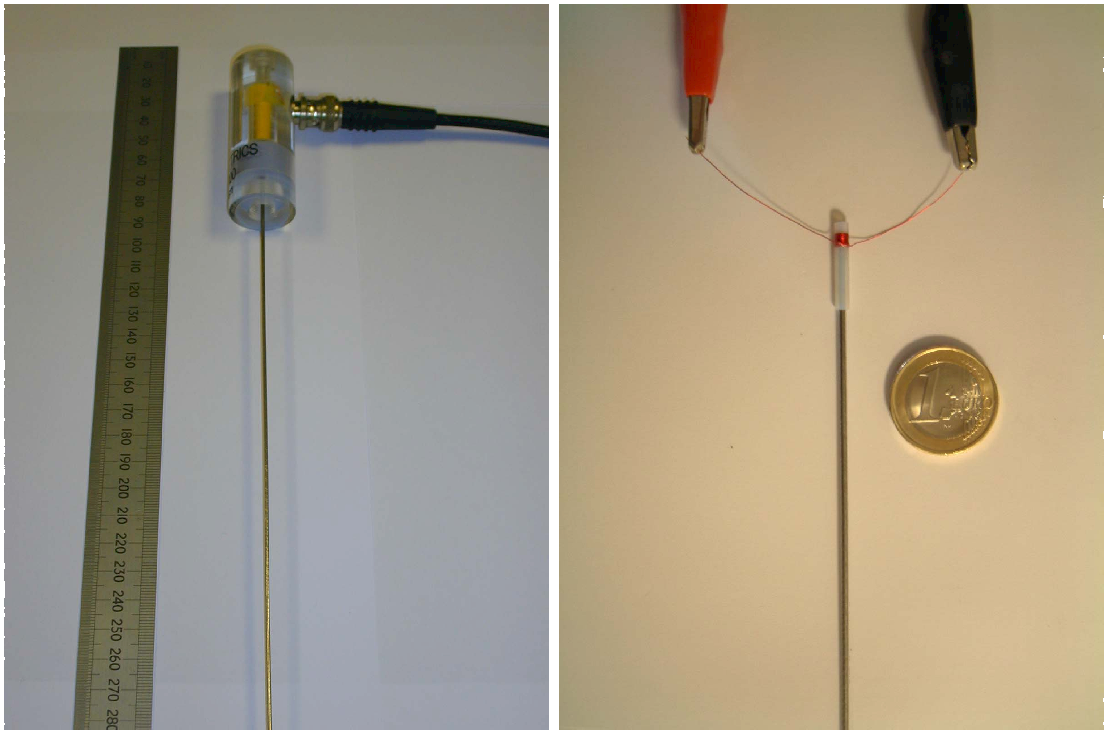

(a) **(b)**

Figure 3.4: (a) Photograph of the magnetostrictive transducers obtained from Panametrics Inc., and (b) photograph of a self-manufactured transducer.

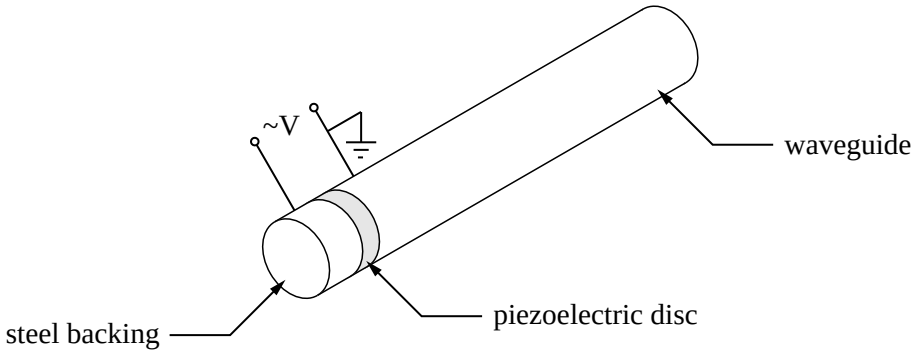

(a)

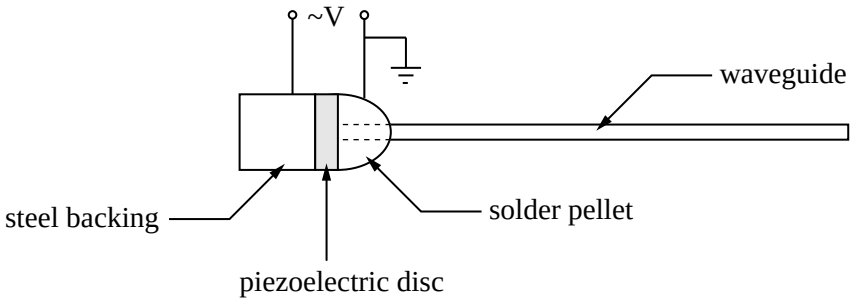

(b)

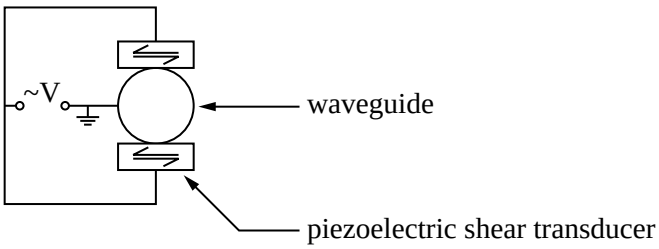

(c)

Figure 3.5: (a) Schematic of the piezoelectric transduction mechanism to excite the L(0,1)-mode. (b) Schematic of the mechanism when the wire waveguide diameter is much smaller than that of the piezoelectric disc. (c) Arrangement of piezoelectric shear transducers to excite T(0,1).

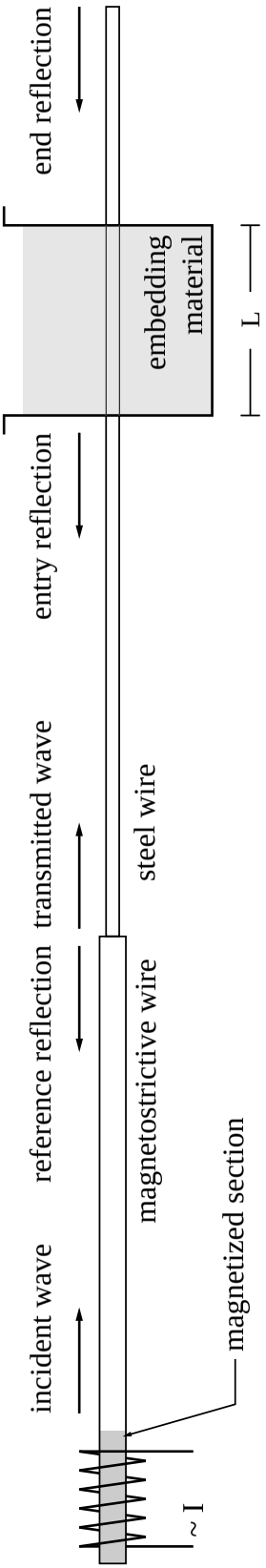

Figure 3.6: Schematic of the experimental set-up, here shown using magnetostrictive transduction.

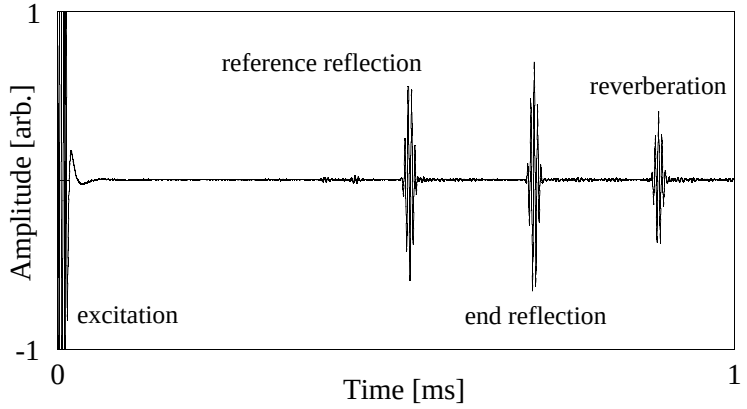

Figure 3.7: Typical time trace of T(0,1) in pulse-echo arrangement, excited using magnetostrictive excitation.

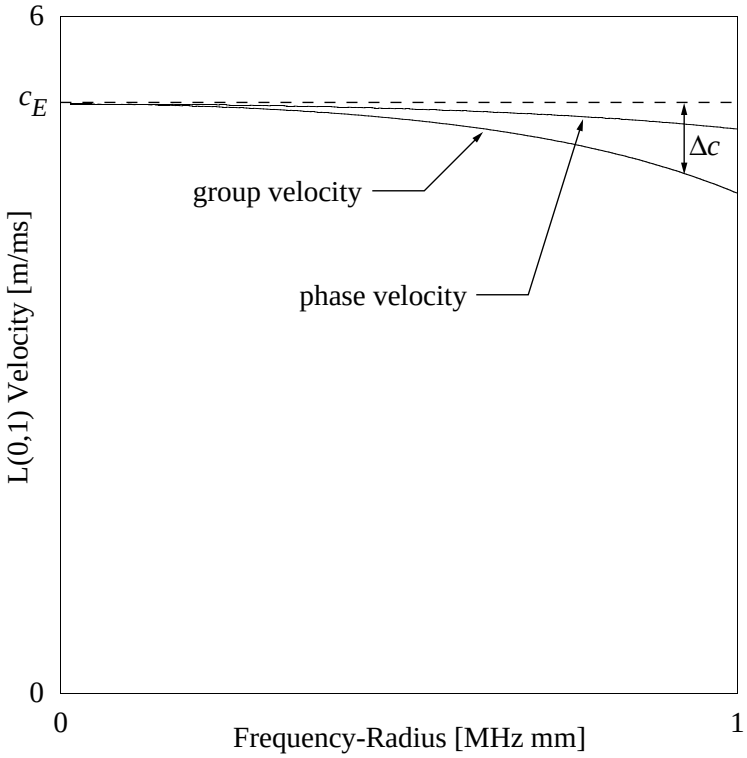

Figure 3.8: Comparison between the phase and group velocity of L(0,1) at low frequency-radius products for a steel bar in vacuum. The material properties of steel are given in Tab. 2.1. The difference between the bar velocity and the group velocity is indicated by Δc.

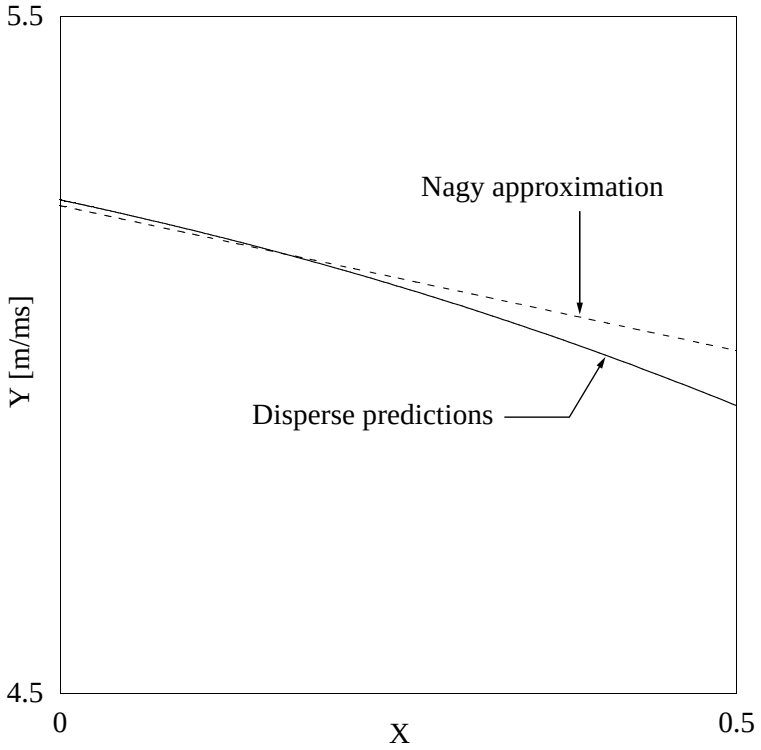

Figure 3.9: Comparison between Disperse predictions and the approximate formula of Eq. (3.7) for a steel bar in vacuum. The quantities X and Y are defined in Eq. (3.8). A value of $X = 0.4$ corresponds in this case to a frequency-radius product of approximately 1 MHz mm.

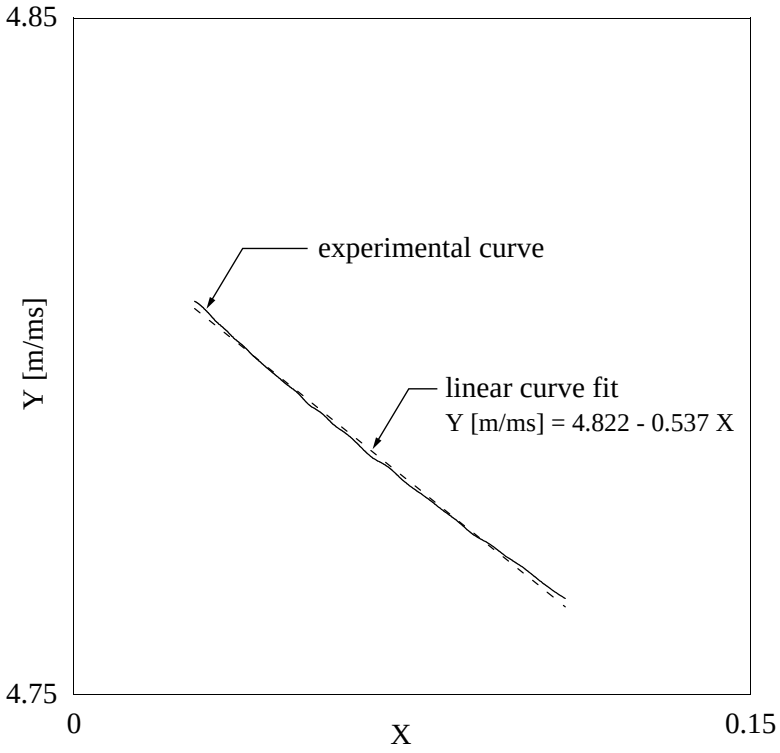

Figure 3.10: Example of experimental results for the phase velocity (solid line) and the corresponding linear curve fit (dashed line). The quantities X and Y are defined in Eq. (3.8).

Chapter 4

Attenuation Method

4.1 Background

This chapter introduces the attenuation method as a technique to measure the material properties of an embedding material. Here, we concentrate mainly on the measurement of the properties of viscous liquids. This serves the purpose of validating the theoretical background of the attenuation technique experimentally with the use of viscous liquids whose properties are well documented. Apart from being an application in its own right, for example in the context of industrial process monitoring of liquids, this is also necessary for the justification of its use for the cure monitoring application, being the main motivation for this work.

The quantitative previous research into the use of waveguide techniques to measure material properties of an embedding material has also concentrated on viscous liquids. Attention has also been given to other media such as slurries or, as will be discussed in Ch. 6, to epoxy resins during cure, however, these results are of a qualitative nature. The waveguide techniques can be divided into two main classes: The first class of experiments measures the change in the wave speed of a guided mode when the waveguide is embedded in another material compared to the case when it is in vacuum. The second class of experiments is based on the attenuation method presented in this thesis.

The corresponding literature will be reviewed in Sec. 4.2. The specific literature

regarding waveguide techniques for cure monitoring will be discussed in Sec. 6.1. Section 4.3 describes the solid-like model for viscous liquids, which is used by the software DISPERSE to predict the dispersion curves. Then it will be explained in detail how to extract the shear viscosity and the longitudinal velocity from guided wave attenuation measurements.

4.2 Review of Literature

The use of ultrasonic guided waves for the measurement of material properties such as the density and the viscosity of an embedding fluid has been investigated previously by several authors. Many of the techniques used to determine the density are based on the measurement of the torsional wave speed in waveguides of non-circular cross-section. Kim and Bau [52] and subsequently Smit and Smith [53] were able to determine the density of an embedding fluid, considering that the speed of torsional waves decreases with increasing density of the fluid. It can be shown that in most cases of interest the torsional wave speed, c, can be approximated by

$$\frac{c}{c_0} = 1 - A_1 \frac{\rho_f}{\rho_s}, \tag{4.1}$$

where ρ_f and ρ_s are the density of the embedding fluid and the waveguide, respectively, and c_0 is the wave speed without fluid loading. A_1 is a shape factor, determined by the cross-section geometry of the waveguide [36]. For circular cross-sections, $A_1 = 0$. This has also been applied to the measurement of two-phase fluids by Kim *et al.* [36] and to slurries by Costley *et al.* [54].

Kim and Bau have taken this approach further to simultaneously measure the density and the shear viscosity of an embedding fluid [55]. In this case, the torsional sensor consists of a rod with two sections of different cross-sections, a rectangular and a circular one. The difference in torsional wave speed for the free and the fluid-loaded rectangular waveguide is sensitive to the density of the fluid, whereas the change in wave speed in the circular waveguide depends on the product of dynamic viscosity and density. The two measurements are combined to give both density and dynamic viscosity.

However, not only can the change in the guided wave speed be very small, also a short gauge length, such as the embedded length in adhesive joints for a cure monitoring application, would further decrease the sensitivity of this technique.

As will be seen in the following sections, experiments based on the measurement of guided wave attenuation rather than wave speed are a promising alternative. Roth and Rich built a device as early as 1953, measuring the viscosity of liquids using a strip-like waveguide sensor [56]. In their paper, the attenuation of the lowest order symmetric guided wave is related to the viscosity of the embedding liquid. Recently, Costley *et. al.* have presented a method based on the attenuation of the fundamental torsional mode [57]. However, their method is non-analytical and requires the use of calibration liquids. Also Kim *et. al.* studied the effect of viscous fluid loading on torsional wave attenuation in circular rods, and derived an asymptotic formula which was experimentally verified [58].

In contrast to the first class of experiments, which measure a change in guided wave speed, the second class of experiments, measuring the guided wave attenuation, has received much less attention regarding the quantitative prediction of material properties, and the current literature is of a qualitative nature. This task is addressed in the remainder of this chapter.

4.3 Solid Model for Viscous Liquids

The case where the embedding medium is a liquid with Newtonian viscosity will be discussed in this chapter. In all the following considerations, the density of the fluid is assumed to be known.

A viscous fluid can be represented by a solid-like material with a phase velocity and attenuation for both longitudinal and shear bulk waves [59, 60]. It can be shown that the dynamic shear velocity in the liquid, c_s, can be expressed in terms of the

shear viscosity, η, in the following way:

$$c_s = \sqrt{\frac{2\eta\omega}{\rho_f}}, \tag{4.2}$$

where $\omega = 2\pi f$ is the circular frequency, and ρ_f is the density of the fluid. The shear attenuation, α_s, in nepers/m, is calculated as

$$\alpha_s\,[\mathrm{np/m}] = \sqrt{\frac{\omega\rho_f}{2\eta}}. \tag{4.3}$$

It can be seen from this that the shear bulk velocity and attenuation in a viscous fluid are related to each other by

$$c_s\alpha_s = \omega, \tag{4.4}$$

and thus only one variable has to be determined in order to fully characterise its shear properties. Consider now the attenuation given in nepers per wavelength, α_s':

$$\alpha_s'\,[\mathrm{np/wl}] = \lambda\,\alpha_s\,[\mathrm{np/m}], \tag{4.5}$$

where λ is the wavelength. The wavelength is related to the phase velocity by

$$\lambda = \frac{c_s}{f}, \tag{4.6}$$

and combining this relationship and Eq. (4.4) with Eq. (4.5) yields

$$\alpha_s'\,[\mathrm{np/wl}] = 2\pi. \tag{4.7}$$

In the following, the numerical implementation uses this to fix the attenuation in nepers per wavelength and hence only the shear velocity is searched for. Subsequently, the shear viscosity is calculated from the shear velocity using Eq. (4.2).

The longitudinal properties are characterised by bulk velocity, c_l, and attenuation, α_l. In the Stokes model [60], which is adopted here, the longitudinal attenuation is assumed to arise entirely from the shear viscosity. The relationship between the bulk velocity and attenuation of longitudinal waves is more complicated than for shear waves. However, it can be shown that the change in longitudinal bulk velocity when the viscous losses are accounted for, compared to the viscosity-free case, is very small. For example, for Glycerol with an assumed shear viscosity of 10 Pa s,

the longitudinal velocities calculated including and excluding the viscous effect differ by about 0.05%. Therefore the effect on the longitudinal velocity will be neglected here. In the case that $c_s^2 \ll c_l^2$, i.e. for relatively low viscosity values, the bulk attenuation may approximately be written as

$$\alpha_l \approx \frac{2\omega^2\eta}{3c_l^3\rho_f} \tag{4.8}$$

(see also [60]). The liquids examined in this thesis are well described by these approximations, and the above equations are implemented in the software DISPERSE. However, it should be noted that for high viscosities a more rigorous approach may have to be adopted.

4.4 Experimental Setup for Attenuation Measurements

Attenuation is measured by comparing the amplitude of the guided wave when the waveguide is in air to the amplitude when the waveguide is embedded over a given length, L (see Fig. 3.6). As mentioned before, the guided wave which is excited in the transduction wire is partly reflected from the joint with the measurement wire, and this reflection serves as a reference. The fraction of the guided wave which is transmitted across the joint into the measurement wire is subsequently reflected from the free end of the measurement wire. In the section where the wire is embedded in the viscous liquid, the guided wave is attenuated. Figure 4.1 shows typical experimental time traces of T(0,1) before and after embedding a steel wire in Glycerol.

At a given frequency, the amplitudes of the Fourier transforms of the reference reflection and the end reflection before embedding are denoted by A_0^{vac} and A^{vac}, respectively, and after embedding by A_0^{emb} and A^{emb}, respectively. The guided wave attenuation α in np/m over the embedded length L is then calculated from

$$\alpha = -\frac{1}{2L}\ln\left(\frac{A^{\text{emb}}/A_0^{\text{emb}}}{A^{\text{vac}}/A_0^{\text{vac}}}\right). \tag{4.9}$$

Note that if the end of the wire is also embedded in the liquid, the guided wave is not totally reflected but may also transmit energy into the liquid through the

end face. This additional loss would introduce a small error in the attenuation calculations, and is therefore avoided by leaving the end of the wire free. Also note that reflections from changes in the surface impedance (such as the entry reflection) are neglected here. For viscous liquids, this assumption is valid to a high degree of accuracy (see Ch. 5 for the dependence of the entry reflection on the shear velocity of an embedding material).

The measurement wires typically employed in the experiments were stainless steel wires with radii between 0.25 mm and 2.5 mm. The material properties for the wires used in the following experiments were determined experimentally by measuring the bar velocity and the torsional velocity (according to Sec. 3.4.1 and Sec. 3.4.2), and are listed in Tab. 4.1. Polyethylene beakers were used as a container for the liquids, and the measurement wire was fed through holes in the walls.

Table 4.1: Material parameters used for the analysis in Ch. 4.

Material	c_l [m/s]	c_s [m/s]	ρ [kg/m^3]
Steel wire (0.25 mm radius)	5560	3060	7930
Steel wire (0.50 mm radius)	5120	2950	7930
Steel wire (1.00 mm radius)	5550	2940	8070
Steel wire (2.50 mm radius)	5630	2980	7770
Glycerol	1920	see Eq. (4.2)	1258

4.5 Measurement of Shear Viscosity Using T(0,1)

4.5.1 Numerical Predictions

As mentioned in Sec. 2.4.3, the fundamental torsional mode has surface displacements in the angular direction only, and therefore only leaks shear bulk waves into a surrounding medium. For this reason, the attenuation of T(0,1) is entirely due to shear leakage, and hence is sensitive to the acoustic shear properties of the sur-

rounding material only. The software DISPERSE can be used to predict the T(0,1)-attenuation dispersion curves as a function of the shear viscosity, assuming that the density of the viscous liquid and the material properties of the waveguide material are known. In an experiment, the attenuation is measured and the dispersion curves are used to correlate this to the shear viscosity.

It should be noted that the dispersion curves only depend on the frequency-radius product as described in Sec. 2.3.2 when the material properties do not depend on the frequency themselves. Here, the shear velocity of the viscous liquid depends on the frequency, and hence the frequency-radius dependence of the dispersion curves is no longer valid.

In order to illustrate the back-fitting procedure, Fig. 4.2(a) shows as an example a T(0,1)-attenuation measurement for a 1 mm radius steel bar embedded in an aqueous solution of Glycerol at several frequencies, and Fig. 4.2(b) shows the predicted T(0,1)-attenuation dispersion curves at exactly these frequencies. An attenuation value in plot 4.2(a), for example at 0.175 MHz, corresponds to a point on the appropriate dispersion curve in plot 4.2(b). In this way, the dynamic viscosity can be directly determined. In principle it is sufficient to evaluate the viscosity at one single frequency. However, in order to increase the accuracy by averaging, and to verify the frequency dependence of the dispersion curve, measurements are taken at several frequencies.

4.5.2 Experimental Validation

Viscosity standards used to calibrate viscometers can be used to estimate the accuracy of the guided wave measurements. As an example, the commercial viscosity standard Cannon VP450, which is a mineral oil, was obtained for the experiments [61]. Figure 4.3 shows an attenuation measurement of T(0,1) at a temperature of 21.0 °C using a 0.5 mm radius steel wire. The material properties of the steel wire are given in Tab. 4.1. At each frequency, the viscosity was calculated, and the dispersion curve, which is also plotted in Fig. 4.3, was predicted using the average value of viscosity. The average viscosity was this way determined as $\eta = 1.42 \pm 0.03\,\mathrm{Pa\,s}$,

where the error is the standard deviation from the mean value.

Most viscous liquids follow an approximate relationship of the form

$$\log \eta = a + \frac{b}{T}, \tag{4.10}$$

where a and b are characteristic constants and T is the absolute temperature (see for example [62], p. 52). The viscosity of the standard at the measurement temperature was interpolated according to the above expression using the data at different temperatures stated by the manufacturer in the range between 20 °C and 26 °C, and was determined as $\eta = 1.395\,\mathrm{Pa\,s}$ at the measurement temperature. Thus, the viscosity can be determined within a range of approximately 2%.

As another example, the attenuation measurement for a 1 mm steel wire immersed in an aqueous solution of Glycerol with 0.7% water content at 20 °C, shown in the explanatory plot in Fig. 4.2, yields a dynamic viscosity of $\eta = 1.17 \pm 0.07\,\mathrm{Pa \cdot s}$. This compares very well to a literature value, which is available for an aqueous Glycerol solution with 1% water content, of $\eta = 1.15\,\mathrm{Pa \cdot s}$.

4.6 Measurement of Shear Viscosity Using L(0,1)

4.6.1 Low Frequency-Radius Approximation

The longitudinal mode L(0,1) may, at low frequencies, also be used to measure the dynamic viscosity of an embedding viscous liquid. As mentioned before, the attenuation of L(0,1) is in this frequency range almost entirely caused by shear leakage and can therefore be directly related to the shear velocity and hence the shear viscosity. As an example, Fig. 4.4 shows the predicted L(0,1)-attenuation for a 0.25 mm radius steel wire immersed in Glycerol with a dynamic viscosity of 1 Pa s together with a hypothetical non-viscous Glycerol. The material properties of Glycerol for this and the following analysis are given in Tab. 4.1, unless otherwise stated. It can be seen that the longitudinal leakage at low frequencies is very small for the non-viscous fluid. The difference in attenuation of the non-viscous and

viscous case is entirely due to viscosity-induced attenuation, which is predominant at low frequencies.

Nagy and Kent give an approximate formula for the viscosity-induced attenuation, α_η, of L(0,1) at low frequencies, which is useful for a first estimate [50]:

$$\alpha_\eta = \frac{1}{R}\sqrt{\frac{\omega\eta\rho_f}{2E\rho_s}}, \tag{4.11}$$

where R is the radius, E is Young's modulus, and ρ_s is the density of the waveguide. This formula was derived assuming firstly that there are no radial displacements, thus neglecting the longitudinal leakage, and secondly that the wire diameter is large compared to the viscous skin depth. Figure 4.5 shows the attenuation of L(0,1) for a steel bar embedded in Glycerol as predicted by Eq. (4.11) together with the curve predicted by DISPERSE and which is the same as given in Fig. 4.4 for viscous Glycerol. The viscosity-induced attenuation may also be obtained by simply subtracting the attenuation curve for the bar in the viscous fluid from that of the bar in the non-viscous fluid. This curve is also shown in Fig. 4.5. From the comparison between the total attenuation and the viscosity-induced attenuation it can be estimated up to which frequency it is valid to neglect longitudinal leakage.

It should also be noted that the exact numerical modelling of the attenuation requires knowledge of the longitudinal bulk velocity of the embedding liquid, since it influences the amount of longitudinal leakage. For this reason, and because it is limited to low frequencies, the use of T(0,1) is preferred to the use of L(0,1). However, the advantage of the longitudinal mode is that it is much easier to excite using piezoelectric excitation. One might therefore consider using L(0,1) for example if a magnetostrictive waveguide system is not available.

4.6.2 Experimental Validation

As a demonstration, experiments were conducted with Glycerol over a wide temperature range. The viscosity changes significantly with temperature and it is therefore possible to verify the method over a large viscosity range using a single material sample. As can be seen from Eq. (4.10), the dynamic viscosity decreases with increasing

temperature.

L(0,1) was excited at 0.2 MHz in a 0.25 mm radius steel wire. Since for this combination of frequency and radius the attenuation is to a good approximation caused by shear leakage only, the modelling here does not require accurate knowledge of the longitudinal velocity. Instead, any reasonable estimated value can be used for the modelling in DISPERSE. The Glycerol which was used in the following experiments presented in this work was an aqueous solution with a water content of approximately 0.7%. The beaker with the Glycerol was placed inside an oven, and the steel wire which was partly embedded in the Glycerol was fed through a hole in the oven wall so that the transducers could be placed outside the oven.

The results are shown in Fig. 4.6 together with literature data, which were available for an aqueous solution of Glycerol with 1% water content. Good agreement was obtained between literature and experimental data. Note that the viscosity is plotted on a logarithmic scale. Additionally, the viscosity of the same sample was measured using plate-plate and cone-plate rheometers, which also confirm the validity of the testing method.

4.7 Combined Measurement of Shear and Longitudinal Velocity

Even though it is not significant in the context of the cure monitoring application in this work, it is worth examining the possibility that L(0,1) may also be used to measure the longitudinal velocity of an embedding liquid. This is interesting from the point of view that thereby the material properties of a viscous liquid can be completely determined. The purpose of this analysis is to show an example procedure where two guided wave measurements can be combined to yield more information about an embedding material.

At higher frequencies, the attenuation of the longitudinal mode L(0,1) is caused by both shear and longitudinal leakage (see Fig. 4.4). If the viscosity is known from

a T(0,1)-attenuation measurement, the L(0,1)-attenuation at a given frequency is a function of the longitudinal bulk velocity only. This in turn allows for the prediction of the longitudinal bulk velocity from an L(0,1)-attenuation measurement.

4.7.1 Results for Water

As a first test, the method was used to determine the longitudinal velocity of water. Since the viscosity of water is very small (approximately 10^{-3} Pa s at 20° C [62]), its effect on the L(0,1)-attenuation may be neglected, so that the longitudinal velocity can be determined directly from the L(0,1)-attenuation measurement.

The longitudinal mode L(0,1) was excited in a 2.5 mm radius steel bar using a piezoelectric transducer, and embedded in distilled water at 20° C. Figure 4.7 shows the L(0,1)-attenuation as a function of the longitudinal velocity of water, modelled as an ideal liquid. From the slope of the curves it can be seen that the sensitivity increases with increasing frequency, and therefore measurements are more accurate at higher frequencies. Measurements were taken in the frequency-range between 0.1 MHz and 0.4 MHz, and the results are plotted in Fig. 4.8. The longitudinal velocity was determined at each frequency. The average of the values at frequencies between 0.25 MHz and 0.4 MHz was evaluated as $c_l = 1.439 \pm 0.027$ m/ms. This is within 3% of the literature value of 1.482 m/ms for distilled water at this temperature [62].

4.7.2 Results for Glycerol

The bar was embedded in Glycerol at 20.0 °C, and the L(0,1)-attenuation was measured at several frequencies. The viscosity was determined beforehand using the torsional mode in Sec. 4.5.2.

Figure 4.9 shows the predicted attenuation of L(0,1) as a function of the longitudinal velocity for a 2.5 mm radius steel bar embedded in Glycerol at different frequencies. The material properties for the steel bar are given in Tab. 4.1. From the slope of the dispersion curves it can be seen that the sensitivity of the attenuation concerning

the longitudinal velocity at lower frequencies is small, but increases towards higher frequencies. This is in accordance with the previously mentioned fact that at low frequencies, the attenuation is mainly sensitive to the shear properties of the viscous liquid and independent from the longitudinal properties. A satisfactory sensitivity is only obtained at higher frequencies.

The experimental data are shown in Fig. 4.2, and the viscosity was predicted as $\eta = 1.17 \pm 0.07\,\mathrm{Pa \cdot s}$. Figure 4.10 shows the results of the longitudinal measurements. The average value of the longitudinal bulk velocity was determined $c_l = 1.76 \pm 0.04\,\mathrm{m/ms}$, and the dispersion curve predicted with this value is also shown in Fig. 4.10. The value of longitudinal velocity is within approximately 10% of the literature value of $1.92\,\mathrm{m/ms}$ at $25^\circ\,\mathrm{C}$ [62].

4.7.3 Error Analysis for Longitudinal Measurements

These preliminary results show that it is in principle possible to measure the longitudinal velocity. The accuracy is however not as good as for viscosity measurements, even though the standard deviation is small. As mentioned before, the calculation of the longitudinal bulk velocity requires the exact knowledge of the dynamic shear viscosity and thus relies on the accuracy of the preceding T(0,1)-attenuation measurement. One significant error can be introduced due to the fact that any error in the calculation of the viscosity is carried through into the calculation of the longitudinal velocity. Therefore an independent measurement of the longitudinal velocity would be preferable. In fact, as was already pointed out by Nagy and Nayfeh, there is one point on the dispersion curve where the L(0,1)-attenuation is almost entirely caused by longitudinal leakage [60]. Figure 4.11 shows the attenuation dispersion curves for the 2.5 mm radius steel bar used in the experiments when embedded in Glycerol with different viscosities. As pointed out in the graph, there is one point where the attenuation is caused almost entirely by longitudinal leakage and the viscosity-induced attenuation is minimal. This is due to the fact that there are mainly radial displacements on the surface of the waveguide at this frequency-radius product, and only little displacements in the axial direction (see mode shape in Fig. 4.12). At this point the longitudinal velocity can be determined

independently from the viscosity, thereby reducing errors. However, L(0,1) is very dispersive at this point, which makes the testing difficult. The feasibility of using this point should be further evaluated in future.

Errors could also be caused by waveguide anisotropy. Wires are drawn during manufacture, and therefore may to a certain degree exhibit a transversely isotropic behaviour [51]. The waveguide properties were obtained assuming that the material is isotropic, and here only two constants have to be determined in order to fully characterise the waveguide (see Sec. 3.4). This is not true if the waveguide material is transversely isotropic, since then 5 constants of the complex stiffness tensor C_{ij} instead of two for the isotropic case are needed to determine the waveguide properties (see, for example, [25]). Nevertheless, the shear velocity in the axial direction is governed by the constant C_{66} only and is measured as such. Therefore, the propagation characteristics of T(0,1) are correctly modelled, and hence there would be no error in the viscosity calculations. However, the propagation of L(0,1) is governed by more than one constant, and the modelling assuming isotropy of the waveguide may be erroneous. Determining all the elastic constants of transversely isotropic waveguide material experimentally is difficult, and is subject to future research.

4.8 Summary

It has been shown in this chapter that it is possible to use the guided wave attenuation in embedded waveguides to accurately measure material properties such as the material properties of a viscous liquid.

Both the fundamental longitudinal and torsional modes are sensitive to the shear properties of the medium surrounding the waveguide. The analytical predictions using the software DISPERSE allow a quantitative evaluation without the use of asymptotic formulas or calibration liquids. Further validation of the attenuation technique for the measurement of shear velocity in the case where the embedding material is solid are given in Sec. 6.5.

The possibility to measure the longitudinal properties of the embedding viscous liquid using L(0,1) at higher frequencies has also been examined. Since the attenuation of L(0,1) at higher frequencies is caused by both shear and longitudinal bulk waves, the shear viscosity is determined in a separate experiment, using either T(0,1) or L(0,1) at lower frequencies. The experimental results are not as accurate as for the viscosity measurements. This may be due to the fact that errors in the viscosity measurements are carried through to the calculation of the longitudinal velocity and that the sensitivity of the attenuation to the longitudinal velocity is very small at lower frequencies. Also, the waveguide material may exhibit anisotropic behaviour.

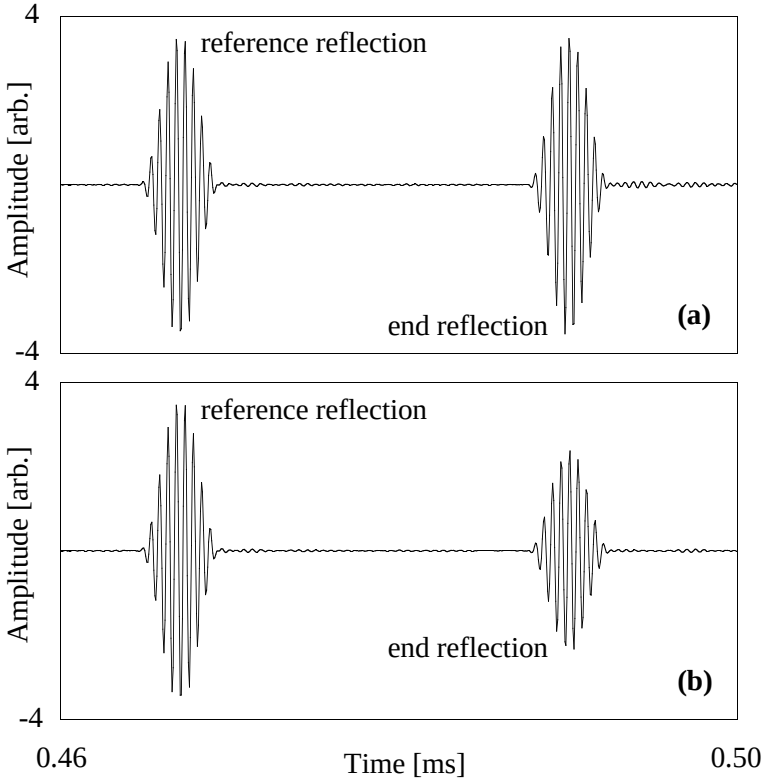

Figure 4.1: Typical time trace of T(0,1) in a steel wire (a) before, and (b) after embedding in Glycerol.

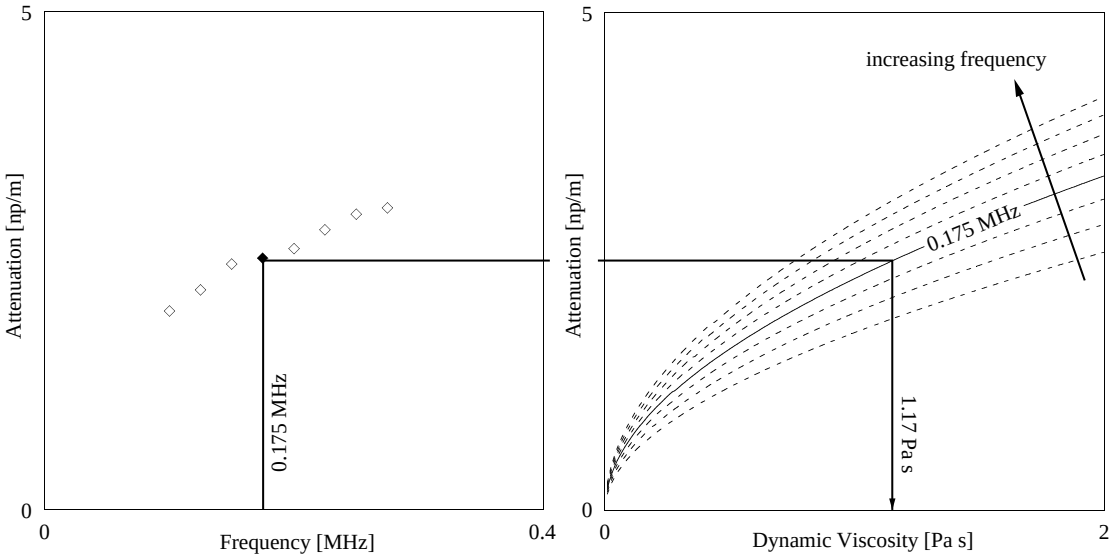

Figure 4.2: Illustration of the determination of shear viscosity from an attenuation measurement. Plot (a) shows actual measurements of T(0,1)-attenuation in a 1 mm radius steel bar embedded in Glycerol at 20 °C in the frequency range of 0.1–0.275 MHz in steps of 0.025 MHz (see Tab. 4.1 for the material properties). Plot (b) are predictions of T(0,1)-attenuation as a function of the shear viscosity at exactly the measured frequencies. The solid line in (b) corresponds to the example frequency of 0.175 MHz. At this frequency, the measured viscosity is 1.17 Pa·s.

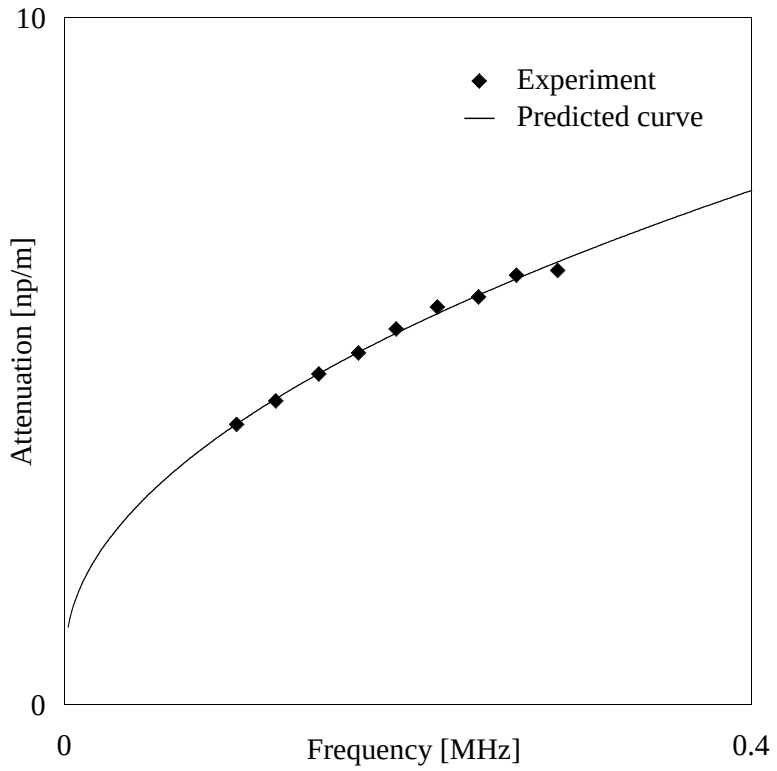

Figure 4.3: Measured T(0,1)-attenuation for a 0.5 mm radius steel wire embedded in the commercial Cannon VP450 viscosity standard at 21 °C. The predicted dispersion curve (solid line) was calculated using the average of viscosity ($\eta = 1.42 \pm 0.03$Pa·s) obtained from all measurement points. The density of the viscosity standard was 887 kg/m^3, and the material properties for steel are given in Tab. 4.1.

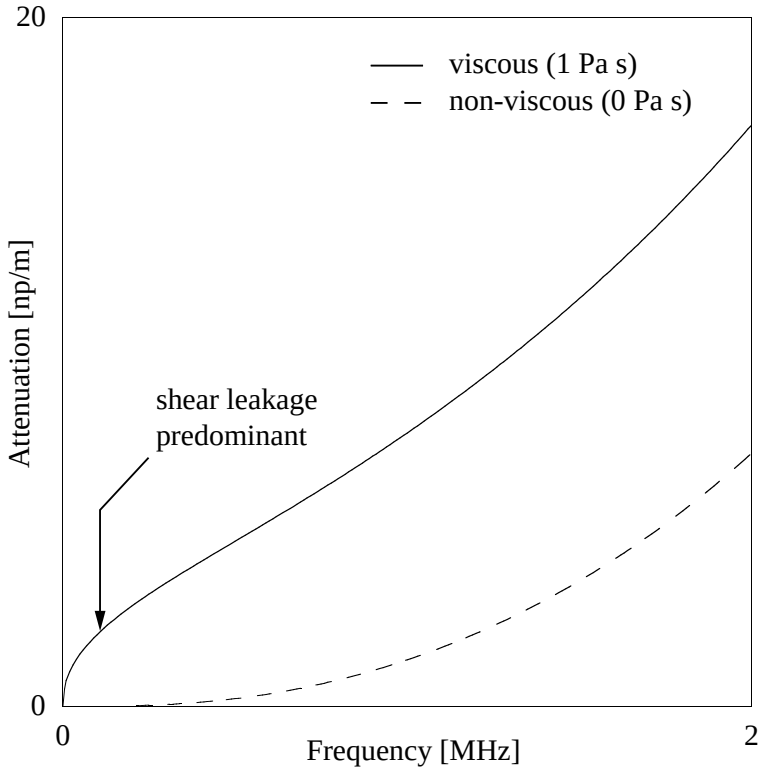

Figure 4.4: Predicted attenuation dispersion curves of L(0,1) in a 0.25 mm radius steel wire embedded in a viscous and a hypothetical non-viscous Glycerol. The material properties are listed in Tab. 4.1. At low frequencies, attenuation is almost entirely due to shear leakage when the liquid is viscous. In the non-viscous case, attenuation is solely due to longitudinal leakage.

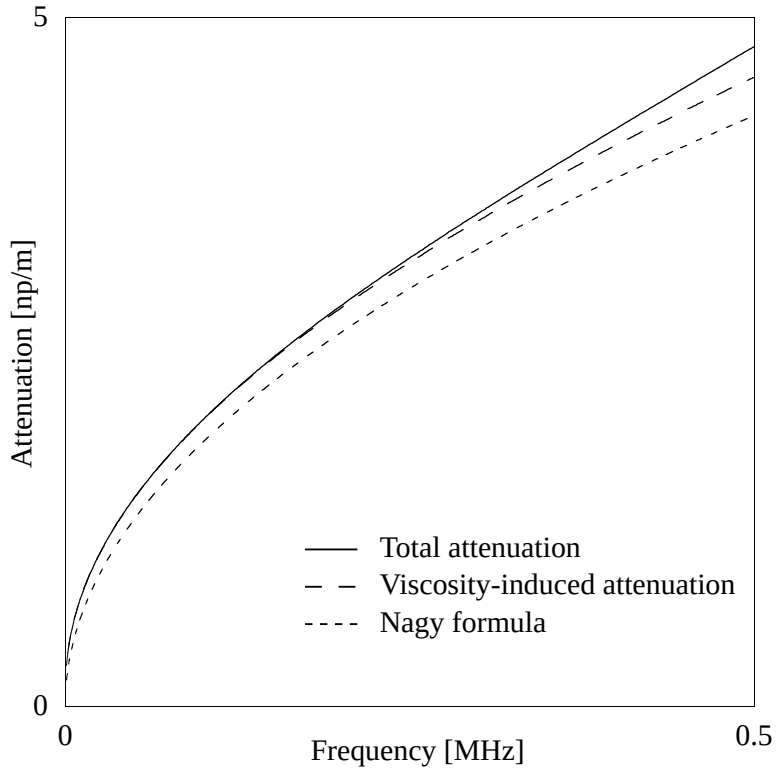

Figure 4.5: Predicted attenuation dispersion curve of L(0,1) in a 0.25 mm radius steel wire embedded in Glycerol with a dynamic viscosity of 1 Pa·s. The solid line includes both shear and longitudinal leakage. By subtracting the attenuation caused by longitudinal leakage (non-viscous case) from the total attenuation, the viscosity-induced attenuation is obtained. The attenuation predicted by Nagy's approximate formula is also shown.

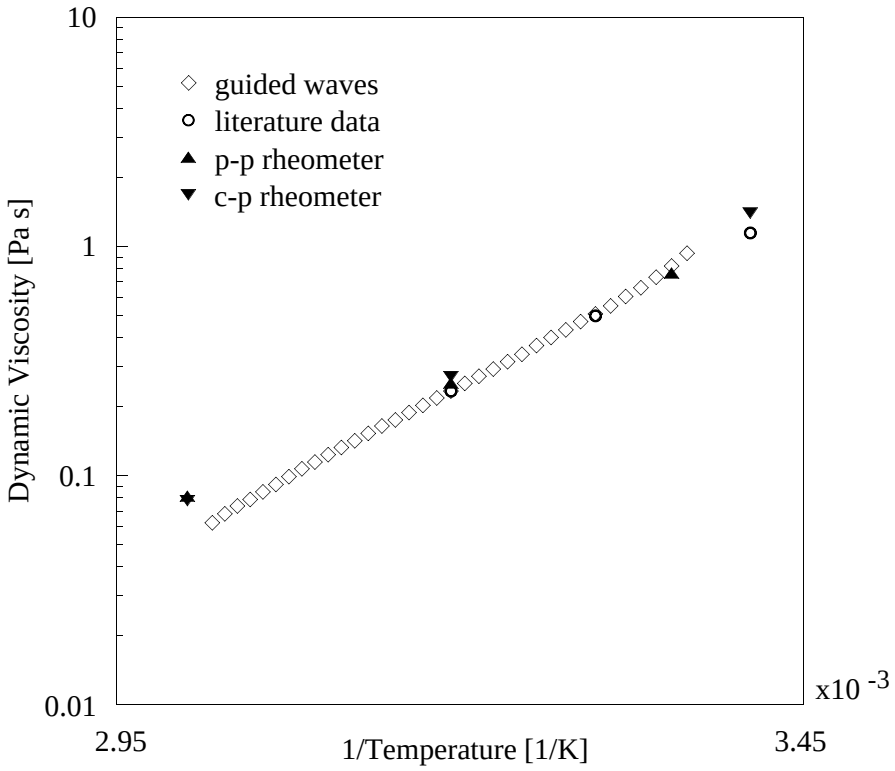

Figure 4.6: Viscosity of an aqueous solution of Glycerol with 0.7% water content measured at different temperatures using L(0,1) (guided waves) together with plate-plate (p-p), cone-plate (c-p) rheometer data, as well as literature values available for an aqueous solution of Glycerol with 1% water content.

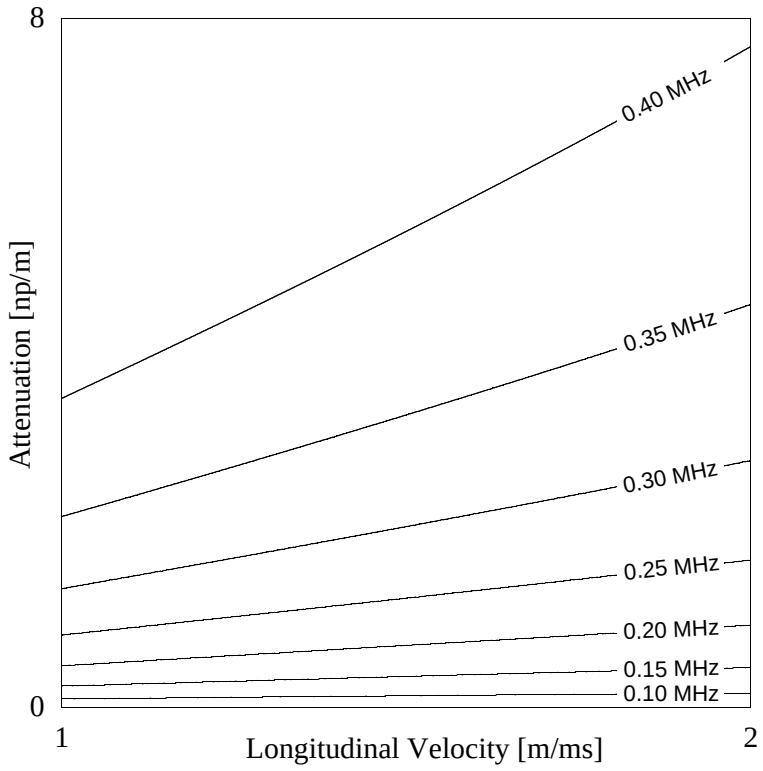

Figure 4.7: Predicted attenuation dispersion curves of L(0,1) at different frequencies for a 2.5 mm radius steel bar embedded in water. The material properties for steel are given in Tab. 4.1, and water is modelled as an ideal liquid with a density of $\rho = 1000\,\mathrm{kg/m^3}$.

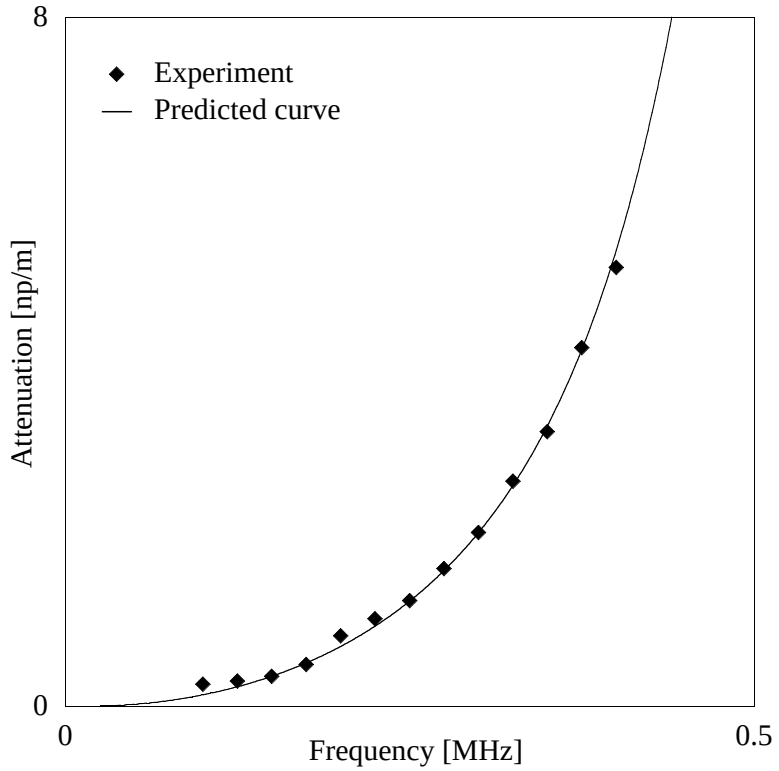

Figure 4.8: Measured L(0,1)-attenuation for a 2.5 mm radius steel bar embedded in distilled water at 20.0 °C at different frequencies. The predicted dispersion curve (solid line) was calculated using the average value of the longitudinal velocity of water obtained from the measured points between 0.25 MHz and 0.4 MHz ($c_l = 1.439 \pm 0.027\,\mathrm{m/ms}$). The material properties for steel are given in Tab. 4.1.

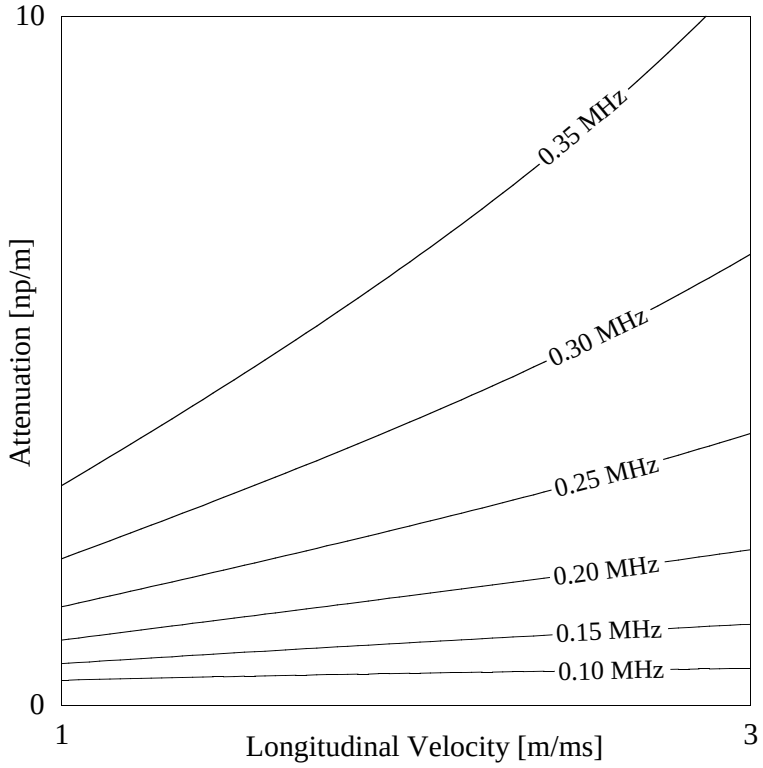

Figure 4.9: Predicted attenuation dispersion curves of L(0,1) at different frequencies for a 2.5 mm radius steel bar embedded in Glycerol with a viscosity of 1.17 Pa·s. The material properties for steel are given in Tab. 4.1.

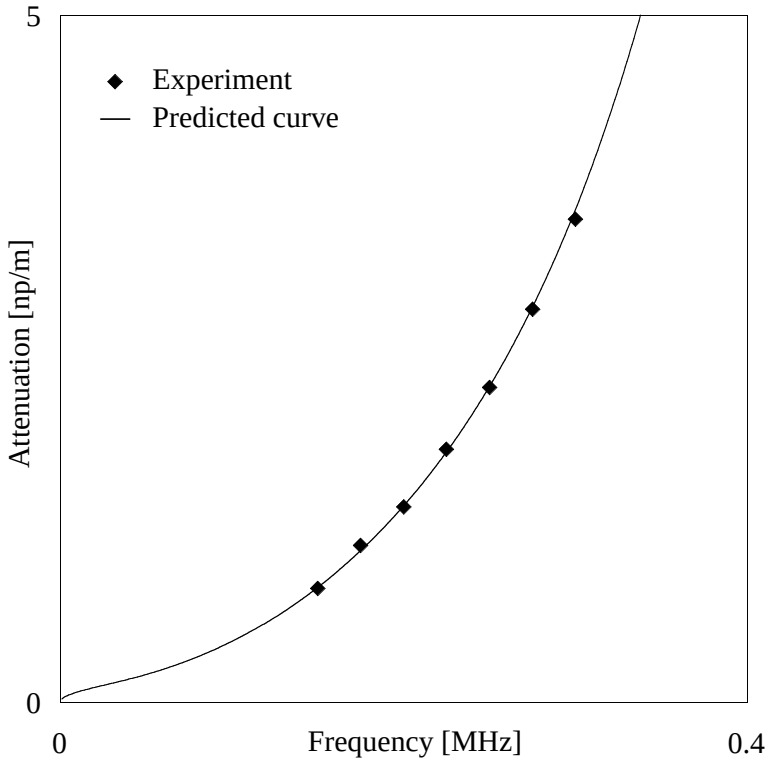

Figure 4.10: Measured L(0,1)-attenuation for a 2.5 mm radius steel bar embedded in Glycerol at 20.0 °C at different frequencies. The predicted dispersion curve (solid line) was calculated using the average value of the longitudinal velocity of Glycerol obtained from all measured points ($c_l = 1.76 \pm 0.04\,\mathrm{m/ms}$). The material properties for steel are given in Tab. 4.1.

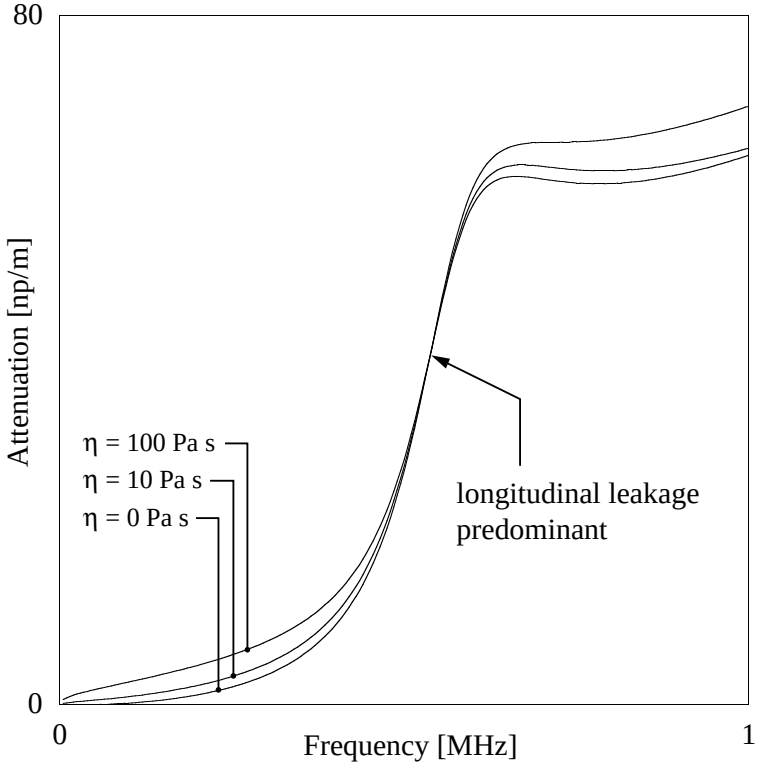

Figure 4.11: Predicted attenuation of L(0,1) for a 2.5 mm radius steel bar embedded in Glycerol with different assumed viscosities. As pointed out in the graph, even for high values of viscosity the attenuation is almost entirely caused by longitudinal leakage around a frequency of 0.54 MHz.

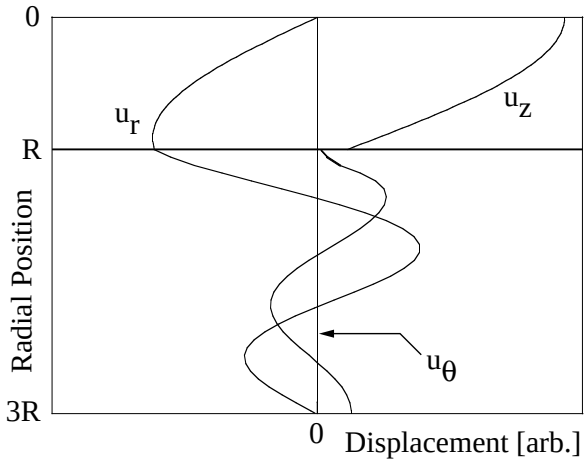

Figure 4.12: Mode shape of L(0,1) in a 2.5 mm radius steel bar embedded in a hypothetical non-viscous Glycerol at 0.54 MHz. It can be seen that the displacements at the surface of the waveguide are mainly in the radial direction.

Chapter 5

Reflection Coefficient Method

5.1 Background

As mentioned in the introduction in Ch. 1, two effects influence guided wave propagation when a waveguide is partly embedded in another material. Firstly, as discussed in Ch. 4, the guided wave will be attenuated in the embedded part. Secondly, because of the change in surface impedance at the point where the waveguide enters the embedding material, the guided wave will be reflected and also scattered through mode conversion. That both these effects can be used to monitor the curing process of epoxy resins was first discussed by Papadakis [63]. However, the results presented were of a qualitative nature. As has been seen in Ch. 4, in order to make quantitative predictions, the guided wave attenuation can be calculated if the acoustic properties of all the materials in the guided wave system are known; indeed the attenuation is an integral part of the dispersion curve calculation. To predict the scattering of a guided wave which is incident from the free section of the waveguide at a change in surface impedance is more difficult, and this problem is addressed in this chapter.

Apart from measuring material properties by embedding a waveguide in the material under investigation, there are many other circumstances when the application of a guided wave system to solve a practical problem involves a waveguide which is partly free and partly embedded. Examples include the testing of partly buried pipes for corrosion [26], or the detection of defects in rockbolts in mining roofs by access to their protruding end [64]. In all these cases, depending on the waveguide

mode, the frequency, and the geometry and the material properties of the waveguide, reflection will occur at the entry point. In many cases, a reflection from the entry point is undesirable, because it either interferes with other signals of interest, or can even make it impossible to test for defects in the embedded section if the reflection coefficient is so high that only little energy is transmitted. However, there are circumstances in which the presence of an entry reflection is advantageous. Examples are, as mentioned above, the cure monitoring of solidifying materials, or liquid level measurements [36].

Most of these applications usually involve the use of a cylindrical waveguide. Some theoretical work has been done on scattering from discontinuities in single and layered plates [65, 66, 67, 68], but less attention has been given to scattering problems in cylindrical waveguides. Zemanek [69] treated the case of guided waves being scattered from the end of a cylinder; the scattering of guided waves from circumferential cracks in hollow cylinders was presented by Ditri [70] and Bai *et al.* [71]. Engan [44] examined the scattering of torsional waves from a step change in the waveguide diameter. The theoretical work in this thesis is based on some of the techniques presented in these references.

Finite Element (FE) modelling presents another possibility of solving scattering problems and has been employed by several researchers [72, 73, 74]. This is most useful when analytical solutions cannot be found. However, the computational analysis can be tedious and does not easily yield insight to the physics of the scattering process. Moreover, numerical problems occur when dealing with materials that have small shear velocities, for example epoxy resins at the beginning of cure. It is therefore desirable to find an alternative solution for the cases where FE modelling is slow or not feasible. In the following, FE modelling will be used for the validation of the theoretical results where the material parameters allow for this.

First, a theoretical analysis will show the equivalence between the S-parameter formalism introduced by Auld [65] and a solution which is based on matching the fields at the interface between the free and the embedded sections of a cylindrical

waveguide when a guided wave is incident from the free section. A complete modal solution is then given, and the results will be compared to FE modelling. It will be shown that in most cases of interest, only a small number of waveguide modes has to be considered in the modal solution. The following theoretical analysis is completely general, but for the purpose of demonstrating its validity and in view of the cure monitoring application presented in Ch. 6, the examples given will be restricted to the case where the lowest order longitudinal mode is incident. It will be shown that the entry reflection is sensitive to the shear velocity of the embedding material, and can therefore be used for its measurement.

5.2 Theoretical Basis

5.2.1 Introduction

For the following derivations it is necessary to review and introduce the notation used to describe guided modes in cylindrical structures. Time-harmonic propagation in the direction of the axis of the waveguide is considered, which is chosen to be the z-direction in the cylindrical coordinates (r,Θ,z). A guided wave solution is represented by sets of wavenumber and frequency combinations for which the particle velocity and stresses satisfy the chosen boundary conditions at the surfaces of the cylindrical structure [20, 69]. The particle velocity, $\mathbf{v}$, and stress tensor, $\mathbf{T}$, are given by the expressions

$$\mathbf{v}_n^\nu(r,\theta,z,t) = \mathbf{v}_n^\nu(r)\, e^{i\nu\theta}\, e^{-i(k_n z-\omega t)}, \tag{5.1}$$

$$\mathbf{T}_n^\nu(r,\theta,z,t) = \mathbf{T}_n^\nu(r)\, e^{i\nu\theta}\, e^{-i(k_n z-\omega t)}, \tag{5.2}$$

where ω is the circular frequency, k_n is the complex wavenumber in the propagation direction, and ν is the angular wavenumber. Firstly, because of the continuity of the field variables in the angular direction, ν must be a whole number; it is commonly referred to as the circumferential order. For example, longitudinal and torsional modes are of circumferential order zero, which means that the modal fields are axi-symmetric. For flexural modes, $\nu \geq 1$. Secondly, at each frequency, there is an infinite number of modes of a given circumferential order, which are solutions to the dispersion equation. The counter n is used to label a single waveguide mode of a

given circumferential order. Therefore, the notation (ν,n) denotes the nth mode of circumferential order ν. These two indices completely identify a waveguide mode.

This notation is similar to that originally introduced by Silk and Bainton [23]. In fact, for flexural modes, the notation (ν,n) is equivalent to the bracketed term in the notation F(ν,n) used by Silk and Bainton. However, for circumferential order zero the notation (ν,n) does not distinguish between longitudinal, L, and torsional, T, modes. In order to relate the counting number n used in this paper to the notation of Silk and Bainton in the case where $\nu = 0$, the following convention can be made:

$n = 1 \rightarrow$ L(0,1)

$n = 2 \rightarrow$ T(0,1)

$n = 3 \rightarrow$ L(0,2)

$n = 4 \rightarrow$ T(0,2)

$n = 5 \rightarrow$ L(0,3)

...

Both of the above notations will be used where appropriate. The variation of the modal fields in the plane perpendicular to the propagation direction z is determined by the radial distribution functions, $\mathbf{v}_n^\nu(r)$ and $\mathbf{T}_n^\nu(r)$, respectively. They are in general complex functions, and are referred to as the mode shapes of the waveguide mode (see Sec. 2.3.3).

5.2.2 Normal Mode Theory

The main tool for analysing scattering problems is the normal mode theory. It was laid out for layered waveguides by Auld [65], and a brief review of the fundamental framework is given here. In normal mode theory, one makes use of the fact that an arbitrary field distribution can be expanded into so-called normal modes. These normal modes have to fulfill two main conditions. Firstly, the set of modes has to be *complete*, which means that they are sufficient, by superposition, to describe any arbitrary field distribution. Questions of this kind have been treated by Kirmann [75] for Lamb modes. In this work, completeness of the waveguide modes

is assumed. Secondly, the modes must be *orthogonal*, which means that the expansion of an arbitrary field into normal modes is unique. Mode orthogonality for layered plate waveguides was treated by Auld [65], and was generalised to cylindrical waveguides by Ditri [70]. To be strict, the orthogonality relationships derived in these references are actually *bi-orthogonality* relationships, since they involve two different fields, namely the particle velocity and stress fields. We now review and consider these relationships.

For any two solutions, "1" and "2", of the particle velocity and stress fields to the field equations, a real reciprocity relationship of the following form holds [65]:

$$\nabla \cdot \{\mathbf{v}_1 \cdot \mathbf{T}_2 - \mathbf{v}_2 \cdot \mathbf{T}_1\} = 0, \tag{5.3}$$

where the indices denote the solutions "1" and "2", respectively, and ∇ is the divergence operator. Within a volume V, where the material parameters are the same for solutions "1" and "2", one can therefore write for a given frequency ω :

$$\int_V \nabla \cdot \{\mathbf{v}_1 \cdot \mathbf{T}_2 - \mathbf{v}_2 \cdot \mathbf{T}_1\}\, dV = 0. \tag{5.4}$$

Consider the case where solution "1" is given by mode (ν,n), and solution "2" is given by mode (μ,m). Equation (5.4) then becomes

$$\int_V \nabla \cdot \{\mathbf{v}_n^\nu \cdot \mathbf{T}_m^\mu - \mathbf{v}_m^\mu \cdot \mathbf{T}_n^\nu\}\, dV = 0. \tag{5.5}$$

Using the two-dimensional Gauss theorem, it follows that

$$\int_S \frac{\partial}{\partial z} \{\mathbf{v}_n^\nu \cdot \mathbf{T}_m^\mu - \mathbf{v}_m^\mu \cdot \mathbf{T}_n^\nu\}\, \hat{\mathbf{z}}\, dS + \oint_C \{\mathbf{v}_n^\nu \cdot \mathbf{T}_m^\mu - \mathbf{v}_m^\mu \cdot \mathbf{T}_n^\nu\}\, \hat{\mathbf{r}}\, dl = 0, \tag{5.6}$$

where S is the cross-section of the waveguide and C is a line along the circumference of S, $\hat{\mathbf{z}}$ is a unit vector in the propagation direction, and $\hat{\mathbf{r}}$ is a unit vector in the outward radial direction (see Fig. 5.1). For a free waveguide the tractions normal to the surface of the waveguide vanish, $\mathbf{T} \cdot \hat{\mathbf{r}} = 0$, whereas for a waveguide with rigid boundaries the particle velocities vanish, $\mathbf{v} = 0$. Therefore, in both cases equation (5.6) reduces to

$$\int_S \frac{\partial}{\partial z} \{\mathbf{v}_n^\nu \cdot \mathbf{T}_m^\mu - \mathbf{v}_m^\mu \cdot \mathbf{T}_n^\nu\}\, \hat{\mathbf{z}}\, dS = 0. \tag{5.7}$$

The dependence of the field variables on z implies that

$$-i(k_n + k_m) \int_S \{\mathbf{v}_n^\nu \cdot \mathbf{T}_m^\mu - \mathbf{v}_m^\mu \cdot \mathbf{T}_n^\nu\} \, \hat{\mathbf{z}} \, dS = 0. \tag{5.8}$$

From this equation, either $k_n = -k_m$, or the integral vanishes:

$$\int_S \{\mathbf{v}_n^\nu \cdot \mathbf{T}_m^\mu - \mathbf{v}_m^\mu \cdot \mathbf{T}_n^\nu\} \, \hat{\mathbf{z}} \, dS = 0 \qquad \text{for } k_n \neq -k_m. \tag{5.9}$$

This is known as the real orthogonality relationship. However, there are cases where two different modes can have $k_n = -k_m$. In this case, orthogonality between the two modes is restored by a second relationship, called the angular orthogonality relationship. For $k_n = -k_m$, the integral on the left-hand side of equation (5.9) can be further evaluated (omitting the time dependence):

$$\int_S \{\mathbf{v}_n^\nu \cdot \mathbf{T}_m^\mu - \mathbf{v}_m^\mu \cdot \mathbf{T}_n^\nu\} \, \hat{\mathbf{z}} \, dS = \int_0^R \{\mathbf{v}_n^\nu \cdot \mathbf{T}_m^\mu - \mathbf{v}_m^\mu \cdot \mathbf{T}_n^\nu\} \, (r) \hat{\mathbf{z}} \, r \, dr \int_{\Theta_0}^{\Theta_0 + 2\pi} e^{i(\nu+\mu)\theta} \, d\Theta. \tag{5.10}$$

The integration over Θ shows that

$$\int_S \{\mathbf{v}_n^\nu \cdot \mathbf{T}_m^\mu - \mathbf{v}_m^\mu \cdot \mathbf{T}_n^\nu\} \, \hat{\mathbf{z}} \, dS = 0 \qquad \text{for } \nu \neq -\mu. \tag{5.11}$$

This is called the angular orthogonality relationship. It is slightly different from the one presented by Ditri [70], which, written in a form compatible with the mode naming here, states that:

$$\int_{\Theta_0}^{\Theta_0 + 2\pi} \mathbf{v}_n^\nu \cdot \mathbf{T}_m^\mu \, d\Theta = 0 \qquad \text{for } \nu \neq \mu. \tag{5.12}$$

This is due to the fact that the modal distribution fields in Ref. [70] are assumed to vary trigonometrically as either $\sin(\nu\Theta)$ or $\cos(\nu\Theta)$. However, in our case, in which we think of the circumferential order as an angular wavenumber, the more general exponential notation, $e^{i\nu\Theta}$, is more consistent. The sine or cosine notation describes a standing wave solution along the circumference of the waveguide, and can be thought of as a superposition of two spiral waves of the exponential type, each in the opposite angular direction.

The orthogonality relationship for a cylinder in vacuum can thus be written in the following form:

$$\int_S \{\mathbf{v}_n^\nu \cdot \mathbf{T}_m^\mu - \mathbf{v}_m^\mu \cdot \mathbf{T}_n^\nu\}\,\hat{\mathbf{z}}\,dS = 0 \qquad \text{for } k_n \neq -k_m \text{ or } \nu \neq -\mu. \tag{5.13}$$

5.2.3 Normalisation Procedure

For the following scattering analysis it is convenient to introduce two more notations. Firstly, we introduce the convention

$$-k_n = k_{-n}, \tag{5.14}$$

to label the same mode propagating in the negative z-direction. We refer to modes whose energy propagates in the positive axial direction as "forward" modes, and those whose energy propagates in the negative axial direction as "backward" modes. Non-propagating and inhomogeneous modes, however, do not propagate energy in any direction (see App. A for a more detailed explanation). One can imagine these modes as local vibrations, which exist only at waveguide discontinuities such as the edge of a plate or the surface discontinuity considered in this work. In this case, the equivalent to a forward mode is a non-propagating or inhomogeneous mode which is attenuated in the positive z-direction.

Secondly, it is convenient to define the quantity $Q_{m\,n}^{\mu\,\nu}$ as

$$Q_{m\,n}^{\mu\,\nu} = -\frac{1}{4}\int_S \{\mathbf{v}_m^\mu \cdot \mathbf{T}_n^\nu - \mathbf{v}_n^\nu \cdot \mathbf{T}_m^\mu\}\hat{\mathbf{z}}\,dS. \tag{5.15}$$

For propagating modes, that means for modes with purely real wavenumber, the fields satisfy the following relations ([65], p. 188):

$$\mathbf{v}_{-m}^{-\mu}(r,\Theta) = -\mathbf{v}_m^{\mu\,*}(r,\Theta), \tag{5.16}$$

$$\mathbf{T}_{-m}^{-\mu}(r,\Theta) = \mathbf{T}_m^{\mu\,*}(r,\Theta). \tag{5.17}$$

Evaluating $Q_{m\,-m}^{\mu\,-\mu}$ with these relationships yields

$$Q_{m\,-m}^{\mu\,-\mu} = -\frac{1}{4}\int_S \{\mathbf{v}_m^\mu \cdot \mathbf{T}_{-m}^{-\mu} - \mathbf{v}_{-m}^{-\mu} \cdot \mathbf{T}_m^\mu\}\hat{\mathbf{z}}\,dS \tag{5.18}$$

$$= -\frac{1}{4}\int_S \{\mathbf{v}_m^\mu \cdot \mathbf{T}_m^{\mu\,*} + \mathbf{v}_m^{\mu\,*} \cdot \mathbf{T}_m^\mu\}\hat{\mathbf{z}}\,dS$$

$$= P_{m\,m}^{\mu\,\mu}, \tag{5.19}$$

where $P^{\mu\,\mu}_{m\,m}$ is the average power flow of mode (μ,m) propagating in the z-direction. The average power flow is the real part of the complex power flow.

In scattering analysis, the modal fields are usually normalised such that the average power flow through the cross-section of the waveguide is unity. However, non-propagating and inhomogeneous modes do not carry power. Therefore they cannot be normalised this way. Some researchers used the complex power flow instead, noting that non-propagating modes can be normalised to the imaginary unit [44]. However, in order to be able to apply the same normalisation procedure to all modes, the modal fields will be normalised here such that

$$Q^{\mu\,-\mu}_{m\,-m} = 1. \tag{5.20}$$

Moreover, propagating modes with purely real wavenumbers are still power normalised by this expression, since

$$Q^{\mu\,-\mu}_{m\,-m} = P^{\mu\,\mu}_{m\,m} = 1. \tag{5.21}$$

5.3 Scattering Analysis

5.3.1 Problem Statement

An infinitely long cylindrical waveguide is half free and half embedded in another material, and the embedding material is assumed to extend infinitely in the radial direction (see Fig. 5.2). A propagating waveguide mode is incident from the free section of the waveguide and will be scattered and mode converted at the interface between the free and the embedded section due to the change in surface impedance. Two different approaches to solving the problem will be taken in the following. In Sec. 5.3.2, we follow the S-parameter formalism laid out by Auld [65]. This analysis yields an exact scattering formula for a guided wave incident from the free section of the cylinder. In Sec. 5.3.3 it is shown that the same expression can be obtained by simply matching the fields over the cross-section of the waveguide, thus neglecting the free surface of the embedding material at the interface between the free and the embedded section. Finally, in Sec. 5.3.4, a complete modal solution is given using a more intuitive notation.

5.3.2 S-Parameter Formalism

The first derivation follows closely the S-parameter method presented by Auld for the calculation of scattering coefficients [65]. Consider a waveguide with and without surface loading as depicted in Fig. 5.3. At any point within the volume V the reciprocity relation holds:

$$\nabla \cdot \{\mathbf{v}_1 \cdot \mathbf{T}_2 - \mathbf{v}_2 \cdot \mathbf{T}_1\} = \nabla \cdot \{\cdots\} = 0, \tag{5.22}$$

where the expression $\{\mathbf{v}_1 \cdot \mathbf{T}_2 - \mathbf{v}_2 \cdot \mathbf{T}_1\}$ has been replaced by $\{\cdots\}$ for brevity. Therefore

$$\int_V \nabla \cdot \{\cdots\}\, dV = 0. \tag{5.23}$$

Let the fields denoted by "1" be the solution for the case when there is no surface loading, and solution "2" for the case with surface loading. This is valid, because the reciprocity relation holds anywhere in the waveguide where the material parameters are the same. The surface S of the volume V can be divided into three regions (see Fig. 5.3):

$$S = \partial V = S_l + S_r + S_c, \tag{5.24}$$

where S_l is the plane on the left hand side, S_r the plane on the right hand side, and S_c the surface on the circumference of the cylindrical waveguide. By applying the Gauss theorem, it follows that

$$-\int_{S_l} \{\cdots\}\hat{\mathbf{z}}\, dS + \int_{S_r} \{\cdots\}\hat{\mathbf{z}}\, dS + \int_{S_c} \{\cdots\}\hat{\mathbf{r}}\, dS = 0. \tag{5.25}$$

Consider a mode ($\bar{\mu}$,$\bar{m}$) incident from the left, indicated as such with a bar superscript for clarity. For solution "1", no scattering occurs, and the fields on S_l and S_r can be written in the following form:

$$\mathbf{v}_1 = \begin{cases} \mathbf{v}_{\bar{m}}^{\bar{\mu}} & \text{on } S_l \\ S_{\bar{m}\bar{m}}^{\bar{\mu}\bar{\mu}} \mathbf{v}_{\bar{m}}^{\bar{\mu}} & \text{on } S_r \end{cases}, \tag{5.26}$$

$$\mathbf{T}_1 = \begin{cases} \mathbf{T}_{\bar{m}}^{\bar{\mu}} & \text{on } S_l \\ S_{\bar{m}\bar{m}}^{\bar{\mu}\bar{\mu}} \mathbf{T}_{\bar{m}}^{\bar{\mu}} & \text{on } S_r \end{cases}. \tag{5.27}$$

Here, the scattering coefficients, S, called the S-parameters, are defined in a slightly different way than in Ref. [65]. For example $S^{\nu\,\mu}_{n\,m}$ refers to the coefficient for mode (μ,m) being incident from the left and mode (ν,n) being scattered (transmitted) to the right hand side of the discontinuity, whereas $S^{-\nu\,\mu}_{-n\,m}$ denotes the reflection of ($-\nu$,$-n$) to the left hand side for an incident mode (μ,m). The mode propagation does not depend on z except for attenuation, whose effect is implicitly contained in the expressions for the particle velocity and the stress. Therefore it follows that

$$S^{\bar{\mu}\,\bar{\mu}}_{\bar{m}\,\bar{m}} = 1. \tag{5.28}$$

Solution "2" must take the reflected and transmitted modes into account. For reasons which will become clear later, mode ($\bar{\nu}$,$\bar{n}$) is chosen to be incident from the left. The fields can be expressed as:

$$\mathbf{v}_2 = \begin{cases} \mathbf{v}^{\bar{\nu}}_{\bar{n}} + \sum\limits_{n,\nu} S^{\nu\,\bar{\nu}}_{-n\,\bar{n}} \mathbf{v}^{\nu}_{-n} & \text{on } S_l \\ \sum\limits_{n,\nu} S^{\nu\,\bar{\nu}}_{n\,\bar{n}} \mathbf{v}^{\nu}_{n} & \text{on } S_r \end{cases} \tag{5.29}$$

$$\mathbf{T}_2 = \begin{cases} \mathbf{T}^{\bar{\nu}}_{\bar{n}} + \sum\limits_{n,\nu} S^{\nu\,\bar{\nu}}_{-n\,\bar{n}} \mathbf{T}^{\nu}_{-n} & \text{on } S_l \\ \sum\limits_{n,\nu} S^{\nu\,\bar{\nu}}_{n\,\bar{n}} \mathbf{T}^{\nu}_{n} & \text{on } S_r \end{cases} . \tag{5.30}$$

The sums run over negative and positive angular wavenumbers, but over positive integers n only. Evaluating the integral from equation (5.25) on S_r yields:

$$\int\limits_{S_r} \{\cdots\}\hat{\mathbf{z}}\, dS = \int\limits_{S_r} \sum_{n,\nu} S^{\nu\,\bar{\nu}}_{n\,\bar{n}} \{\mathbf{v}^{\bar{\mu}}_{\bar{m}} \cdot \mathbf{T}^{\nu}_{n} - \mathbf{v}^{\nu}_{n} \cdot \mathbf{T}^{\bar{\mu}}_{\bar{m}}\}\hat{\mathbf{z}}\, dS \tag{5.31}$$

$$= 0. \tag{5.32}$$

Note at this stage that therefore equation (5.25) becomes

$$\int\limits_{S_l} \{\mathbf{v}^{\mu}_{m} \cdot \mathbf{T}_2 - \mathbf{v}_2 \cdot \mathbf{T}^{\mu}_{m}\}\hat{\mathbf{z}}\, dS = \int\limits_{S_c} \{\mathbf{v}^{\mu}_{m} \cdot \mathbf{T}_2 - \mathbf{v}_2 \cdot \mathbf{T}^{\mu}_{m}\}\hat{\mathbf{r}}\, dS. \tag{5.33}$$

Further evaluating the integral on S_l one obtains:

$$-\int\limits_{S_l} \{\cdots\}\hat{\mathbf{z}}\, dS = -\int\limits_{S_l} \{\mathbf{v}^{\bar{\mu}}_{\bar{m}} \cdot \mathbf{T}^{\bar{\nu}}_{\bar{n}} - \mathbf{v}^{\bar{\nu}}_{\bar{n}} \cdot \mathbf{T}^{\bar{\mu}}_{\bar{m}}\}\hat{\mathbf{z}}\, dS \tag{5.34}$$

$$-\int\limits_{S_l} \sum_{n,\nu} S^{\nu\,\bar{\nu}}_{-n\,\bar{n}} \{\mathbf{v}^{\bar{\mu}}_{\bar{m}} \cdot \mathbf{T}^{\nu}_{-n} - \mathbf{v}^{\nu}_{-n} \cdot \mathbf{T}^{\bar{\mu}}_{\bar{m}}\}\hat{\mathbf{z}}\, dS$$

$$= 4S^{-\bar{\mu}\,\bar{\nu}}_{-\bar{m}\,\bar{n}}.$$

Equation (5.25) therefore becomes:

$$4S_{-\bar{m}\,\bar{n}}^{-\bar{\mu}\,\bar{\nu}} + \int_{S_c} \{\mathbf{v}_{\bar{m}}^{\bar{\mu}} \cdot \mathbf{T}_2 - \mathbf{v}_2 \cdot \mathbf{T}_{\bar{m}}^{\bar{\mu}}\}\hat{\mathbf{r}}\, dS = 0. \tag{5.35}$$

This is valid for an arbitrary mode ($\bar{\mu}$,$\bar{m}$), which can be renamed (μ,m). Thus

$$S_{-m\,\bar{n}}^{-\mu\,\bar{\nu}} = -\frac{1}{4}\int_{S_c} \{\mathbf{v}_m^{\mu} \cdot \mathbf{T}_2 - \mathbf{v}_2 \cdot \mathbf{T}_m^{\mu}\}\hat{\mathbf{r}}\, dS. \tag{5.36}$$

This is a general scattering formula for an incident mode ($\bar{\nu}$,$\bar{n}$) being scattered into mode ($-\mu$,$-m$). It is equivalent to the general scattering formula presented by Auld. This is an exact formula, and the S-Parameters can be calculated if the fields in "2" are known. It can be seen that the scattering coefficients will depend on the total waveguide surface area covered by the embedding material. To obtain the case considered here, the integral over the surface S_c has to be extended to $z = \infty$.

5.3.3 Alternative Calculation

It will be shown in this section that the same result can be obtained by simply matching the boundary conditions at the interface where the waveguide enters the embedding material. Only the mode shapes over the adjoining cross-section have to be considered in order to obtain an exact solution for modes which are incident from the free section. Thus, the free surface of the embedding material at $z = 0$ does not have to be considered.

It is assumed that the field in the waveguide on the left hand side of the interface between the vacuum and embedded parts, "1", is a superposition of the waveguide modes in the free cylinder (see Fig. 5.4); we refer to these here as the "vacuum" modes. The particle velocity and stress fields "1" are expressed in terms of the incident vacuum mode ($\bar{\nu}$,$\bar{n}$), propagating in the $+z$-direction, and the sum of all reflected vacuum modes, propagating in the $-z$-direction. The sums run over negative and positive angular wavenumbers, but over positive axial wavenumbers only:

$$\mathbf{v}_1 = \mathbf{v}_{\bar{n}}^{\bar{\nu}} + \sum_{\nu,n} S_{-n\,\bar{n}}^{\nu\,\bar{\nu}}\, \mathbf{v}_{-n}^{\nu}, \tag{5.37}$$

$$\mathbf{T}_1 = \mathbf{T}_{\bar{n}}^{\bar{\nu}} + \sum_{\nu,n} S_{-n\,\bar{n}}^{\nu\,\bar{\nu}}\, \mathbf{T}_{-n}^{\nu}. \tag{5.38}$$

We will make assumptions about the fields in "2" later in Sec. 5.3.4, but for the moment the fields created in the embedded section by the incident mode will just be denoted by $\mathbf{v}_2$ and $\mathbf{T}_2$. The boundary conditions within the waveguide at the interface between the free and the embedded section must be fulfilled,

$$\mathbf{v}_1 = \mathbf{v}_2, \tag{5.39}$$

$$\mathbf{T}_1 \cdot \hat{\mathbf{z}} = \mathbf{T}_2 \cdot \hat{\mathbf{z}}, \tag{5.40}$$

where $\hat{\mathbf{z}}$ is the unit vector in the z-direction. The boundary conditions therefore become

$$\mathbf{v}_{\bar{n}}^{\bar{\nu}} + \sum_{\nu,n} S_{-n\,\bar{n}}^{\nu\,\bar{\nu}}\, \mathbf{v}_{-n}^{\nu} = \mathbf{v}_2, \tag{5.41}$$

$$\mathbf{T}_{\bar{n}}^{\bar{\nu}} + \sum_{\nu,n} S_{-n\,\bar{n}}^{\nu\,\bar{\nu}}\, \mathbf{T}_{-n}^{\nu} = \mathbf{T}_2. \tag{5.42}$$

Multiplying the first equation by $\mathbf{T}_m^{\mu}$ and the second equation by $\mathbf{v}_m^{\mu}$, one obtains

$$\mathbf{v}_{\bar{n}}^{\bar{\nu}} \cdot \mathbf{T}_m^{\mu} + \sum_{\nu,n} S_{-n\,\bar{n}}^{\nu\,\bar{\nu}}\, \mathbf{v}_{-n}^{\nu} \cdot \mathbf{T}_m^{\mu} = \mathbf{v}_2 \cdot \mathbf{T}_m^{\mu}, \tag{5.43}$$

$$\mathbf{v}_m^{\mu} \cdot \mathbf{T}_{\bar{n}}^{\bar{\nu}} + \sum_{\nu,n} S_{-n,\bar{n}}^{\nu,\bar{\nu}}\, \mathbf{v}_m^{\mu} \cdot \mathbf{T}_{-n}^{\nu} = \mathbf{v}_m^{\mu} \cdot \mathbf{T}_2. \tag{5.44}$$

Subtracting equation (5.44) from (5.43) yields:

$$\{\mathbf{v}_{\bar{n}}^{\bar{\nu}} \cdot \mathbf{T}_m^{\mu} - \mathbf{v}_m^{\mu} \cdot \mathbf{T}_{\bar{n}}^{\bar{\nu}}\} + \sum_{\nu,n} S_{-n\,\bar{n}}^{\nu\,\bar{\nu}} \{\mathbf{v}_{-n}^{\nu} \cdot \mathbf{T}_m^{\mu} - \mathbf{v}_m^{\mu} \cdot \mathbf{T}_{-n}^{\nu}\} = \{\mathbf{v}_2 \cdot \mathbf{T}_m^{\mu} - \mathbf{v}_m^{\mu} \cdot \mathbf{T}_2\}. \tag{5.45}$$

In order to take advantage of the real orthogonality relation, this is integrated over the cross-section S. The terms on the left hand side can be examined separately:

$$\int_S \{\mathbf{v}_{\bar{n}}^{\bar{\nu}} \cdot \mathbf{T}_m^{\mu} - \mathbf{v}_m^{\mu} \cdot \mathbf{T}_{\bar{n}}^{\bar{\nu}}\} \hat{\mathbf{z}}\, dS = 0, \tag{5.46}$$

$$\int_S \sum_{\nu,n} S_{-n\,\bar{n}}^{\nu\,\bar{\nu}} \{\mathbf{v}_{-n}^{\nu} \cdot \mathbf{T}_m^{\mu} - \mathbf{v}_m^{\mu} \cdot \mathbf{T}_{-n}^{\nu}\} \hat{\mathbf{z}}\, dS = 4 S_{-m\,\bar{n}}^{-\mu\,\bar{\nu}}. \tag{5.47}$$

Replacing this into equation (5.45), the S-parameter for the scattered mode $(-\mu,-m)$ and the incident mode $(\bar{\nu},\bar{n})$ is obtained:

$$S_{-m\,\bar{n}}^{-\mu\,\bar{\nu}} = -\frac{1}{4} \int_S \{\mathbf{v}_m^{\mu} \cdot \mathbf{T}_2 - \mathbf{v}_2 \cdot \mathbf{T}_m^{\mu}\} \hat{\mathbf{z}}\, dS. \tag{5.48}$$

The surface S is equivalent to S_l in equation (5.33). Since the boundary conditions are fulfilled on this surface, the fields $\mathbf{v}_2$ and $\mathbf{T}_2$ on S in the two approaches to calculate the scattering coefficients are the same. Thus it follows that the expressions in equations (5.36) and (5.48) are equivalent.

Similarly, by multiplying equations (5.41) and (5.42) by $\mathbf{T}^{\mu}_{-m}$ and $\mathbf{v}^{\mu}_{-m}$, respectively, it can be shown that

$$-\frac{1}{4}\int_S \{\mathbf{v}_2 \cdot \mathbf{T}^{\mu}_{-m} - \mathbf{v}^{\mu}_{-m} \cdot \mathbf{T}_2\}\hat{\mathbf{z}}\, dS = \begin{cases} 1 & \text{for } \mu = -\bar{\nu} \text{ and } m = \bar{n} \\ 0 & \text{else.} \end{cases} \tag{5.49}$$

Thus, the scattering parameters for the case of a mode incident from the free part of the waveguide can be calculated by just considering the integrals over the cross-section of the waveguide, ignoring the free surface of the embedding material. However, this is not necessarily true for the case when a mode is incident from the embedded section of the waveguide. For this to be true, orthogonality would have to be shown for these modes. Whether or not it is sufficient only to consider the adjoining cross-section in the embedded part would then depend on the nature of this orthogonality relationship (see also App. B).

5.3.4 Modal Solution

In fact, the equations (5.48) and (5.49) already give the complete solution to the problem in the case where modes are incident from the free section of the waveguide. However, it cannot readily be seen how to calculate the scattering parameters from this. Therefore in this section the complete modal solution for the case of modes which are incident from the free section of the waveguide will be derived in a more intuitive notation similar to that presented by Engan [44].

In order to do this, one has to assume that the field in the embedded part of the waveguide can be represented by a superposition of waveguide modes (ν',n'). These modes are in general leaky modes, and there exist proofs of orthogonality in the literature for leaky layered waveguides [76, 77]. However, it has to be mentioned that it is usually assumed that the wavenumber in the propagation direction is

either purely real or purely imaginary, or that the fields vanish far away from the interface. This is not necessarily true, as leaky guided waves have a complex axial wave number. If they have a purely real wavenumber, they are essentially non-leaky modes. Also, the plane waves leaking into the surrounding material must be inhomogeneous in order to fulfill Snell's law, which states that the real and the imaginary part of the complex wavenumber in the axial direction of both the guided wave and the leaking inhomogeneous plane wave must be identical (see Fig. 5.5). For inhomogeneous plane waves in an elastic medium, the attenuation direction must be normal to the propagation direction [14] (see also Sec. 2.2). In plate-like structures, where the partial waves are plane waves, this causes the fields in the embedding material to increase exponentially in the outward direction normal to the interface between the waveguide and the embedding material. The situation is similar, though more complicated, in the case of a cylindrical waveguide. Here, the dependence on the radial position is given by Bessel-functions, whose argument is complex when there is attenuation. Hence, the fields actually tend to infinity far away from the interface. Nevertheless, in this section, orthogonality of these modes is assumed. As explained in more detail in section 5.4, this is found to be the case to a satisfactory degree of accuracy. For more detailed comments on waveguide orthogonality in embedded waveguides refer to App. B.

We will restrict the following derivation to longitudinal modes, which are of circumferential order zero. The superscripts denoting the circumferential order will be omitted from now on, since by symmetry order zero modes can only scatter into modes of the same order, and also torsional modes cannot scatter into longitudinal modes and vice versa.

If the amplitudes of incoming modes are denoted by a's, and scattered mode amplitudes are denoted by b's, the particle velocity and stress fields in the free section of the bar can be written as

$$\mathbf{v}_1 = \sum_m a_m \mathbf{v}_m + b_{-m} \mathbf{v}_{-m}, \tag{5.50}$$

$$\mathbf{T}_1 = \sum_m a_m \mathbf{T}_m + b_{-m} \mathbf{T}_{-m}. \tag{5.51}$$

The index of the mode amplitudes indicate in which direction the scattered mode is propagating. As stated earlier, for non-propagating and inhomogeneous modes, this is chosen to be the direction of the decay. It is now assumed that the fields being excited in "2" are composed of the modes of an embedded cylinder, denoted by a dash:

$$\mathbf{v}_2 = \sum_{m'} b_{m'} \mathbf{v}_{m'}, \tag{5.52}$$

$$\mathbf{T}_2 = \sum_{m'} b_{m'} \mathbf{T}_{m'}. \tag{5.53}$$

Note that there is no incident mode from the embedded section. In principle, the sums in equations (5.50) – (5.53) extend over an infinite number of modes. However, for the numerical calculations, these sums have to be truncated after a certain mode M.

One can collect the incoming and scattered mode amplitudes in column vectors, and they are related to each other by a scattering matrix in the following way:

$$\begin{bmatrix} b_{-1} \\ b_{-2} \\ \vdots \\ b_{-M} \\ b_{1'} \\ b_{2'} \\ \vdots \\ b_{M'} \end{bmatrix} = \begin{bmatrix} S_{-1\,1} & S_{-1\,2} & \cdots & S_{-1\,M} \\ S_{-2\,1} & S_{-2\,2} & \cdots & S_{-2\,M} \\ \vdots & \vdots & \ddots & \vdots \\ S_{-M\,1} & S_{-M\,2} & \cdots & S_{-M\,M} \\ S_{1'\,1} & S_{1'\,2} & \cdots & S_{1'\,M} \\ S_{2'\,1} & S_{2'\,2} & \cdots & S_{2'\,M} \\ \vdots & \vdots & \ddots & \vdots \\ S_{M'\,1} & S_{M'\,2} & \cdots & S_{M'\,M} \end{bmatrix} \begin{bmatrix} a_1 \\ a_2 \\ \vdots \\ a_M \end{bmatrix} = \begin{bmatrix} \\ [S_{-m\,n}] \\ \\ \\ \\ \\ [S_{m'\,n}] \\ \\ \end{bmatrix} \begin{bmatrix} a_1 \\ a_2 \\ \vdots \\ a_M \end{bmatrix}. \tag{5.54}$$

The scattering sub-matrices $S_{-m\,n}$ and $S_{m'\,n}$ are $M \times M$ matrices, whereas the full scattering matrix is an $M \times 2M$ matrix. First, the boundary conditions are applied on the interface between the free and the embedded section (see equations (5.39) and (5.40), respectively):

$$\sum_m a_m \mathbf{v}_m + b_{-m} \mathbf{v}_{-m} = \sum_{m'} b_{m'} \mathbf{v}_{m'}, \tag{5.55}$$

$$\sum_m a_m \mathbf{T}_m + b_{-m} \mathbf{T}_{-m} = \sum_{m'} b_{m'} \mathbf{T}_{m'}. \tag{5.56}$$

Multiplying equation (5.55) by $\mathbf{T}_{-n}$ and equation (5.56) by $\mathbf{v}_{-n}$, and subtracting (5.56) from (5.55) yields:

$$\sum_m a_m \left(\mathbf{v}_m \cdot \mathbf{T}_{-n} - \mathbf{v}_{-n} \cdot \mathbf{T}_m\right) + \sum_m b_{-m} \left(\mathbf{v}_{-m} \cdot \mathbf{T}_{-n} - \mathbf{v}_{-n} \cdot \mathbf{T}_{-m}\right) = \sum_{m'} b_{m'} \left(\mathbf{v}_{m'} \cdot \mathbf{T}_{-n} - \mathbf{v}_{-n} \cdot \mathbf{T}_{m'}\right). \quad (5.57)$$

Then, by integrating over the cross-section of the waveguide one makes use of the orthogonality relation (5.13), and some terms in equation (5.57) vanish. Noting that the fields are normalised according to equation (5.20), it follows that

$$\begin{aligned} a_n &= -\frac{1}{4} \sum_{m'} b_{m'} \int_S \left(\mathbf{v}_{m'} \cdot \mathbf{T}_{-n} - \mathbf{v}_{-n} \cdot \mathbf{T}_{m'}\right) \cdot \hat{\mathbf{z}} \, dS \quad (5.58) \\ &= -\sum_{m'} b_{m'} \, Q_{-n\,m'}. \end{aligned}$$

This can be written in matrix form:

$$\begin{bmatrix} a_1 \\ a_2 \\ \vdots \\ a_M \end{bmatrix} = - \begin{bmatrix} Q_{-1\,1'} & Q_{-1\,2'} & \cdots & Q_{-1\,M'} \\ Q_{-2\,1'} & Q_{-2\,2'} & \cdots & Q_{-2\,M'} \\ \vdots & \vdots & \ddots & \vdots \\ Q_{-M\,1'} & Q_{-M\,2'} & \cdots & Q_{-M\,M'} \end{bmatrix} \begin{bmatrix} b_{1'} \\ b_{2'} \\ \vdots \\ b_{M'} \end{bmatrix} \quad (5.59)$$

In an abbreviated notation, this is

$$[a_n] = -[Q_{-n\,m'}][b_{m'}], \quad (5.60)$$

so

$$[b_{m'}] = -[Q_{-n\,m'}]^{-1}[a_n]. \quad (5.61)$$

Secondly, multiplying equation (5.55) by $\mathbf{T}_n$ and equation (5.56) by $\mathbf{v}_n$, and subtracting (5.56) from (5.55) yields:

$$\sum_m a_m \left(\mathbf{v}_m \cdot \mathbf{T}_n - \mathbf{v}_n \cdot \mathbf{T}_m\right) + \sum_m b_{-m} \left(\mathbf{v}_{-m} \cdot \mathbf{T}_n - \mathbf{v}_n \cdot \mathbf{T}_{-m}\right) = \sum_{m'} b_{m'} \left(\mathbf{v}_{m'} \cdot \mathbf{T}_n - \mathbf{v}_n \cdot \mathbf{T}_{m'}\right). \quad (5.62)$$

Again, this is integrated over the cross-section of the waveguide, and some terms vanish due to orthogonality. One is left with the following equation:

$$\begin{aligned} b_{-n} &= \frac{1}{4} \sum_{m'} b_{m'} \int_S \left(\mathbf{v}_{m'} \cdot \mathbf{T}_n - \mathbf{v}_n \cdot \mathbf{T}_{m'}\right) \cdot \hat{\mathbf{z}} \, dS \quad (5.63) \\ &= \sum_{m'} b_{m'} \, Q_{n\,m'}. \end{aligned}$$

Replacing n by m, this can be abbreviated to give

$$[b_{-m}] = [Q_{m\,m'}][b_{m'}]. \tag{5.64}$$

Recalling equation (5.61), the coefficients b_{-m} are calculated as follows:

$$[b_{-m}] = -[Q_{m\,m'}][Q_{-n\,m'}]^{-1}[a_n]. \tag{5.65}$$

Finally, equations (5.61) and (5.65) can be combined to give the solution to the scattering problem:

$$\begin{bmatrix} [b_{-m}] \\ [b_{m'}] \end{bmatrix} = \begin{bmatrix} -[Q_{m\,m'}][Q_{-n\,m'}]^{-1} \\ -[Q_{-n\,m'}]^{-1} \end{bmatrix} [a_n] \tag{5.66}$$

By comparison with the general scattering formula in equation (5.54), it follows that

$$[S_{-m\,n}] = -[Q_{m\,m'}][Q_{-n\,m'}]^{-1} \tag{5.67}$$

and

$$[S_{m'\,n}] = -[Q_{-n\,m'}]^{-1}. \tag{5.68}$$

The scattering amplitudes are here calculated using a normalisation procedure for the modal fields according to equation (5.20). For the interpretation of the results it is convenient to state the scattering amplitudes in terms of the scattered power. The power normalised scattering coefficients, denoted by capital letters A_m, B_{-m}, and $B_{m'}$ respectively, are obtained from the amplitudes calculated here, a_m, b_{-m}, and $b_{m'}$ respectively, by multiplying by the square-root of the power of the corresponding mode, for example:

$$B'_m = b'_m \sqrt{P_{m'\,m'}}. \tag{5.69}$$

Note that for non-propagating and inhomogeneous modes, $P_{m\,m} = 0$, and therefore no power is carried away from the scattering region by these modes.

5.4 Numerical Implementation

The calculation of the elements of the scattering matrix requires the knowledge of the radial distribution functions of the modes which are included in the solution. In

most cases, a closed form analytical solution of the modal fields cannot be obtained, and the dispersion equation has to be solved numerically. DISPERSE has been used to trace the dispersion curves and to obtain the particle velocity and stress mode shapes of each mode. These mode shapes are used to calculate the elements of the scattering matrix. Typically, a resolution of 200 points over the radius of the waveguide was found to give a reasonable accuracy for the calculation of the integrals.

A key assumption in the modal analysis is that the fields in the embedded section can be represented by a sum of waveguide modes of the infinitely long embedded cylinder. Orthogonality is assured for the waveguide modes of the free bar (see equation 5.13). This relationship was checked numerically using the mode shapes predicted by DISPERSE for the free bar modes in order to give an indication as to how accurate the numerical values are. It was found that, once the fields have been normalised according to equation (5.20), the value of $Q^{\nu\,\mu}_{n\,m}$ for two orthogonal modes was of the order of 10^{-5}. Strictly this should be zero, so this value represents the error in the calculations. For the equivalent modes of a cylinder embedded in an epoxy resin as modelled in this work, $Q^{\nu'\,\mu'}_{n'\,m'}$ was found to be typically of the order of 10^{-3}. Given the increased difficulty in finding the complex roots of the dispersion equation and the limited precision of the complex Bessel functions which have to be employed, this seems to be an acceptably small value. However, this numerical demonstration is not a proof, and it has to be accepted that orthogonality for leaky waves may have to be evaluated including the embedding half-space and not only the waveguide cross-section.

The dispersion curves can be presented in a 3-dimensional representation, showing the real and imaginary part of the axial wavenumber, k, in the propagation direction against the frequency f. A summary of the material parameters used in the analysis is given in Tab. 5.1.

Onoe and Zemanek have presented the dispersion curves for a cylinder in vacuum in great detail, showing the real, imaginary and complex branches [18, 69]. The curves will therefore only be shown here for explanatory purposes. Real, imaginary

Table 5.1: Material parameters used for the analysis in Ch. 5.

Material	c_l [m/s]	c_s [m/s]	ρ [kg/m^3]
Steel	5960	3260	7932
Epoxy	2610	1000	1170
Material "a"	2000	1000	1000
Material "b"	4000	1000	1000

and complex branches correspond respectively to propagating, non-propagating and inhomogeneous solutions. As pointed out in Ref. [69], for every complex branch there exists an exact negative complex conjugate one. A 3-dimensional representation of the first three longitudinal modes is given in Fig. 5.6 (a). Consider for example the modes L(0,2) and L(0,3), which are both inhomogeneous between zero frequency and the cut-off frequency of L(0,2). In the inhomogeneous region, their imaginary wavenumbers are identical, whereas the real parts of their wavenumber have equal magnitude and opposite sign. As an example, in order to show this relationship more clearly, the real wavenumber of the forward modes is plotted together with that of the backward modes in Fig. 5.6 (b). The wavenumber of a forward mode has the same magnitude and opposite sign to the wavenumber of the corresponding backward mode, and therefore this graph allows a direct comparison of the real wavenumbers of L(0,2) and L(0,3) in the inhomogeneous region by looking at L(0,2) and -L(0,3). The latter overlap completely in the inhomogeneous region, therefore the real wavenumbers of L(0,2) and L(0,3) are the exact negatives of each other.

The real part of the wavenumber is non-zero for an inhomogeneous mode and represents a phase propagation, whereas the imaginary part represents a spatial attenuation. However, as a simple power flow calculation shows, inhomogeneous modes do not carry power.

The situation is different for an embedded waveguide. Figure 5.7 (a) shows the dispersion curves for the longitudinal modes L(0,1) to L(0,5) in a 1 mm steel cylinder

embedded in an epoxy resin. In addition, the projection of these curves onto the real wavenumber - frequency plane is given in Fig. 5.7 (b), which also shows the modes which propagate in the negative direction. From this it can clearly be seen that the modes which are equivalent to the inhomogeneous modes in the free cylinder do not have a negative complex conjugate counterpart. Instead, the modes seem to repel each other. Also, a power flow calculation shows that these modes do in general propagate power, and are therefore propagating modes.

The case where the embedding material is replaced by a perfectly rigid material is also discussed. It presents an appropriate validation case for two reasons. Firstly, the validity of the modal solution can be tested without the assumption of orthogonality in the embedded case since the modes in a cylinder with rigid boundaries obey the orthogonality relationship presented in equation (5.7). Secondly, a rigid boundary can be thought of as a limiting case of infinite impedance of the embedding material. The dispersion curves are shown in Fig. 5.8. Note that there are only non-propagating and inhomogeneous longitudinal modes in the low-frequency region and no propagating longitudinal modes. The consequences arising from this are studied in Sec. 5.6.

In order to ensure that the sub-matrix $[Q_{m'-n}]$ in equation (5.60) is invertible, the equivalent number of modes in the embedded cylinder to that in the free cylinder will be included in the modal solution.

The energy balance is often used as an estimate of the error in the calculation of the scattering coefficients [67], and it is adopted here. After normalisation of the coefficients to represent the scattered power (see equation (5.69)), the error ε in the total power flow is given by:

$$\sum_{m} \left(|A_m|^2 - |B_{-m}|^2 \right) - \sum_{m'} |B_{m'}|^2 = \varepsilon. \tag{5.70}$$

For an exact solution, $\varepsilon = 0$. It should be noted that the sums only run over propagating modes, since non-propagating and inhomogeneous modes do not contribute to the power flow. Also note that modes propagating in the $-z$-direction have neg-

ative power flow. In the case that only one mode of unit power flow is incident, this simplifies to:

$$1 - \sum_{m} |B_{-m}|^2 - \sum_{m'} |B_{m'}|^2 = \varepsilon. \tag{5.71}$$

5.5 Comparison to Finite Element Modelling

5.5.1 Finite Element Technique

The Finite Element (FE) method is used here to validate the results obtained from the modal scattering analysis, which will be shown later in Sec. 5.6. The FE analysis was carried out using the software FINEL, developed at Imperial College [78]. It performs efficient modelling of elastic wave propagation using a time-marching procedure. For general reference of the FE-method refer to Refs. [79, 80].

To model a circular waveguide, four-noded quadrilateral elements were used in axisymmetry. To obtain a stable solution, it is necessary to meet a number of requirements. Firstly, for numerical accuracy, the element size should at most be one eighth of the shortest wavelength present. Then, the error, for example, in guided wave speed is smaller than 0.5% [72]. Similarly, a rapidly varying mode shape over the cross-section has to be accounted for correctly by a sufficient number of elements. Thirdly, the time step for the marching procedure should not exceed 0.8 times the time in which the fastest wave can propagate one element length.

5.5.2 2D Finite Element Model

The nature of the reflection of L(0,1) from the point where a steel cylinder enters a much larger diameter cylinder of epoxy resin was examined in detail. A schematic of the FE model is shown in Fig. 5.9. The analysis covered the range from 0 – 0.5 MHz, and three different wire radii were modelled: 0.25 mm, 0.5 mm and 0.75 mm. A 1-cycle Hanning-windowed piston profile of 0.2 MHz centre frequency was applied at the free end of the cylinder in order to obtain the reflection coefficient over a range of frequencies. Because the excitation has no significant energy above the cut-off frequency of L(0,2) for the chosen waveguide diameters, the only propagating mode

excited by this configuration is L(0,1). One has to make sure that the reflection from the entry point is not disturbed by any other reflections from the end of the cylinder or from the boundaries of the epoxy by choosing a sufficiently long embedded length and a sufficiently large outer diameter of the epoxy. The monitoring point for displacements in the axial direction is half way between the free end of the cylinder and the entry point.

A typical FE time-trace is shown in Fig. 5.10. The first signal corresponds to the incident mode L(0,1) passing the monitoring point, whereas the second signal is the reflection from the entry point into the epoxy. Reflections from the other boundaries of the embedded part of the model come later and can thus be neglected. A Fourier transform was then applied to both signals individually. The division of the amplitude spectrum of the reflected signal by the amplitude spectrum of the incident signal gives the frequency dependent amplitude reflection coefficient.

The reflection from the interface between a cylinder with a free boundary and one with a perfectly rigid boundary was also examined. A schematic of the FE model is given in Fig. 5.11. The radius of the steel cylinder in this analysis was 0.5 mm. Since there are no propagating modes in the cylinder with rigid boundaries in the frequency-range covered by the analysis, only non-propagating and inhomogeneous modes will be excited in the rigid region. In order to observe these modes, the displacements were additionally monitored in the axial direction in steps of 0.125 mm to the right hand side of the interface on the axis of the cylinder.

5.6 Results

5.6.1 Cylinder With Rigid Boundary

The reflection of L(0,1) from the interface between a cylinder with free and rigid boundaries is considered mainly for the validation of the modal solution, since orthogonality is given in the cylinder with the rigid surface. However, it also gives some insight into the behaviour of non-propagating and inhomogeneous modes.

As stated earlier, there are no propagating modes at low frequencies in the rigid cylinder. When the L(0,1) mode is incident from the free cylinder, then total reflection must occur at the interface at frequencies which are below the cut-off frequency of L(0,2) in the free and L(0,1) in the rigid cylinder. This is because the non-propagating and inhomogeneous modes in both parts of the cylinder cannot propagate energy away from the scattering region. Therefore, both the modal and the FE solution should give a reflection coefficient of unity. As shown in Fig. 5.12, this is confirmed by both methods to a high degree of numerical accuracy. To obtain this result, only the propagating L(0,1) mode in the free section and the non-propagating L(0,1) in the rigid section were included in the modal solution.

The displacements in the z-direction on the axis of the cylinder with the rigid surface were also monitored in the FE analysis. They can be thought of as the superposition of the displacements of all the non-propagating and inhomogeneous modes excited at the interface. Figure 5.13 shows the displacements as a function of time at three different distances from the interface, which is located at $z = 0\,\text{mm}$. It can clearly be seen that there is no propagation, and the amplitude decreases with distance from the interface. These modes can therefore be thought of as local vibrations with a spatial attenuation away from the discontinuity. The decay of the displacement amplitude with respect to the distance from the interface at 0.2 MHz, obtained from the Fourier transform of the signal, is plotted in Fig. 5.14.

Zemanek [69] has already pointed out that inhomogeneous modes are always created in pairs with equal imaginary wavenumber but with real wavenumbers of opposite sign. This way, a spatially attenuated standing wave is set up which does not propagate energy. As an example for the free cylinder, L(0,2) and L(0,3) represent such a pair of inhomogeneous modes. Indeed, it was found in the calculations that the scattering parameters, b, of the corresponding inhomogeneous modes are to a high degree of accuracy identical.

As the total displacement, u, in the rigid part of the waveguide is a superposition of all the spatially decaying non-propagating and inhomogeneous modes involved, the

z-dependence of the modulus can be expressed in the form

$$\begin{aligned} u(z) &= \sum_{m'} u_{m'}(z) \\ &= \sum_{m'} |u_{m'}|\, e^{-i\xi_{m'}z}\, e^{-\alpha_{m'}z}, \end{aligned} \tag{5.72}$$

where ξ is the real wavenumber, and α is the attenuation (see also Sec. 2.3). Here, the time-dependence has been omitted. Since the inhomogeneous modes occur in pairs with real wavenumbers of opposite sign, this expression becomes

$$u(z) = \sum_{m'} |u_{m'}|\, \cos(\xi_{m'}z)\, e^{-\alpha_{m'}z}. \tag{5.73}$$

For non-propagating modes, the real wavenumber is zero, and the cosine takes the value unity. The values for the real wavenumber, ξ, and the attenuation, α, are obtained from DISPERSE, and a curve can be fitted to the FE results using the above equation, with the $|u_{m'}|$'s being the fitting parameters. It is found that, even though the modal solution gives accurate results when including only one non-propagating mode, the decay function cannot be satisfactorily fitted using only one mode (see Fig. 5.14). Instead, a minimum of 5 non-propagating and inhomogeneous modes is needed to obtain a precise fit. This means that, although the modal solution gives an accurate representation of the reflection coefficient when including a minimal number of modes, more modes might actually be significantly involved in the scattering process.

5.6.2 Scattering From Epoxy Loading

The different examples presented below are related to the application of a guided wave system to the cure monitoring of epoxy resins. A steel cylinder which is partly embedded in an epoxy resin is considered. The waveguide and the epoxy resin are modelled as purely elastic materials.

Figure 5.15 shows the modulus of the amplitude reflection coefficient for the lowest order longitudinal mode, L(0,1), in a 1 mm radius steel wire using the material properties given in Tab. 5.1 and using just the lowest order longitudinal mode in the embedded section in the modal solution. In the same plot, the FE results are

shown, and the agreement is very good. Including more inhomogeneous modes in the free section and the equivalent modes in the embedded section changes the reflection coefficient only by a negligible amount (not shown here). Therefore, the influence of these modes on the reflection coefficient is minimal in this case. This is in accordance with the findings of Engan in the case of the scattering of torsional modes from a step change in diameter [44], which suggest that only a few non-propagating modes are needed for a reasonably accurate description. The error in the power flow calculation was found to be of the order of $\varepsilon \approx 10^{-4} - 10^{-5}$, even with small numbers of inhomogeneous modes.

It is interesting to note that the amplitude reflection coefficient curve scales with the product of the frequency and the radius of the cylinder (see Fig. 5.16). This is not surprising as the reflection coefficient is calculated using the mode shapes, which, like the dispersion curves, scale with the frequency-radius product. This has been confirmed both with FE modelling and using the modal solution, although only the FE results are plotted in Fig. 5.16.

The power of the L(0,1)-mode at low frequency-radius products is distributed fairly evenly over the cross-section of the waveguide. However, the scattering occurs on the circumference of the waveguide. It seems reasonable that under these conditions the ratio of circumference to cross-sectional area roughly relates to the ratio of the scattered to the total power of the incident mode. It was found that in this case only the lowest order longitudinal mode plays a significant role in the scattering process, and therefore the ratio of scattered to total power governs the reflection coefficient. Because of the geometry, this ratio decreases with increasing radius. This explains why the reflection coefficient is large for low frequency-radius products, and falls off to low values at higher frequency-radius products.

The particle displacements of L(0,1) at the surface of the waveguide at very low frequencies are mainly in the axial direction. Therefore, guided wave attenuation is mostly caused by the leakage of shear waves and depends strongly on the shear velocity of the embedding material, and only to a small extent on its longitudinal

velocity. The situation is similar for the reflection coefficient. This is illustrated in Fig. 5.17, where the reflection coefficient for embedding materials with constant shear velocity and density but a 100% difference in the longitudinal velocity are shown. There is a negligible difference in the curves for the two materials. For a cure monitoring application, the change in shear properties with curing time is significant, and a significant change in the reflection coefficient is expected. Fig. 5.18 shows the amplitude reflection coefficient for different values of shear velocity, calculated using both the modal solution and FE modelling. The reflection coefficient increases with increasing shear velocity, since the difference in surface impedance between the free and the embedded cylinder increases. Therefore the reflection coefficient can be used to evaluate the shear properties of an embedding material.

5.7 Experimental Validation

For the experimental validation in this section the influence of the shear bulk attenuation on the reflection coefficient after the resin has fully cured is neglected, so the resin is modelled as an elastic material. The accuracy of this approximation is discussed in Sec. 6.4.

Figure 5.19(a) shows an example of an experimental time trace of L(0,1) in the free wire before embedding. It shows the reference reflection and the reflection from the end of the wire. The time trace after embedding is shown in Fig. 5.19(b), with the resin fully cured. Here the entry reflection is received at an earlier time because of the reduction in propagation distance.

Since piezoelectric transducers were used for these experiments, a narrow-band signal had to be chosen in order to prevent signal distortion due to the excitation of frequencies close to the resonance frequency of the transducer. Let the modulus of the Fourier transform of the reference reflection in the free and the embedded wire be denoted by A_0^{vac} and A_0^{emb}, respectively, the end reflection in the free wire by A^{vac} and the entry reflection in the embedded wire by A^{emb}. Then the reflection

coefficient R is calculated according to

$$R = \frac{A^{\mathrm{emb}}/A_0^{\mathrm{emb}}}{A^{\mathrm{vac}}/A_0^{\mathrm{vac}}}. \tag{5.74}$$

Experiments were conducted using the lowest order longitudinal mode, L(0,1). Two steel wires of different radius, $r = 0.125\,\mathrm{mm}$ and $r = 0.5\,\mathrm{mm}$, were embedded in the same sample of epoxy resin (Araldite 2012, Ciba Specialty Chemicals) in order to confirm the frequency-radius dependence of the reflection coefficient. Measurements were taken between 0.1 MHz and 0.55 MHz using narrow-band signals, and the reflection coefficient was evaluated at the centre frequencies.

In a separate experiment, the material properties of the cured epoxy sample were measured using conventional ultrasonic transducers in a through-transmission experiment at 0.05 MHz. The shear velocity was determined as $c_s = 0.885\,\mathrm{m/ms}$, and the density $\rho = 1170\,\mathrm{kg/m^3}$. Using these material properties, the reflection coefficient was predicted by means of FE modelling, assuming the epoxy to be perfectly elastic. The experimental results are plotted together with the predictions in Fig. 5.20. The agreement is very good, and it confirms the frequency-radius dependence of the reflection coefficient.

5.8 Summary

The scattering of guided waves in a free bar from the point where the waveguide enters an embedding material has been discussed. It has been shown that for a wave which is incident from the free section of the bar, a scattering formula equivalent to one derived using the S-Parameter formalism is obtained by matching the fields at the interface between the free and the embedded waveguide. A modal solution shows good agreement with results obtained from Finite Element modelling.

For the modal solution presented here, orthogonality of the leaky modes in the embedded waveguide is assumed and appears to be satisfied sensibly in the example which is studied. However, further research should investigate an orthogonality relationship for leaky waveguide modes. The mathematical form of such a relationship,

for example whether an integral form includes the embedding half-spaces or only the waveguide cross-section, determines the modal solution in the case where a guided wave is incident from the embedded section of the waveguide.

Orthogonality is given in the case where the embedding material is perfectly rigid. The results for this case show that, although several non-propagating and inhomogeneous modes are involved in the scattering process, only the lowest order non-propagating mode significantly influences the reflection coefficient.

The nature of the reflection coefficient when the embedding material is an epoxy resin has been discussed in detail. It has been shown that the reflection coefficient is a function of the frequency-radius product, as are the dispersion relationships. It was found that, in the frequency range which was covered by the analysis, the reflection coefficient depends only minimally on the longitudinal velocity of the resin, but is a strong function of the shear velocity. As in the case where the embedding material is rigid, the influence of the non-propagating and inhomogeneous modes was found to be minimal.

The numerical results from the modal solution and the Finite Element modelling were experimentally verified, very good agreement being obtained.

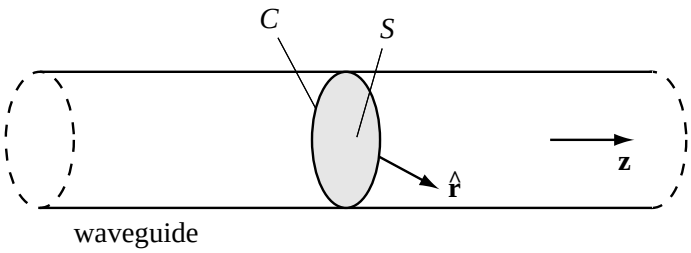

Figure 5.1: Circular waveguide of cross-section S and circumference C. $\hat{\mathbf{r}}$ is the outward normal vector to C.

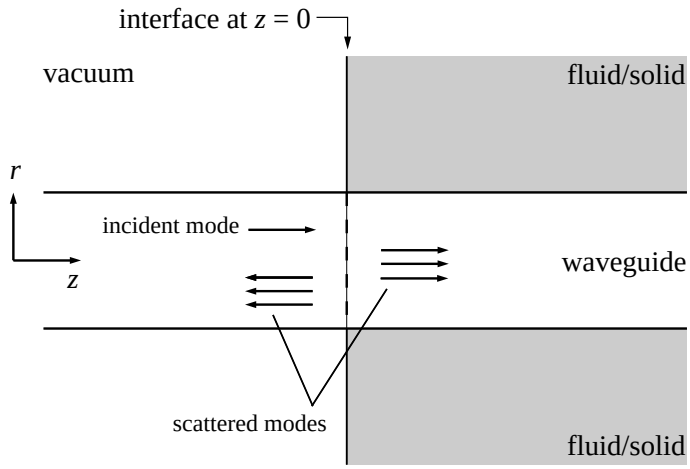

Figure 5.2: Schematic of the problem considered in this chapter. A propagating mode incident from the free section of the bar is scattered at the interface at $z = 0$ due a change in surface impedance.

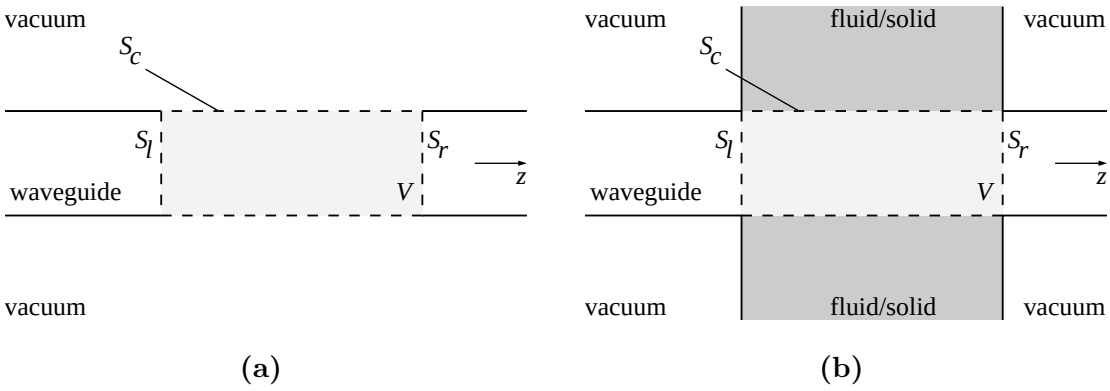

Figure 5.3: (a) Solution "1", without surface loading, and (b) solution "2", with surface loading.

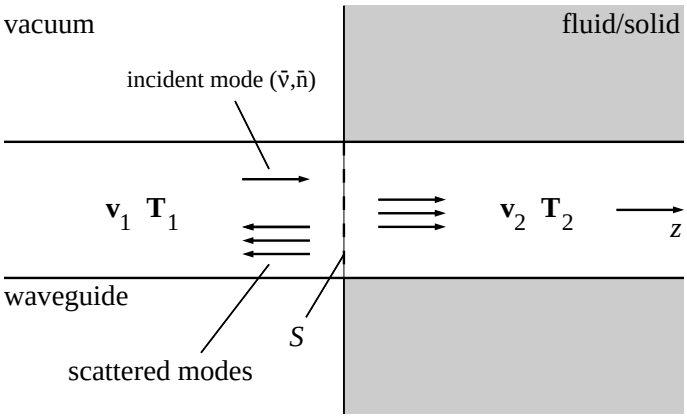

Figure 5.4: Partly embedded circular waveguide. An incident mode ($\bar{\nu}$,$\bar{n}$) is scattered at the interface between the free and embedded section of the waveguide. The fields $\mathbf{v}_1$ and $\mathbf{T}_1$ in the free section are represented by a superposition of the incident and reflected waveguide modes. The fields excited in the embedded section are denoted by $\mathbf{v}_2$ and $\mathbf{T}_2$.

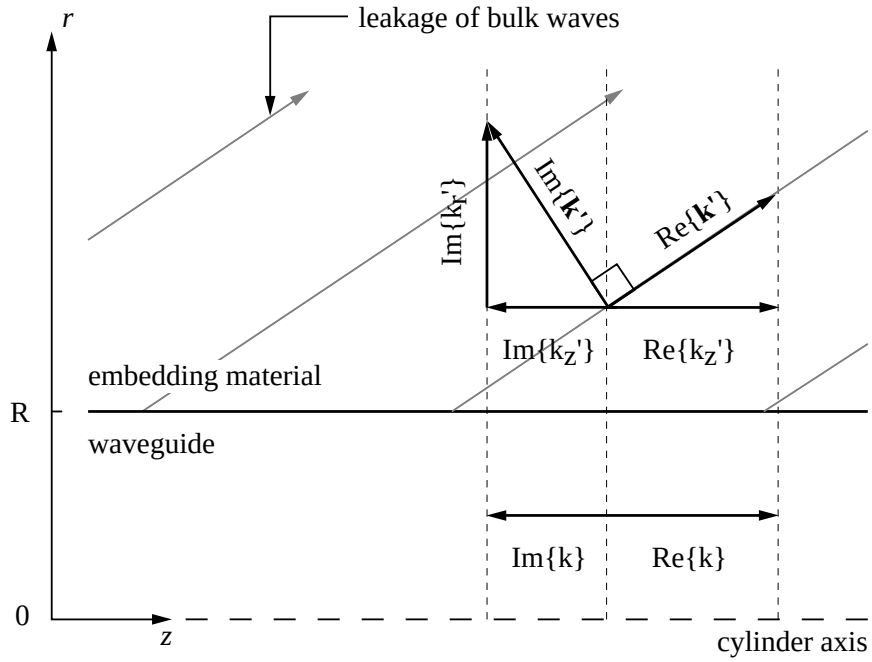

Figure 5.5: Schematic showing the geometrical relationship between the complex wavenumber of the guided wave in the axial direction, k, and the complex wavenumber vector of the leaky inhomogeneous bulk wave, $\mathbf{k}'$. Note that, for harmonic propagation with e^{-ikz}, $\mathrm{Im}\{k\} < 0$ corresponds to a guided wave which is attenuated in the positive z-direction.

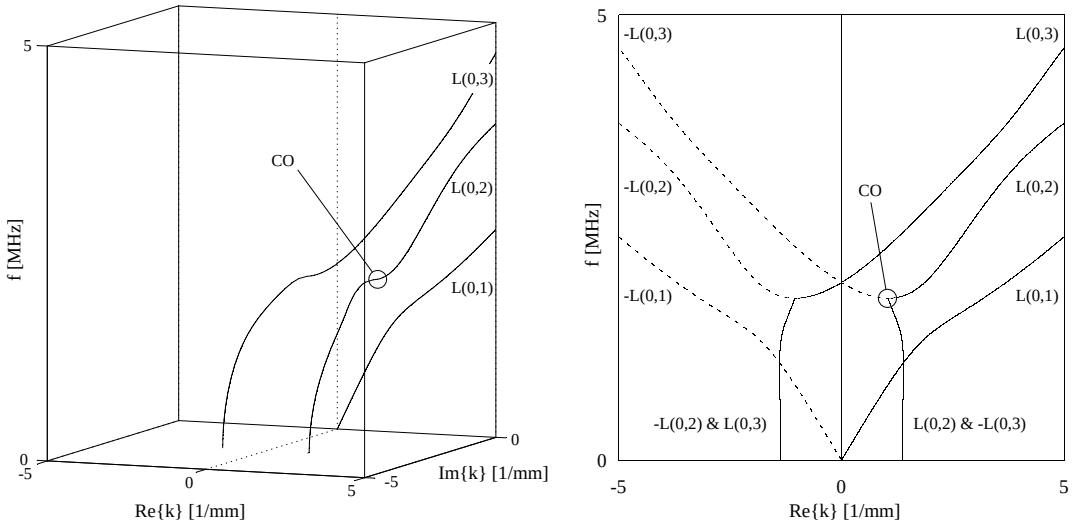

(a) **(b)**

Figure 5.6: (a) 3-dimensional dispersion curves for the first three longitudinal forward modes in a 1 mm steel cylinder in vacuum. (b) Real wavenumber of the first three longitudinal modes, showing forward and backward modes plotted in solid lines and dashed lines, respectively. CO indicates the cut-off point below which L(0,2) is inhomogeneous.

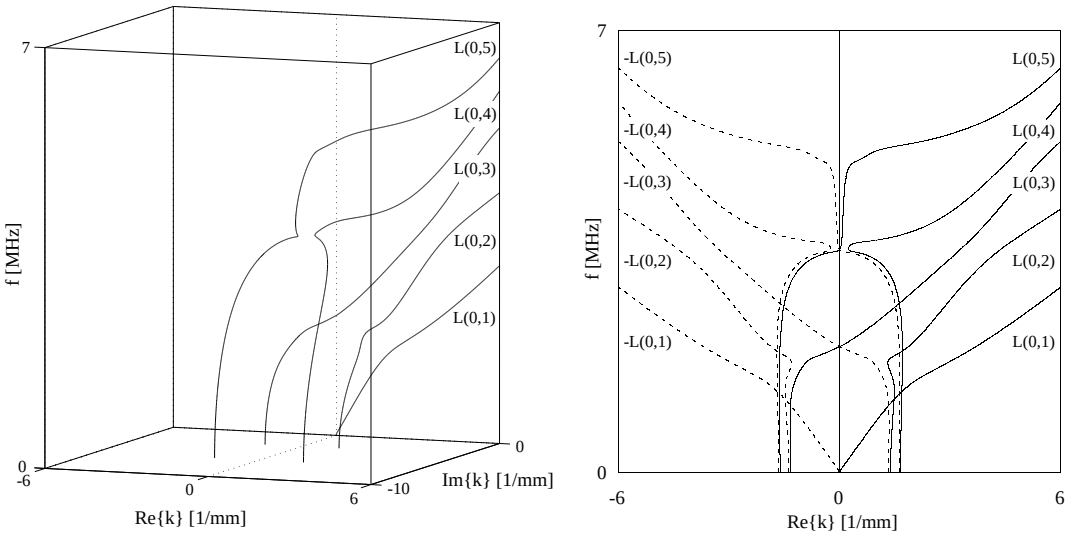

(a) **(b)**

Figure 5.7: (a) 3-dimensional dispersion curves for the first five longitudinal forward modes in a 1 mm steel cylinder embedded in epoxy resin. (b) Real wavenumber of the first five longitudinal modes, showing forward but also backward modes in solid lines and dashed lines, respectively.

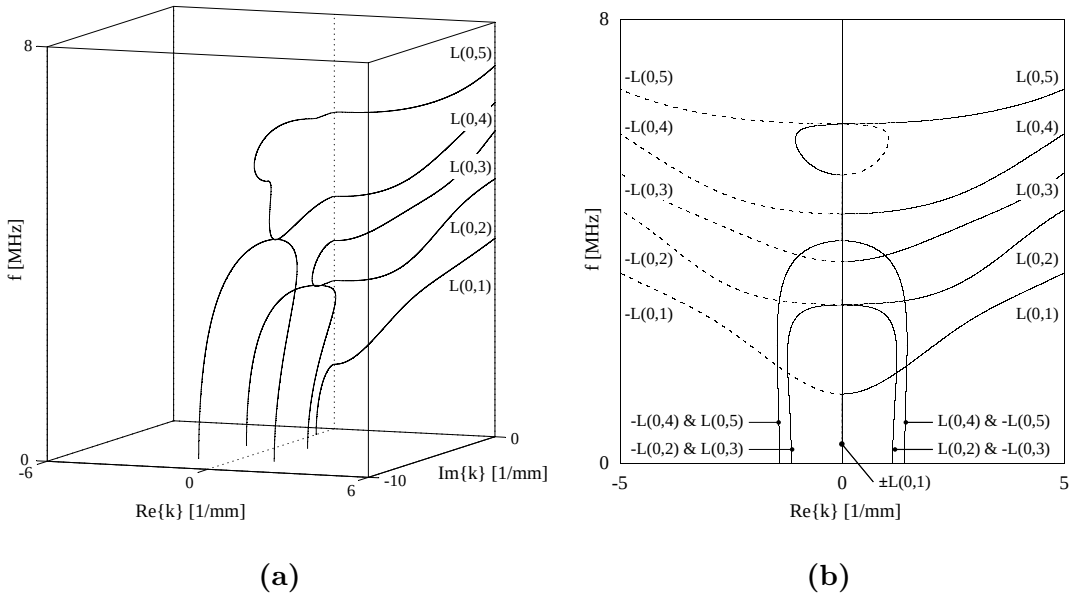

Figure 5.8: (a) 3-dimensional dispersion curves for the first five longitudinal forward modes in a 1 mm steel cylinder with rigid boundaries. (b) Real wavenumber of the first five longitudinal modes, showing forward but also backward modes in solid lines and dashed lines, respectively. Note that there are no propagating modes at low frequencies.

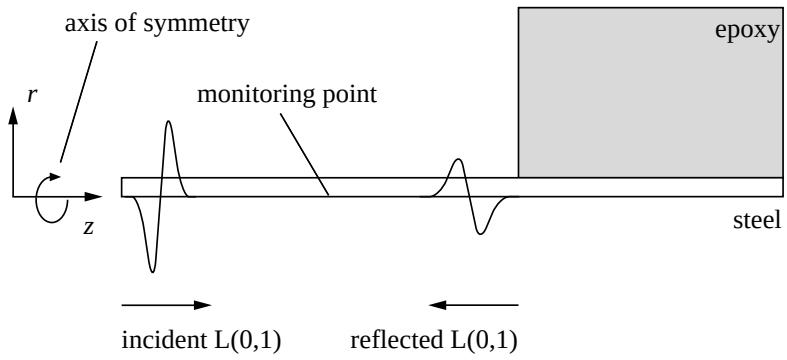

Figure 5.9: Schematic of the Finite Element model for a cylinder entering an epoxy resin.

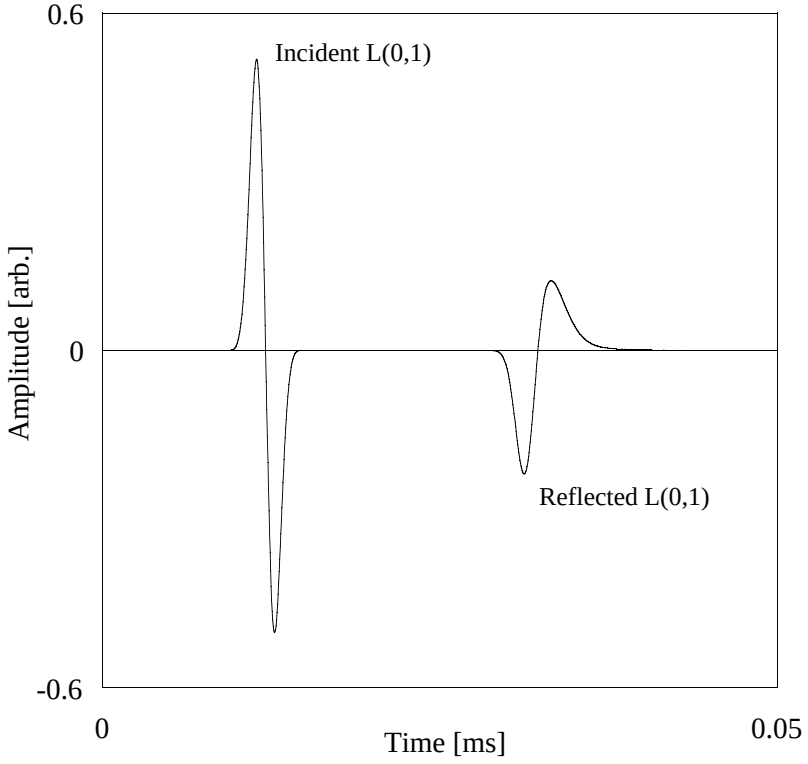

Figure 5.10: Typical Finite Element time trace of the incident and reflected L(0,1) mode in 0.5 mm diameter steel bar which is partly embedded in epoxy.

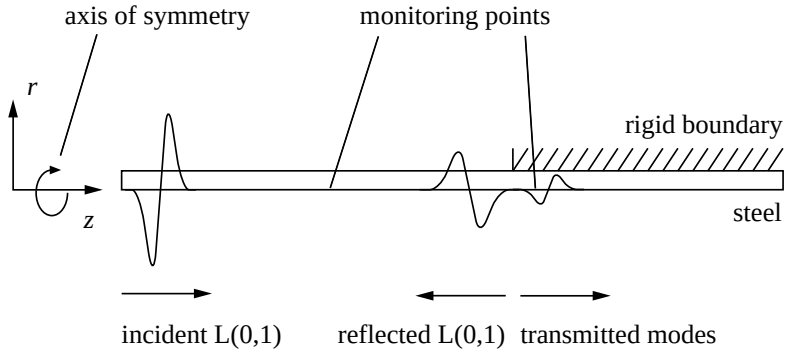

Figure 5.11: Schematic of the Finite Element model for a cylinder entering a region with rigid boundaries.

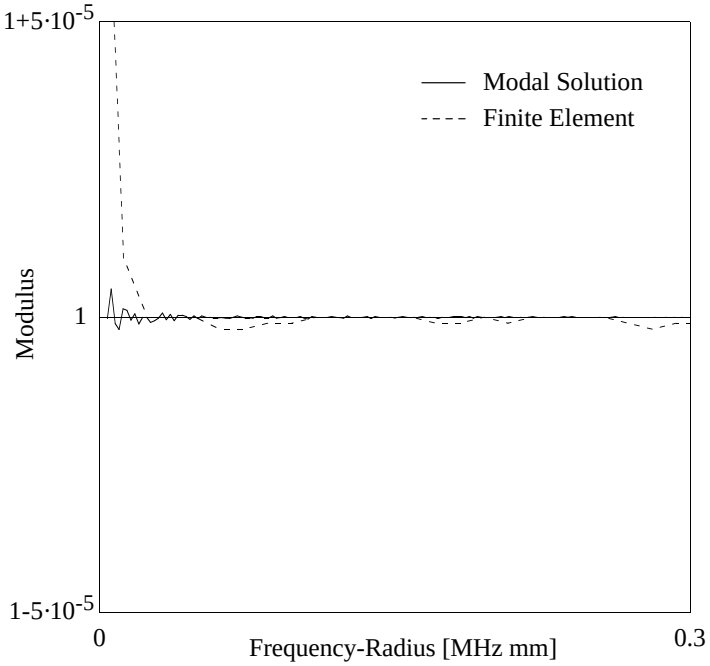

Figure 5.12: Modulus of the reflection coefficient of L(0,1) from the interface between a cylinder with a free and one with a rigid surface. As explained in the text, this should be exactly unity. Note that the ordinate has been scaled to better show the error in the calculations.

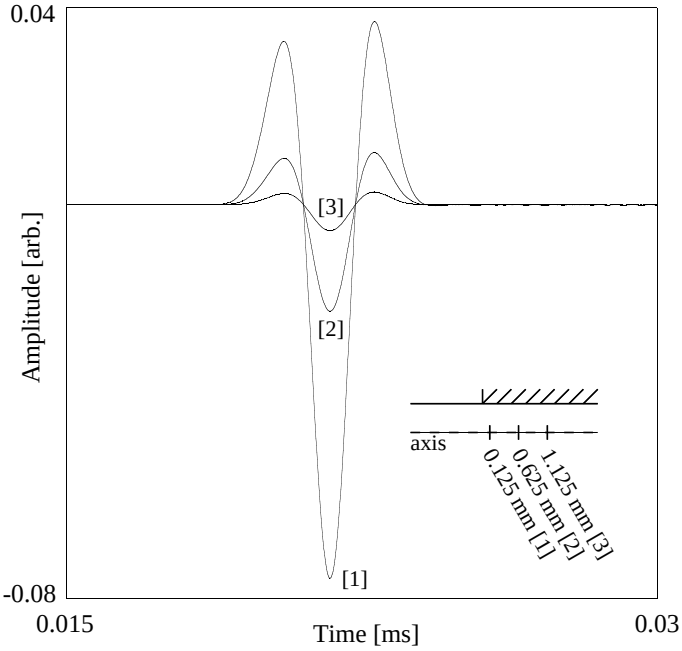

Figure 5.13: Time trace showing the displacements in the rigid section of the cylinder at three locations, 0.125 mm, 0.625 mm, and 1.125 mm away from the interface.

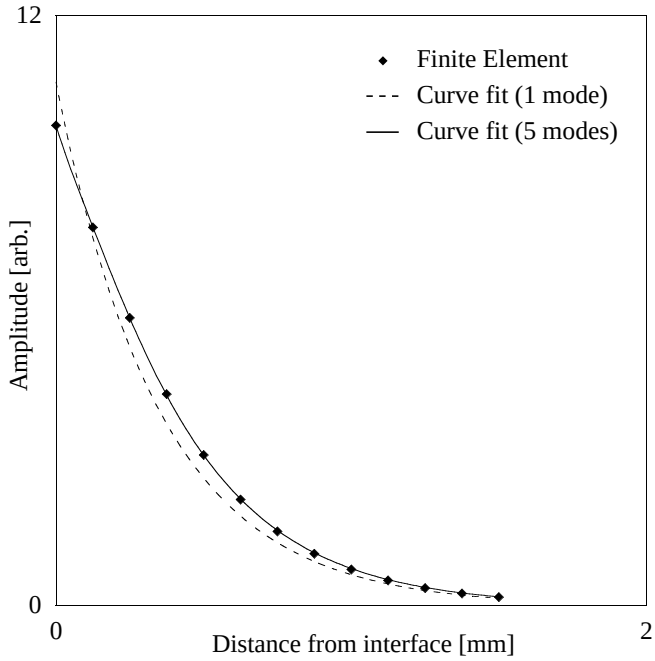

Figure 5.14: Modulus of the displacement at 0.2 MHz versus distance from the interface. Details regarding the curve fits are given in the text.

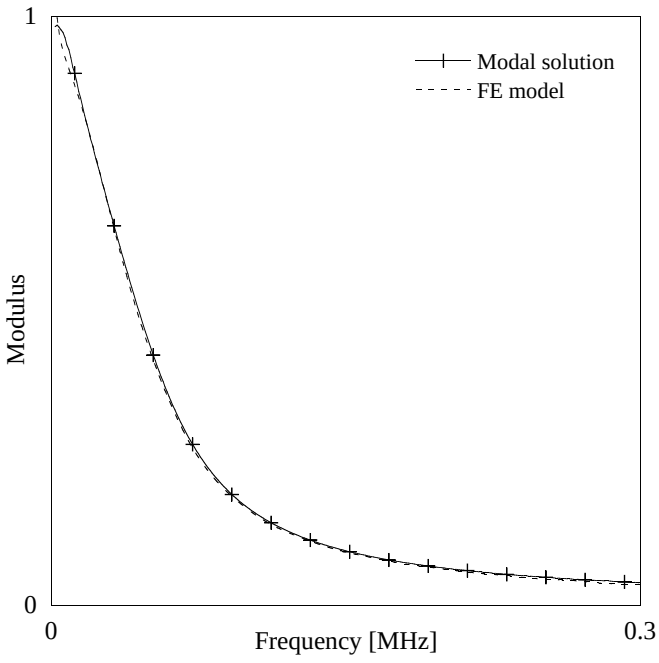

Figure 5.15: Modulus of the amplitude reflection coefficient of L(0,1) in a 1 mm radius steel bar embedded in epoxy. The material parameters for this analysis are given in Tab. 5.1. The plot shows the results obtained with the modal solution, using only the lowest order longitudinal mode in the analysis, and the Finite Element (FE) model.

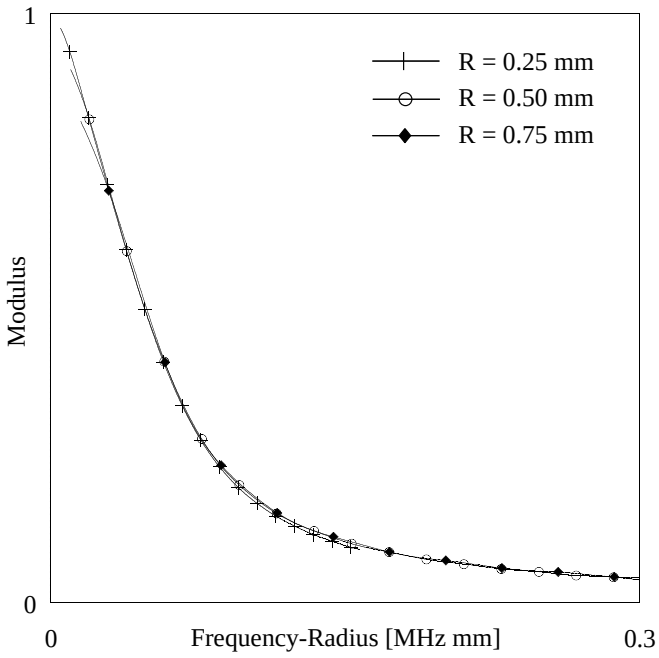

Figure 5.16: Modulus of the amplitude reflection coefficient of L(0,1) in a steel bar embedded in epoxy as a function of the product of frequency and radius. The material parameters for the analysis are given in Tab. 5.1. The plot shows the Finite Element results obtained with three different wire radii R.

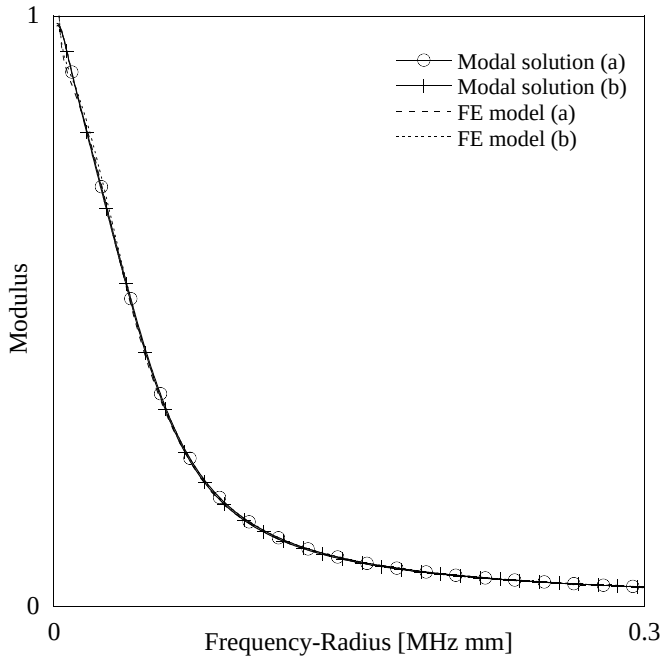

Figure 5.17: Dependence of the modulus of the reflection coefficient on the longitudinal velocity for two different materials, "a" and "b", respectively. The material properties used in the analysis are given in Tab. 5.1.

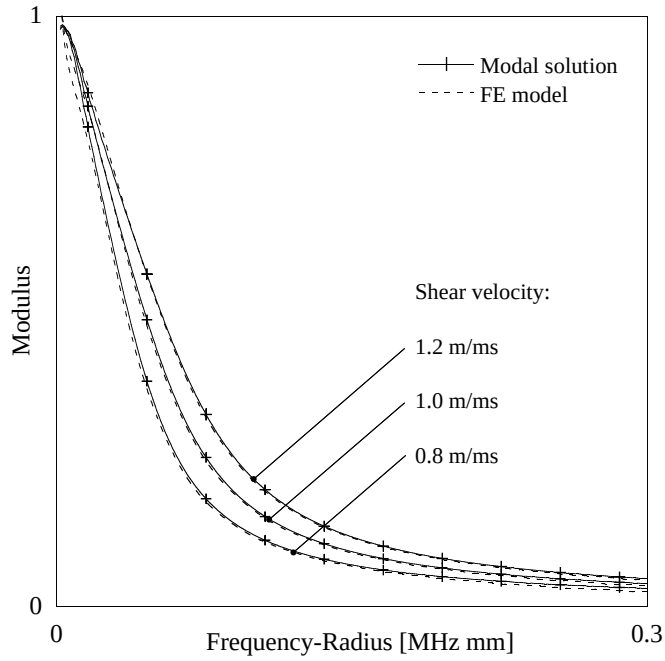

Figure 5.18: Modulus of the amplitude reflection coefficient of L(0,1) in a steel bar for different values of epoxy shear velocity. All other material properties of the epoxy are according to Tab. 5.1.

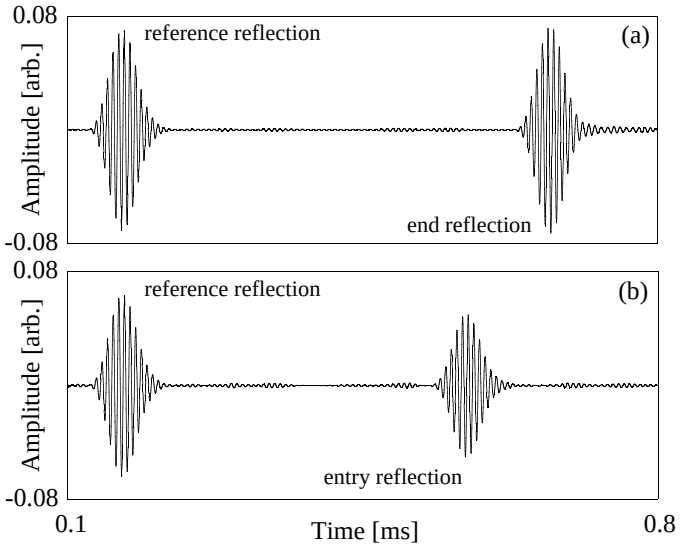

Figure 5.19: Experimental time traces of the lowest order longitudinal mode, L(0,1), in a 0.125 mm radius steel wire. Plots (a) and (b) show the time trace before and after embedding in epoxy resin, respectively. In plot (b) the resin has fully cured.

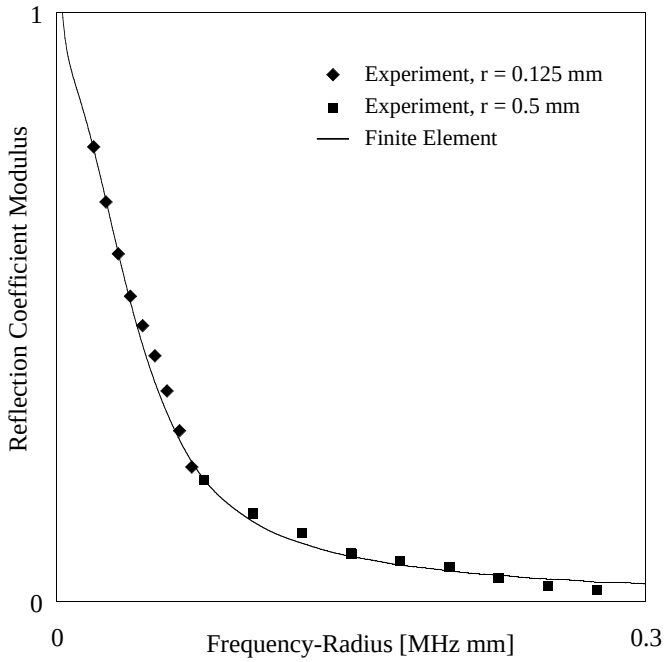

Figure 5.20: Measured and predicted entry reflection coefficient for steel wires partly embedded in an epoxy resin. Experiments were conducted with two wires of different radius, $r = 0.125\,\text{mm}$ and $r = 0.5\,\text{mm}$. The solid line shows the Finite Element results.

Chapter 6

Application to Cure Monitoring

6.1 Background

This chapter is concerned with the monitoring of the cure process of epoxy resins. The emphasis here is to demonstrate the measurement techniques presented in Ch. 4 and Ch. 5 rather than the examination of the properties of specific epoxy resins.

An epoxy is a molecule containing one or more epoxide groups (see, for example, [81]). The curing process is a chemical reaction in which these epoxide groups in the resin react with a curing agent to form a cross-linked polymer. The curing agent is also known as hardener. Commercial epoxy resins are thus delivered in two parts, one component being the epoxy resin, the other one being the hardener. Before the epoxy resin and the hardener are mixed to initiate the curing reaction, both components have the consistence of a viscous liquid or a paste, depending on the particular resin and agent. Once mixed, due to the cross-linking of polymer chains, the material properties of the resin change. In general, both the shear and the longitudinal bulk velocity increase monotonically with the progress of cure until the final values are reached and the resin is fully cured. The resin is then a solid material. The longitudinal bulk attenuation initially increases, reaches a maximum and decreases monotonically until the end of cure, whereas the shear bulk attenuation decreases monotonically throughout the cure process [3, 82]. However, it should be noted that existing ultrasonic techniques cannot easily monitor the shear properties in the initial stages of cure. In some resins, the temperature in the

sample may rise due to exothermic reactions, and cause the viscosity to decrease in the initial stages of cure. Also the density can change during cure as shrinkage is observed to different extents in some resins. However, for the resins used in this thesis, a density change could not be observed.

Several researchers have previously investigated the possibility of using a waveguide technique for monitoring this cure process. In 1974 Papadakis presented two methods for determining the change in material properties of an epoxy resin over the cure cycle [63], which are indeed the measurement techniques presented in Ch. 4 and Ch. 5. The first method is based on the measurement of the attenuation of longitudinal and torsional guided waves in a circular bar. The second method measures the reflection of those waves from the point where the waveguide enters the resin. Both attenuation and reflection change significantly during cure.

The feasibility of using guided waves in wires for monitoring cure as well as the structural integrity of composites was also investigated by Harrold and Sanjana [2]. Their measurements were based on the attenuation method. They excited guided waves in a 1.5 mm diameter polyester-fibreglass rod at 74 kHz, and the attenuation of the guided wave when embedded in a curing epoxy resin and a curing gel was measured in through transmission. The effect of bubbles occurring in the epoxy could be observed as a small peak in the amplitude. However, they did not account for the entry reflection. The theoretical foundations and practical aspects of cure monitoring with waveguides were qualitatively described by the same authors in Ref. [83]. Harrold *et al.* later also applied this technique to monitor the solidification process of other materials such as concrete [84].

Li *et. al.* used the wire waveguide technique in a through-transmission arrangement, with the transmitter at one end of the wire and the receiver at the other end [85]. Where it is embedded in the epoxy, the wire is bent in the form of a U-turn, so that two sections of the wire run parallel to each other (see Fig. 6.1). When the epoxy cures, the guided wave will go all along path 1 and be received at the other end, thereby being more and more attenuated during cure. At one point, the guided wave

attenuation will become too high, but energy is then propagated between the two legs of the wire (path 2). Characteristic curing curves of amplitude and time of flight can be obtained this way. It should be noted that the mechanism for the propagation of waves between the legs of the wire is closely related to the study carried out in Ch. 7, where the effect of radiating waves in a joint geometry is analysed.

However, all these results are so far only of a qualitative nature and have not been related to the actual material properties of the epoxy resin. This is due to the fact that the underlying theory had not been worked out in detail. The measurement techniques and modelling tools for measuring material properties presented in Ch. 4 and Ch. 5 are suited for this task and are used in the following.

In the early stages of this investigation, only the longitudinal mode, L(0,1), was used because it is easy to excite using piezoelectric excitation. Because of this chronological circumstance, work has concentrated on the longitudinal mode. As for the reflection coefficient method presented in Ch. 5 and the analysis carried out in Ch. 7, the analysis in this chapter covers only this mode. However, the modelling tools and measurement techniques are completely general and can be applied to any other mode, such as for example the torsional mode, T(0,1).

In the following, a brief review of existing cure monitoring techniques other than ultrasonic waveguide techniques will be given. Preliminary considerations then deal with the applicability of the reflection and the attenuation method for measuring the properties of curing and solid materials. The reflection and the attenuation method are then applied to the cure monitoring of an adhesive that can be cured in bulk form in order to avoid geometry effects which will be described in Ch. 7.

6.2 Review of Existing Cure Monitoring Techniques

The following review is intended to give a short overview into the existing techniques other than guided wave methods which have been described in Sec. 6.1. In order

to remain within the scope of this work, the non-ultrasonic techniques in particular are described only briefly, and the reader will be referred to the cited literature.

Ultrasonic Bulk Wave Techniques

Ultrasonic cure monitoring of epoxy resins was first investigated by Sofer and Hauser in 1952 [86]. They measured the longitudinal velocity and attenuation of a resin contained in a test chamber in through transmission at 2.2 – 2.4 MHz. While the longitudinal bulk wave velocity increased monotonically, they observed that the attenuation increases at first, then goes through a maximum, and then decreases again. Temperature changes were recorded, too, but they concluded that the maximum in attenuation occurs independently.

Speake *et al.* [87] used both an ultrasonic critical-angle and an ultrasonic resonance method to monitor the cross-linking reaction in epoxy resins. The objective of their work was to measure cure after the gelation point, where the polymer is already relatively solid. The critical-angle technique is based on the principle of critical reflection of a wave at an interface between two media. The angles of reflection and refraction of longitudinal and shear waves at an interface between two media are related to each other by Snell's law. At a certain critical angle, depending on the material properties of the two media, total reflection occurs, and a peak in the reflected amplitude can be observed, because the energy of the incident wave is no longer split into a reflected and a refracted one. Thus, the measurement of the critical angles for shear and longitudinal waves yields the sound velocities of the material under investigation. They found that this technique is sensitive to changes both in the shear and the longitudinal velocity of curing epoxy resins. In the resonance technique, longitudinal or torsional waves were transmitted along a rod which was mechanically coupled to the specimen in a frequency range of 10 – 100 kHz. Resonances which show up in the amplitude spectrum of the reflected signal allow Young's modulus and the shear modulus to be obtained, using an apparatus originally developed by Bell [88].

Lindrose [89] measured and calculated both the longitudinal and the shear modulus

of a resin as a function of cure time by applying a pulse-echo technique. He used longitudinal and shear wave transducers at a frequency of 1 MHz. Freemantle *et al.* [3] presented a through-transmission set-up where the test cell, which contains the resin sample, is immersed in water. A longitudinal wave is transmitted through the water and the resin sample. Using a goniometer, the test cell could then be angled with respect to the direction of propagation of the longitudinal wave in the water. This way, longitudinal and, through mode conversion, also shear waves were excited in the resin sample. Once these waves reach the other side of the sample, they excite a longitudinal wave in the water and are detected by a receiving transducer. Both longitudinal and shear phase velocity and attenuation can be calculated.

Rohklin *et al.* [90] measured the frequency dependence of phase velocity and attenuation during polymerisation in the range of 2 – 20 MHz. They concluded from their measurements that the attenuation increases linearly with frequency at all stages of the cure process. The frequency dependence of the longitudinal properties of thin viscoelastic adhesive layers as a function of cure was also measured by Challis *et al.* [91] by applying a short pulse technique in through transmission. The elastic modulus can be calculated on the basis of a frequency domain comparison of shapes of successive reverberations in the adhesive layer.

Dixon *et al.* [82] measured the cure process of an epoxy resin using electro-magnetic acoustic shear transducers. The adhesive was contained in a test cell with parallel aluminium sheets, and the transducers were placed on opposite sides of the cell. The shear properties of the adhesive were measured both in through transmission and by measuring the reflection which occurs at the interface between the aluminium plate and the adhesive. It was found that the shear velocity increases during cure whereas the shear attenuation decreases monotonically.

Measurements of cure were also carried out in composite materials [92, 93] and epoxy resins containing fillers such as glass beads and fibres [87].

Dielectric Analysis

A well established means of monitoring the cure process of epoxy resins is dielectric analysis [94, 95, 96, 97, 98]. The method is based on the measurement of electrical capacitance, which is related to the complex dielectric constant. The resin is placed in an alternating electric field between two metal electrodes. In the early stages of cure up to the gelation point the ionic conductance dominates the dielectric response. It depends on the mobility and concentration of the ions, and is therefore also closely related to the viscosity. If the viscosity is low, then the dissipation term of the dielectric constant is small, because the motion of the dipoles is not impeded. This is different during gelation, where the viscosity is very high. There, the dissipation is at its maximum. After that point, a polymeric network is formed, so that the dipoles are fixed in their position and hence cannot dissipate energy by moving in the alternating electric field. Therefore, the dissipation curve decreases until the end of cure. The real part of the dielectric constant is a measure of the ability of the molecules to align themselves in the presence of an electric field, and undergoes significant changes during the cure process, too. After gelation, like the dissipation factor, it decreases monotonically.

NMR Analysis

The nuclear magnetic resonance technique reveals information regarding the internal structure of a material. This method is able to distinguish the different stages of cure by measuring relaxation times of nuclear spins. The relaxation time is related to the mobility of the molecules, and is the shorter the more solid the material is. If both a liquid phase and a solid phase co-exist in the material, two different signals with different relaxation constants appear. Therefore, by tracking the relaxation times over the cure cycle, the change from a viscous liquid to a cross-linked solid polymer can be observed. Studies on an epoxy resin during cure were recently carried out by Dare and Chadwick [99].

Infrared and Optical Analysis

There are a number of different infrared spectroscopy methods, which are all useful for monitoring polymerisation rates and the chemical mechanisms of cure. They are

based on the observation of absorption bands belonging to a group of reactants in the infrared spectrum. A thorough review is given in Ref. [81]. Similar to ultrasonic guided wave methods, optical fibres can be used for the infrared spectroscopy methods [100].

X-Ray Analysis

Wide-angle X-ray scattering has recently been applied to measure the formation of chains and networks in curing resins [101]. The development of peaks in the intensity at different scattering angles indicate the development of local structures and molecular components. So far, the conclusions that can be drawn from this technique are not very specific.

6.3 Applicability of the Reflection and Attenuation Method

6.3.1 General Applicability

The nature of the entry reflection coefficient of the fundamental longitudinal mode determines the range of frequency-radius products at which each method is applicable. Clearly, the reflection coefficient method can only be used at low frequency-radius products, since only there is it of significant magnitude. For the attenuation measurements, it would be preferable also to work at low-frequency radius products, since the influence of the longitudinal properties of the adhesive can be neglected there, which makes it possible to relate the attenuation measurement to the shear properties of the epoxy resin. Also, the longitudinal mode becomes dispersive at higher frequencies which makes testing more difficult. However, in practice, where the exciting transducer is placed on a free section of the waveguide, and the guided wave of the free bar has to be transmitted into the guided wave in the embedded section, the need to minimise entry reflection forces one to work at higher frequency-radius products. Only there is enough energy transmitted into the embedded part, and the entry reflection may be neglected or included in the analysis as an error. The shaded regions in Fig. 6.2 schematically indicate where each method is appli-

cable. Of course, the limits of these regions are not strict, and they depend on the system under investigation and the accuracy required.

6.3.2 Application in Automotive Joints

Regarding the cure monitoring application in thin joints in an industrial setting, the reflection coefficient methods seems at first better suited for an industrial application mainly from a practical point of view. Firstly, for the attenuation method, it is difficult to exactly determine the embedded length of the wire in real joints. This uncertainty affects the calculation of the attenuation according to Eq. (4.9). There is no such limitation for the reflection coefficient method. Secondly, for the application in thin joints, also thin wires have to be used. Keeping in mind that for small radius wires the entry reflection becomes large, the attenuation method does not seem feasible. One solution would be to test at higher frequencies. However, the intrinsic attenuation in the wire itself increases with increasing frequency, which is a disadvantage when using long wires as is anticipated for this particular application.

For the reasons outlined above, the investigation into possible effects of the joint geometry as presented in Ch. 7 will concentrate on the reflection method.

6.4 Reflection Method for Cure Monitoring of Bulk Samples

6.4.1 Numerical Simulations

For a cure monitoring experiment it is important to know how the reflection coefficient changes with the increasing shear velocity of the embedding resin. Figure 5.18 shows the entry reflection of L(0,1) for different epoxy shear velocities. Apart from the shear velocity, which is indicated in the plot for each reflection coefficient curve, the epoxy properties are the same as the ones given in Tab. 6.1 for the solid epoxy. While the epoxy resin solidifies, the shear velocity increases and the change in surface impedance becomes larger, so that the entry reflection increases. As an example, Fig. 6.3 shows the reflection coefficient as a function of the epoxy shear velocity at a

frequency-radius product of 0.05 MHz mm. This shows once more the advantage of the modal solution over Finite Element modelling, since for this result a number of different FE calculations would have to be performed, apart from the fact that it is not feasible at low shear velocities for the reasons pointed out in Sec. 5.1. The modal solution, in contrast, only needs one calculation, since the mode shapes, which are needed for the modal solution, can be traced in DISPERSE as a function of the shear velocity, with fixed frequency. Of course, the longitudinal bulk velocity also undergoes significant changes during cure, but as was already mentioned in Sec. 5.6.2, this does not affect the reflection coefficient.

Table 6.1: Material parameters used for the analysis in Ch. 6.

Material	c_l [m/s]	c_s [m/s]	ρ [kg/m^3]
Steel	5960	3260	7930
Solid Epoxy	2610	1000	1170
Liquid Epoxy	1700	–	1170

The modelling tools presented enable the optimisation of the guided wave system, by choice of the frequency-radius product, to have the highest sensitivity to shear changes. The sensitivity S, which is the change in reflection coefficient R for a given change in shear velocity c_s at a particular shear velocity c_0 is determined by the following expression:

$$S = \left.\frac{\mathrm{d}R}{\mathrm{d}c_s}\right|_{c_0} . \tag{6.1}$$

Figure 6.4 shows the sensitivity around a shear velocity of $c_0 = 1\,\mathrm{m/ms}$. For a typical epoxy resin surrounding a steel wire, a maximum occurs at around 0.05 MHz mm. The reflection coefficient experiments were therefore conducted in this frequency-radius range.

As was explained in Sec. 6.1, the shear bulk attenuation decreases with the progress of cure, whereas the shear bulk velocity increases. For typical values of bulk shear

velocity and attenuation in the epoxy after the completion of cure (see, for example, Ref. [3]), results using the modal solution suggest that even a high attenuation value of 0.5 np/wl in the epoxy influences the reflection coefficient only minimally (see Fig. 6.5). For this analysis, the frequency dependence of the bulk shear attenuation of the resin was assumed to be such that the attenuation per wavelength was constant. This behaviour is supported by findings of Freemantle *et al.* [3] in ultrasonic bulk wave experiments.

It should be noted that the modelling examples given here are idealised in that the epoxy resin was modelled as an elastic material. As mentioned before, in reality it behaves more like a viscoelastic material with a changing bulk shear velocity and attenuation. Since only one variable can be determined either from the reflection coefficient or from the attenuation technique, it is not possible to characterise the embedding material completely. However, it has been shown that in the later stages of cure, the bulk shear attenuation has a negligible effect, so the bulk shear velocity can be predicted accurately. In the earlier stages of cure, the bulk shear attenuation is very high and will affect the calculation of the shear velocity. Therefore, an accurate value of shear velocity cannot be obtained. Nevertheless, the measurement is indicative of the progress of cure in the early stages.

6.4.2 Experimental Findings

The commercial epoxy adhesive Araldite 2013 (Ciba Specialty Chemicals) was used in the experiments. It is a low temperature curing adhesive for metal bonding and gap filling applications. Cure monitoring experiments were conducted using a 0.5 mm radius steel wire as the measurement wire. The longitudinal mode L(0,1) was excited in the wire using magnetostrictive transduction. A wide-band, 2 cycle Hanning windowed signal was chosen so that the reflection coefficient could be evaluated at several frequencies. The epoxy was cured at room-temperature in a bulk sample of 50 ml volume in a polyethylene beaker of 53 mm inner diameter, and the measurement wire was fed through holes in the beaker. After taking a reference time trace before embedding, the adhesive was poured into the beaker and measurements were taken at intervals of 5 minutes. The beaker was positioned approximately in

the middle of the measurement wire.

Figure 6.6 shows example time traces obtained during cure. The time trace at 0 hours shows the reference time trace before embedding. The signal denoted by "A" is the reference reflection from the joint between the magnetostrictive and the measurement wire, and the reflection denoted by "B" is the reflection from the end of the wire. The remaining time traces show the reflections while the measurement wire is embedded in the curing epoxy. After 1 hour, the entry reflection, "C", can be seen, and the amplitude of the end reflection decreases due to both increasing attenuation in the embedded part and also due to the fact that some of the energy is reflected at the entry point. After 2 hours, the end reflection disappears completely, and only the entry reflection remains visible. The entry reflection increases monotonically with curing time due to the increasing shear velocity in the epoxy. A second reflection, "D", can be observed after approximately 3 hours. This is not a reflection from the end of the wire but a reverberation of the entry reflection "C" between the entry point and the joint between the magnetostrictive and the measurement wire. No significant further changes are observed after approximately 8 hours.

The cure monitoring curves obtained from the above experiment at different frequencies are plotted in Fig. 6.7, using equation (5.74). As expected, the reflection coefficient is higher at lower frequencies. The reflection coefficient of L(0,1) at the end of cure at 0.05 MHz mm was $R = 0.451$. With a density of $\rho = 1170\,\mathrm{kg/m^3}$, this corresponds to an epoxy shear velocity of $c_s = 1.06\,\mathrm{m/ms}$. This agrees well with the shear velocity data given in Ref. [3].

Note that in this case cure is measured at the edge rather than in the interior of the epoxy sample. This is important to keep in mind as considerable temperature differences may occur between the inside and the surface of the curing adhesive, resulting in different curing rates.

6.5 Attenuation Method for Cure Monitoring of Bulk Samples

6.5.1 Numerical Simulations

It is clear from Sec. 6.3 that at higher frequency-radius products the guided wave incident from the free section of the wire is almost entirely transmitted into the embedded section. The analysis in this section deals with the guided wave which is transmitted as a mode in the embedded waveguide.

As mentioned before, the guided wave is attenuated due to the leakage of bulk waves into the surrounding medium. If the embedding material is an ideal liquid, only bulk longitudinal waves are radiated, whereas if it is a solid, both shear and longitudinal waves may be radiated and contribute to the leakage. In the case of the fundamental longitudinal mode, L(0,1), at low frequencies the leakage of longitudinal waves is small, since the surface displacements are mainly in the axial direction. Therefore, leakage is almost entirely due to shear leakage. It is hence expected that the attenuation is low at the onset of cure and increases with increasing shear velocity of the embedding epoxy resin.

As an example, Fig. 6.8 shows the attenuation dispersion curves of L(0,1) for a steel wire embedded in a liquid epoxy resin, modelled as an ideal liquid and representing the pre-cure state, and a solid epoxy resin, modelled as an elastic solid and representing the post-cure state. The density is assumed to stay constant throughout cure. As mentioned before, for an ideal liquid epoxy, only longitudinal bulk waves radiate, whereas for the solid epoxy, both shear and longitudinal waves contribute to the leakage. The dispersion curve for the liquid epoxy case confirms that at low frequency-radius products, the attenuation due to the leakage of longitudinal waves is small. Therefore, the attenuation is mainly sensitive to the shear properties of the epoxy resin. It should also be noted that the ordinate of Fig. 6.8 is a np·mm/m-scale. Therefore, the attenuation per metre of a 1 mm radius wire at a given frequency-radius product is double that of a 2 mm radius wire.

Figure 6.9 shows the effect of different epoxy longitudinal velocities on the L(0,1)-attenuation for a cured epoxy and an imaginary uncured one with a low shear velocity and the same longitudinal velocity. It is found that the longitudinal velocity has only little influence in the low frequency-radius limit below 0.5 MHz mm after the early stages of the cure cycle. Only at higher frequency-radius products does the longitudinal velocity have a significant effect on the attenuation, which is due to the increasing radial displacements at the surface of the waveguide. This is similar to the behaviour observed for the entry reflection.

The effect of shear bulk attenuation on the attenuation of the longitudinal guided wave at the end of cure is considered in Fig. 6.10. This shows the attenuation of L(0,1) for a purely elastic and a strongly attenuating epoxy resin. As before, for the evaluation of the influence of bulk shear attenuation on the reflection coefficient, the attenuation was taken to be constant per wavelength, thus linearly increasing with frequency. It can be seen that the difference in guided wave attenuation is very small, and may therefore also be neglected when calculating the shear properties of the epoxy resin after cure.

As an example, the L(0,1)-attenuation as a function of the epoxy shear velocity is given in Fig. 6.11, assuming that the epoxy resin is elastic. The attenuation increases almost linearly with increasing shear velocity. This is to be expected since by increasing the epoxy shear velocity, the difference between the acoustic impedance of the waveguide and the epoxy resin decreases.

6.5.2 Experimental Findings

The setup was changed slightly in order to make cure monitoring measurements using the attenuation method. As pointed out earlier, these measurements have to be taken at a higher frequency-radius product in order to avoid reflection at the entry point. Therefore, measurements were taken using a 1.5 mm radius steel wire at 0.266 MHz, which corresponds to a frequency-radius product of about 0.4 MHz mm. A piezoelectric transducer was used to excite L(0,1) in a 1 mm radius steel wire, and in order to avoid ringing a 10-cycle Hanning windowed input signal was applied.

The embedding length L for the calculation of the guided wave attenuation was 53 mm. The same adhesive was used as for the reflection coefficient experiments.

Figure 6.12 shows the development of the time traces during cure. The reference signal from the joint between the steel wires is denoted by "A", and the reflection from the end of the measurement wire is denoted by "B". The plot at 0 hours shows the reference time trace before embedding. After 1 hour, the amplitude of the end reflection has decreased due to the fact that the wire is embedded and leaking bulk waves into the epoxy. As the polymer chains are cross-linking, the shear velocity increases and the amplitude decreases monotonically until the end of cure as the L(0,1)-attenuation increases. After 2 hours, a small entry reflection occurs, "C", which increases until the end of cure. This entry reflection reaches a value of approximately $R = 0.05$ by the end of cure.

The attenuation as a function of the curing time is plotted in Fig. 6.13. In order to check consistency between the reflection coefficient and the attenuation results, the epoxy shear velocity is calculated at the end of cure. The attenuation of L(0,1) in the 1.5 mm radius steel wire at the end of cure was $\alpha = 18.89\,\mathrm{np/m}$, which corresponds to an attenuation-radius product of $\alpha \cdot r = 28.33\,\mathrm{np \cdot mm/m}$. Using these values, the epoxy shear velocity is calculated as $c_s = 1.01\,\mathrm{m/ms}$. This is within 4% of the value obtained with the reflection coefficient method and also agrees well with the shear velocity data given by Freemantle *et. al.* [3].

It should be noted that the entry reflection always introduces an error in the attenuation measurements if it is not accounted for in the analysis; the measured attenuation appears larger than the actual attenuation. The only way that this can be avoided is to fully embed the waveguide in the epoxy resin. If this is not possible, an estimate of the maximum error introduced by the entry reflection can be calculated from the entry reflection which was also measured during the cure experiment (reflection "C"). The transmission coefficient T may be calculated from the energy balance equation:

$$R^2 + T^2 = 1. \tag{6.2}$$

One main assumption enters this equation. It is assumed that all the incident power is scattered into the transmitted and reflected L(0,1)-modes, and not into other modes. As has been found in Ch. 5, the above equation is fulfilled to a high degree of accuracy.

In order to calculate the error introduced by the entry reflection, it is further assumed that the transmission coefficient from the free section into the embedded section is equal to the transmission coefficient from the embedded into the free section. It should be noted that this is not necessarily true, and the difficulty encountered when trying to calculate the latter transmission coefficient is outlined in Appendix B. In a pulse-echo experiment, as schematically shown in Fig. 3.6, the end of the wire waveguide protrudes from the epoxy sample in order to avoid losses through the end face of the wire. The received end reflection was therefore transmitted twice from the free into the embedded section and twice from the embedded into the free section, each time with a transmission coefficient of T. Thus, the normalised amplitude $A^{\mathrm{emb}}/A_0^{\mathrm{emb}}$ can be written in the following way:

$$\frac{A^{\mathrm{emb}}}{A_0^{\mathrm{emb}}} = \frac{A^{\mathrm{vac}}}{A_0^{\mathrm{vac}}}\, T^4 e^{-2\alpha L}. \tag{6.3}$$

It follows that the error ε introduced when calculating the attenuation according to equation (4.9) instead of equation (6.3) is

$$\varepsilon = \frac{2}{L} \ln T. \tag{6.4}$$

Note that this error becomes smaller with increasing embedding length L. Since T is always smaller than 1, $\varepsilon < 0$, and therefore the actual attenuation is overestimated. In this case, with $R = 0.05$, the error is estimated as $\varepsilon \approx -0.05\,\mathrm{np/m}$. This is small compared to the measured attenuation and may be neglected.

In contrast to the reflection coefficient method, the measured shear velocity for the attenuation method presents an average value measured over the embedded length of the waveguide.

6.6 Summary

The shear velocity of an epoxy resin changes significantly during cure. At the beginning of cure, the material properties range from viscous to pasty, depending on the epoxy resin. At this stage, conventional ultrasonic bulk wave techniques fail to monitor changes in the shear properties due to the high shear bulk attenuation. During solidification the shear velocity increases and the shear attenuation decreases steadily due to the cross-linking of polymer chains. These changes happen relatively quickly at the beginning of cure, whereas towards the end of cure, the curing rate is slowed down very much, even though the cure cycle is not complete.

It has been shown that it is possible to monitor the curing process of epoxy resins using the waveguide methods presented in Ch. 4 and Ch. 5. One significant advantage of the wire waveguide method is that the shear properties can be measured from the start over the whole curing cycle, and quantitative predictions of the shear velocity for example at the end of cure are possible. An indicative assessment of the progress of cure is possible at the early stages of cure, where conventional ultrasonic cure monitoring methods fail.

The nature of the entry reflection determines at which frequency-radius products the reflection and attenuation method can be applied. Experimental results have shown the validity of the predictions by modal analysis. These results are valid in bulk material of the embedding medium.

For the application in automotive joints, the reflection method is more attractive than the attenuation method. This is mainly due to the fact that thin wires have to be used, in which case the reflection method is better suited, but also due to calibration difficulties when using the attenuation method.

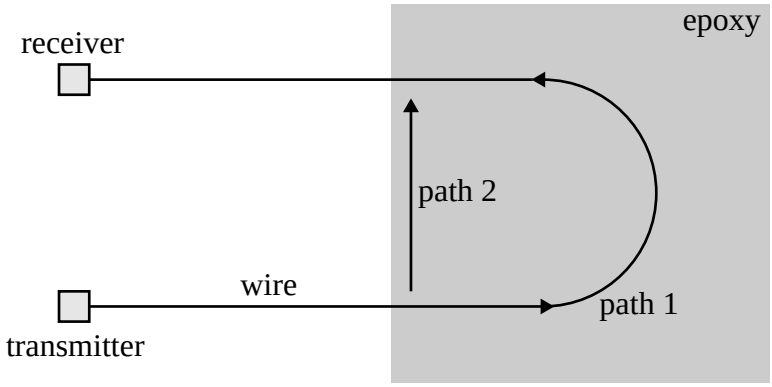

Figure 6.1: Experimental setup used by Li *et al.* to monitor epoxy cure.

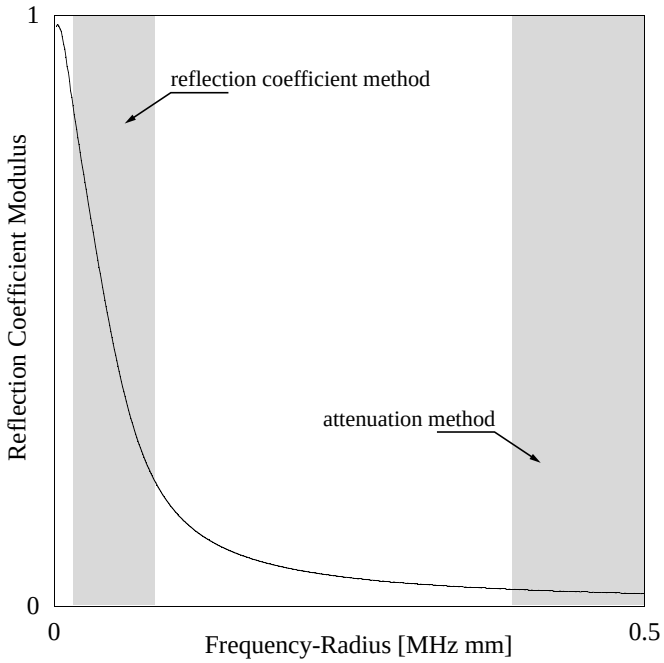

Figure 6.2: Entry reflection coefficient of L(0,1) as plotted in Fig. 5.15. The shaded areas indicate schematically where the reflection and attenuation method are applicable for cure monitoring experiments.

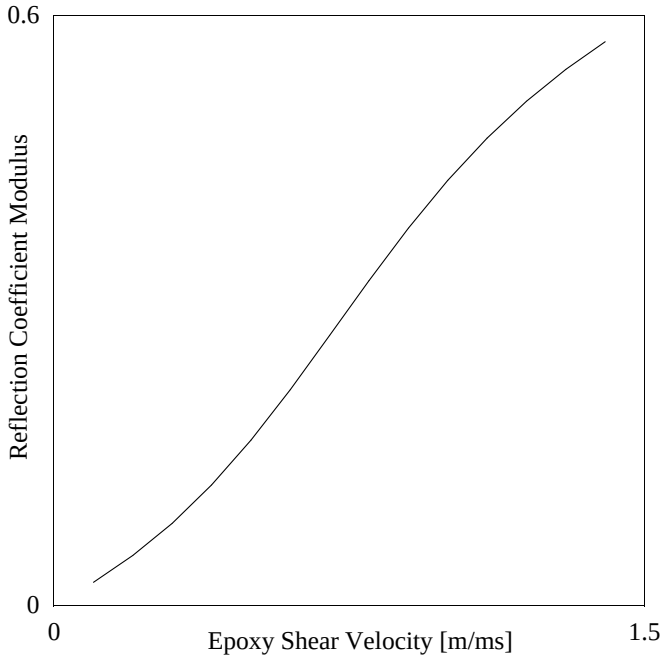

Figure 6.3: Predicted entry reflection coefficient of L(0,1) as a function of the epoxy shear velocity at a frequency-radius product of 0.05 MHz mm (modal solution). All other material properties are as for solid epoxy in Tab. 6.1.

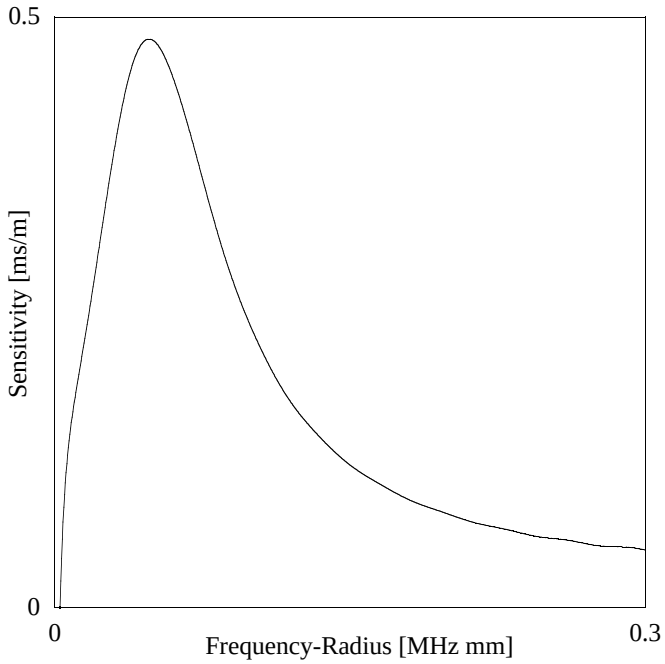

Figure 6.4: Sensitivity of the L(0,1)-reflection coefficient to changes in the shear velocity at $c_s = 1.0\,\mathrm{m/ms}$. A maximum occurs at around 0.05 MHz mm.

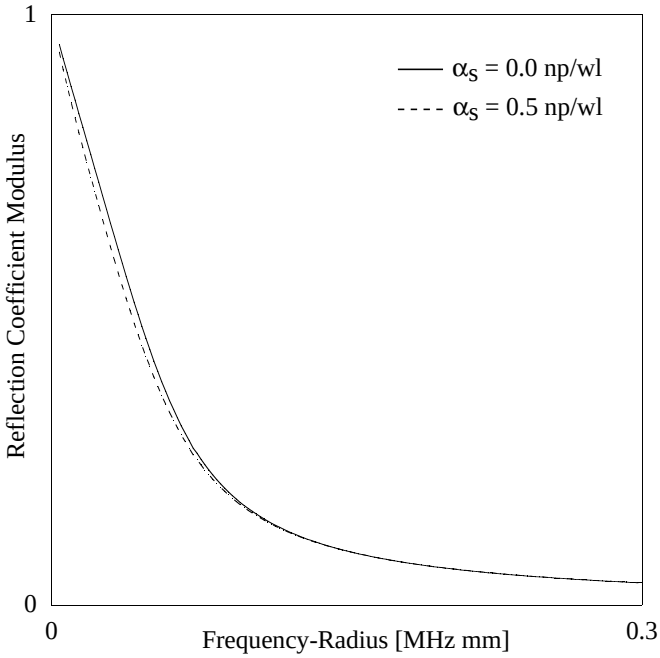

Figure 6.5: Predicted entry reflection coefficient of L(0,1) for different bulk shear attenuation values of the embedding epoxy resin (modal solution). All other material properties are according to Tab. 6.1 for solid epoxy.

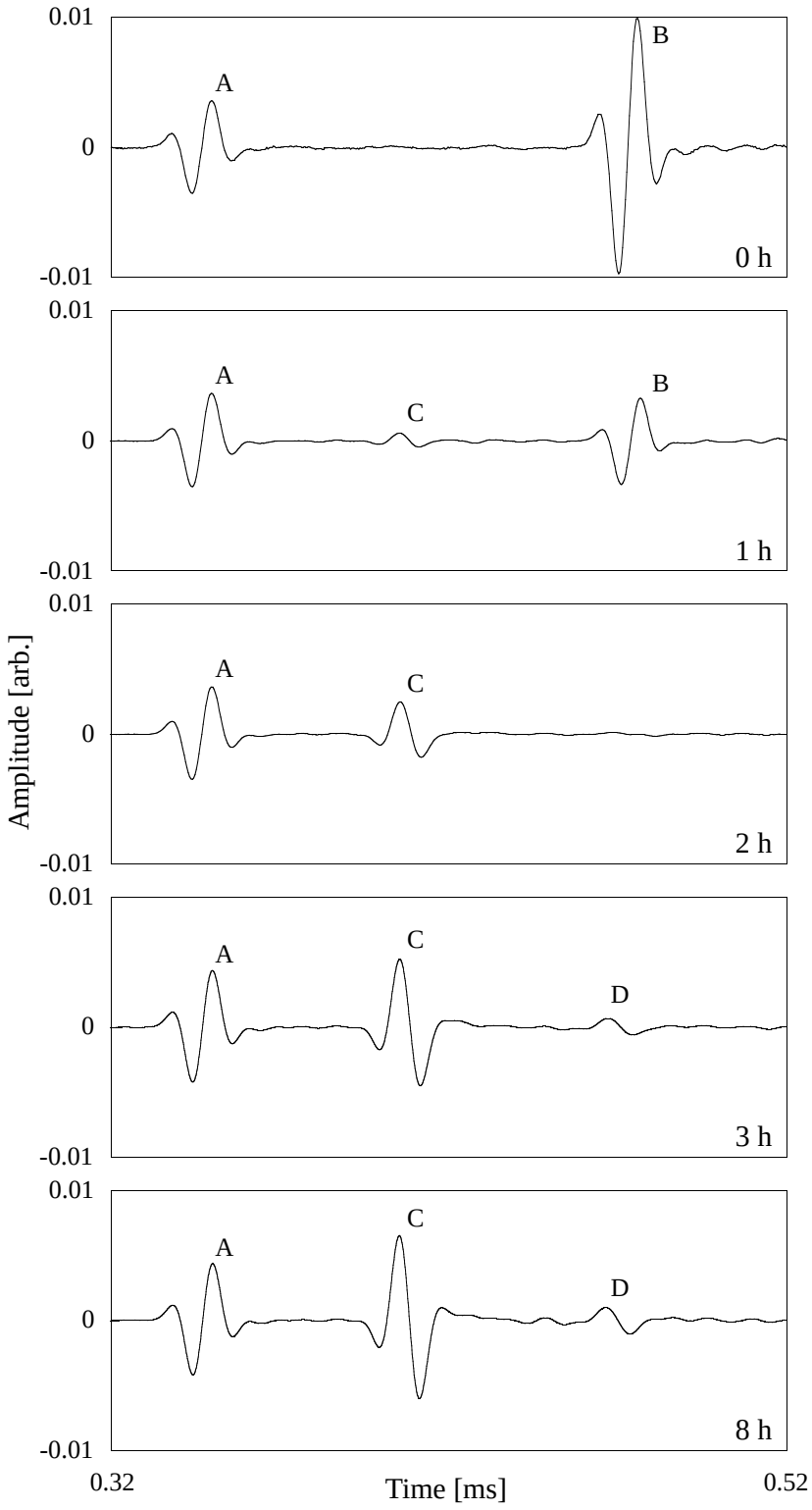

Figure 6.6: Time traces during a reflection coefficient cure measurement. The plot at 0 hours shows the time trace in the free wire before embedding.

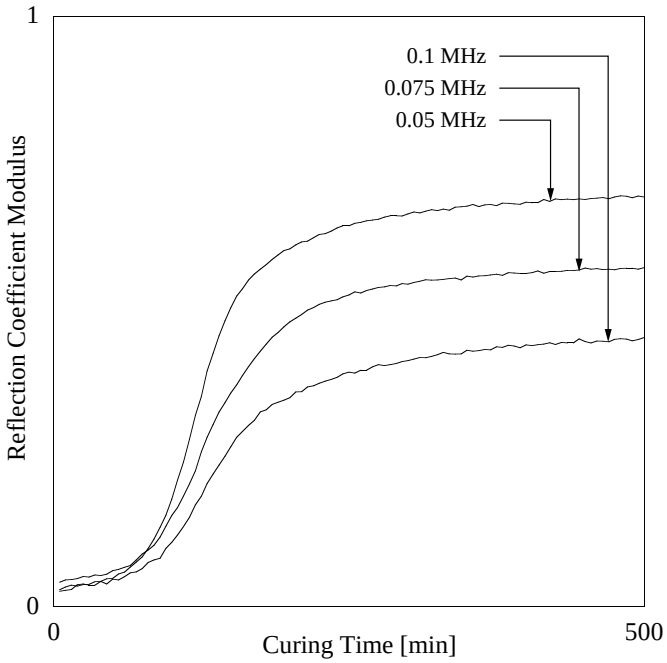

Figure 6.7: Cure monitoring curves obtained in Araldite 2013 with the reflection coefficient method at different frequencies.

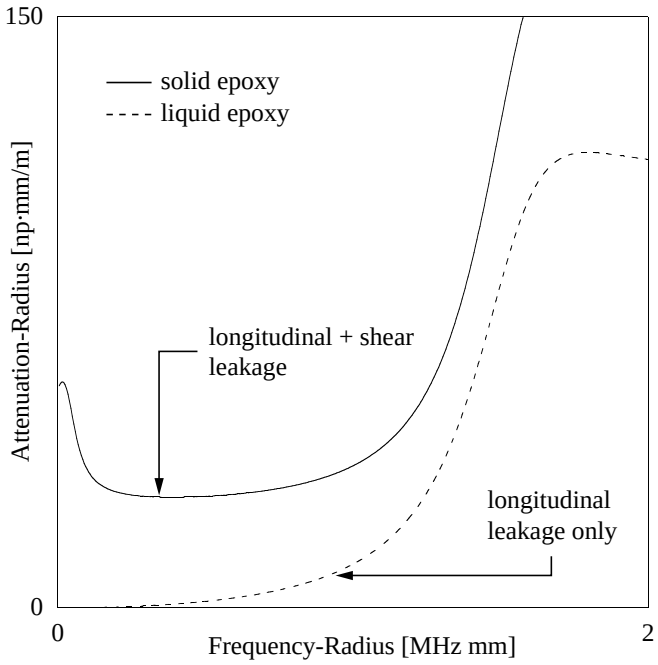

Figure 6.8: Predicted attenuation dispersion curves of L(0,1) for a steel wire embedded in a liquid and a solid epoxy. The material properties are given in Tab. 6.1.

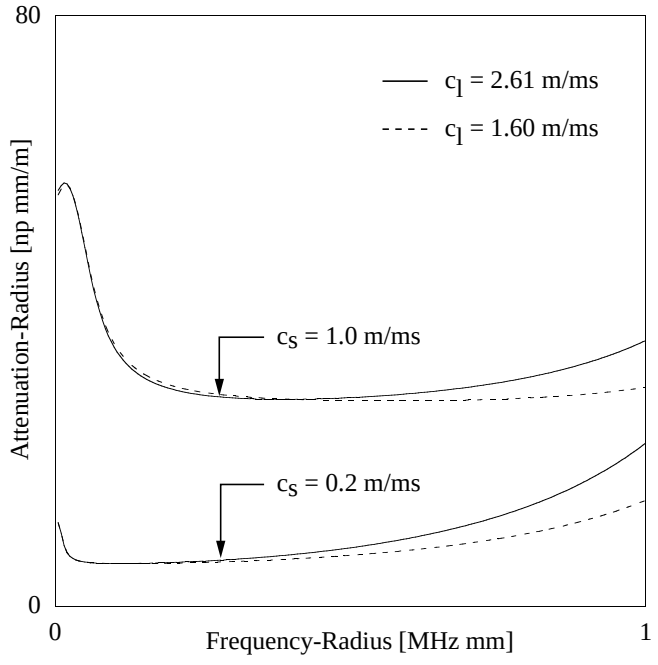

Figure 6.9: Predicted attenuation dispersion curves of L(0,1) in a steel wire for different epoxy longitudinal velocities for a solid epoxy ($c_s = 1.0\,\mathrm{m/ms}$) and an imaginary uncured epoxy resin with low shear velocity ($c_s = 0.2\,\mathrm{m/ms}$). The density of the epoxy resin in this analysis is $\rho = 1170\,\mathrm{kg/m^3}$, and the steel properties are given in Tab. 6.1.

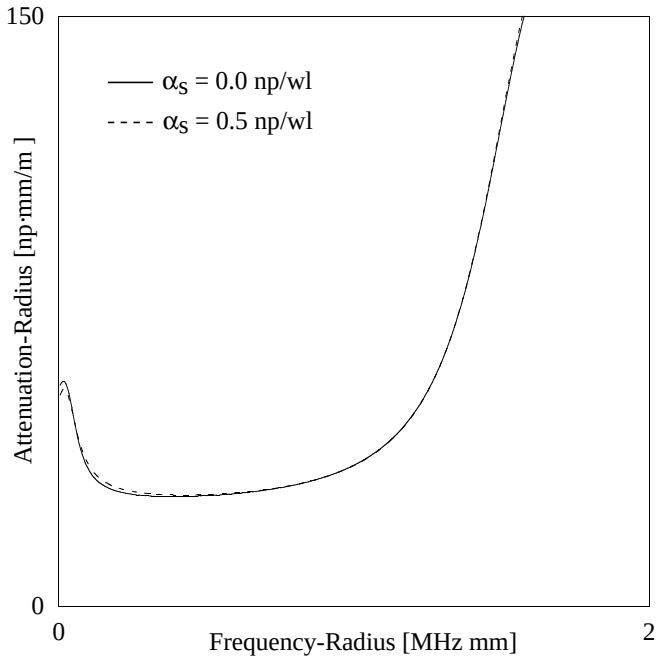

Figure 6.10: Predicted attenuation dispersion curves of L(0,1) for a solid epoxy (see Tab. 6.1) without attenuation (solid line) and with a constant attenuation of 0.5 np/wl (dashed line).

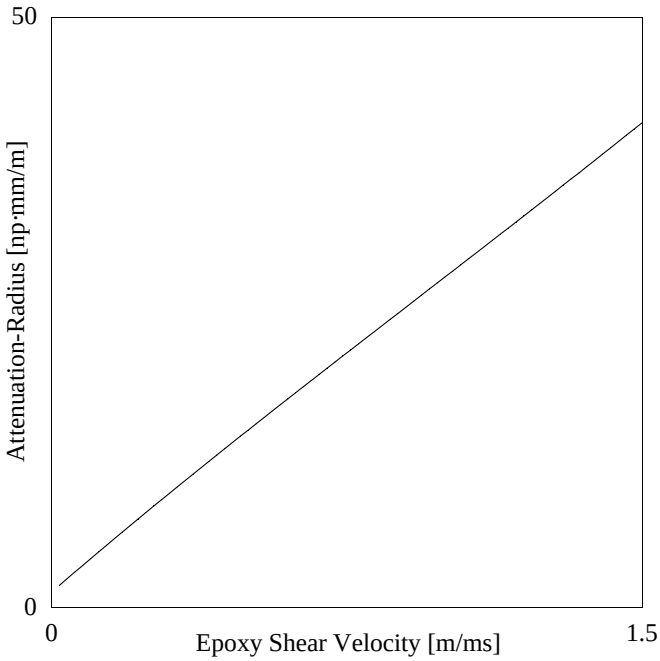

Figure 6.11: Predicted dependence of the L(0,1)-attenuation as a function of the solid epoxy shear velocity at 0.4 MHz mm.

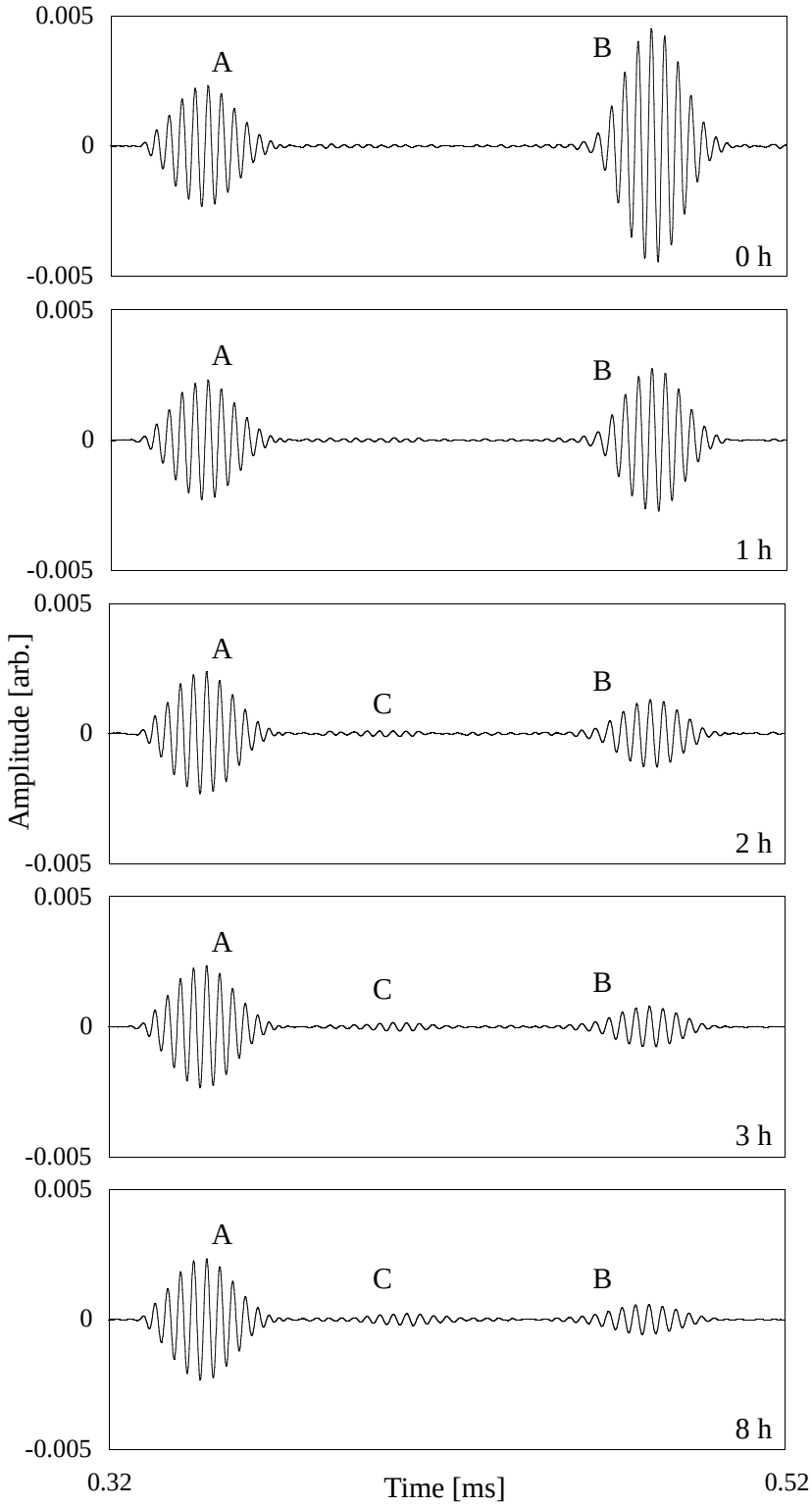

Figure 6.12: Time traces during an attenuation cure measurement. The plot at 0 hours shows the time trace in the free wire before embedding.

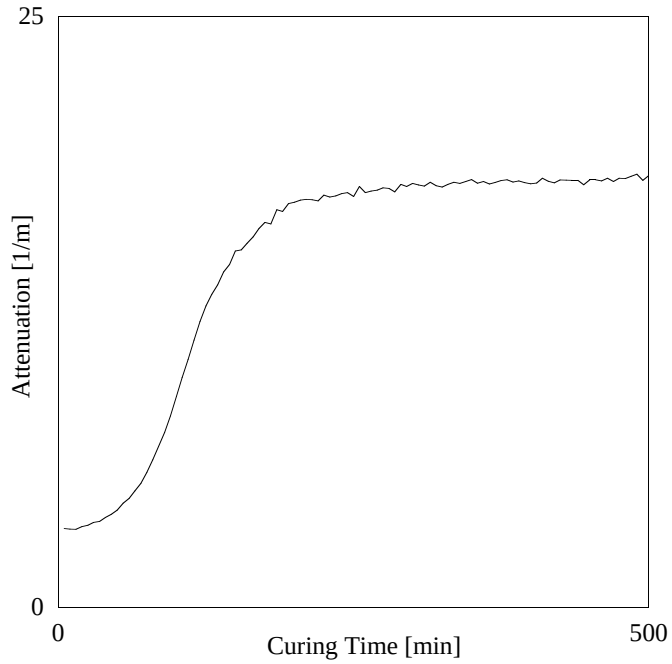

Figure 6.13: Cure monitoring curve obtained in Araldite 2013 with the attenuation method at 0.4 MHz mm.

Chapter 7

Effect of Entry Geometry on Reflection Coefficient

7.1 Background

In view of the original motivation to develop a testing tool for the cure monitoring of adhesives in automotive joints, the possible effect of the joint geometry on the reflection coefficient and the attenuation has to be discussed. As discussed in Sec. 6.3, the more favourable technique for the cure monitoring in thin joints is the reflection method, and thus the main emphasis in this chapter will be put on the reflection coefficient.

There are two main factors which potentially influence the magnitude of the reflection coefficient. Firstly, the shape of the entry geometry at the point where the wire waveguide enters the adhesive is in general not well defined in automotive joints. Instead of being perfectly square, as modelled in Ch. 5, the adhesive may take the shape of a meniscus, either due to surface tension, or simply due to spewing when the joint is assembled. Secondly, the thickness of the adhesive layer may possibly have an effect due to reflections of radiating waves inside the adhesive layer which can potentially feed back into the waveguide and interfere with the guided wave signal of interest. This is shown schematically in Fig. 7.1. The extent of these effects will be examined in the following using Finite Element (FE) modelling, and the analysis will be restricted to the fundamental longitudinal mode, L(0,1).

7.2 Effect of Meniscus

7.2.1 2D Finite Element Modelling

The effect of a meniscus is analysed using 2D-FE modelling in axi-symmetry. The model was idealised in such a way that the meniscus is assumed to take a cone-like shape, and the angle, δ, between the free surface of the embedding material and the direction of the cylinder axis is chosen as the parameter. Figure 7.2 shows a schematic of the FE model.

All the materials in the model are elastic. In view of the cure monitoring application, the embedding material was chosen to have the properties of a typical solid epoxy resin after cure. The material properties are given in Tab. 7.1.

Table 7.1: Material parameters used for the Finite Element analysis in Sec. 7.2.

Material	c_l [m/s]	c_s [m/s]	ρ [kg/m^3]
Steel	5960	3260	7932
Epoxy	2600	1200	1170

As a waveguide, a steel wire with a radius of 0.5 mm was modelled. As in the FE modelling presented in Sec. 5.5, a 1-cycle Hanning-windowed piston profile of 0.2 MHz centre frequency was applied at the free end of the cylinder. The size of the quadrilateral, four noded elements was first chosen as $\Delta x = 0.125$ mm. At a frequency of 0.2 MHz, the wavelength of L(0,1) is approximately 25 mm, so this corresponds to about 200 elements per wavelength. With a wire radius of 0.5 mm this is equivalent to only 4 elements over the radius of the wire. Also note that the lowest velocity of the materials in the FE model is the shear velocity of the embedding epoxy resin. Here, one wavelength corresponds to approximately 40 elements. The model was subsequently run with only 2 elements over the radius of the wire, and yielded identical results, thus demonstrating convergence. In order to reduce the computation time, the element size for the following analysis was therefore chosen as $\Delta x = 0.25$ mm. The length of the entire model in the axial

direction was 150 mm, and the embedding epoxy extended a maximum of 40 mm in the radial direction, so as to avoid interfering reflections from the end of the wire and the epoxy boundaries. The time step size was $\Delta t = 0.02\,\mu$s. The monitoring point was half way between the free end of the wire and the entry point.

7.2.2 Sensitivity of Reflection To Meniscus Angle

Seven different angles between 27° and 153° were modelled, including the perfectly square case which corresponds to an angle of 90°. The data analysis is equivalent to that in Sec. 5.5, and time traces are of the same form as shown in Fig. 5.10. A Fourier transform is applied individually to the incident and the reflected signal. The frequency dependent reflection coefficient is then obtained by dividing the amplitude spectrum of the reflected signal by that of the incident signal.

The modulus of the reflection coefficient for these cases is shown in Fig. 7.3. If the difference in angle compared to the square case, $\Delta\delta = 90° - \delta$, is small, then the difference in reflection coefficient for a given set of epoxy material properties is also small. As was already discussed in Sec. 5.6 (see also Fig. 5.17), the influence of the epoxy bulk longitudinal velocity on the reflection coefficient of L(0,1) is negligible. Hence, if the density of the epoxy resin is known, then the governing variable is the epoxy bulk shear velocity. Because of this, one can estimate the relative error in the shear velocity calculated from a measured reflection coefficient for a given uncertainty in the angle δ. For example, at 0.05 MHz, the relative error in the reflection coefficient, $\Delta R/R$, for an actual angle of 45° when an angle of 90° is assumed, is approximately 13%. Now the error in shear velocity has to be considered for a given error in the reflection coefficient. The sensitivity of the reflection coefficient to changes in the shear velocity was discussed in Sec. 6.4. It is found that this error in the reflection coefficient around a shear velocity of 1.2 m/ms and at 0.05 MHz mm would correspond to a relative error in the shear velocity of approximately $\Delta c_s/c_s = 9\%$.

This may still be acceptable in practical terms for the cure monitoring in an industrial setting. However, if the thickness of the joint also has an influence on the

reflection coefficient, errors may add up and become too high. The thickness effect is analysed in the following section.

7.3 Thickness Effect

7.3.1 Preliminary Experimental Findings

In order to investigate a possible effect of the joint thickness on the reflection coefficient, the following experiment was set up (see Fig. 7.4 for a schematic). A joint was assembled, consisting of a layer of adhesive, sandwiched between aluminium sheets of 2 mm thickness. The adhesive thickness was 3.4 mm, and three steel wires of different diameters (0.25 mm, 0.5 mm, and 1 mm) were embedded in the same joint sample so as to have the same material properties of the adhesive surrounding each wire. The entry point of the wires was kept as close to the mid-plane of the adhesive layer as possible. Also, the embedded length of the wires was such that no reflection from the end of the wire could be observed. In this way, it is possible to study the effect of the joint thickness, and that of the ratio between the diameter of the wire and the joint thickness.

It should be noted that the experimental procedure is problematic, especially in cases where the wire diameter is only slightly smaller than the joint thickness, since it is difficult to maintain the wires in a position exactly in the middle of the joint. This is mainly caused by the fact that the wires tend to curl. In some cases, wires may even touch one of the aluminium adherends, which introduces further experimental errors.

An additional practical difficulty which has become apparent in the course of this work is the fact that when handling wires with a radius comparable to or less than about 0.1 mm, kinks can easily be introduced by accident, which greatly diminishes the transmission of guided waves along the wire. Reliable results especially with these thin wires, intended for use in joints with a thickness down to 0.2 mm, may therefore be difficult to achieve in an industrial environment.

Figure 7.5 shows the reflection coefficient obtained experimentally as well as using Finite Element modelling for Araldite 2013. The techniques for this have already been presented in Sec. 5.7, and the solid line shows the FE predictions for bulk epoxy. The material properties for this analysis are shown in Tab. 7.2.

Table 7.2: Material parameters used for the Finite Element analysis in Fig. 7.5.

Material	c_l [m/s]	c_s [m/s]	ρ [kg/m^3]
Steel	5960	3260	7930
Epoxy	2120	1030	1170

Even though an adhesive thickness of 3.4 mm is fairly large for an automotive joint, which may range from about 0.2 mm to 2 mm, it can be seen that for the 1 mm diameter wire, which has the highest diameter to joint thickness ratio, the experimental results deviate from the predicted curve above around 0.1 MHz mm. The smaller the diameter of the wire, the closer the values are to the predicted curve. However, the frequency-radius dependence still seems to be preserved.

The thinner the adhesive layer becomes, the more significant the thickness effect becomes. As an example, Fig. 7.6 shows experimental data of the reflection coefficient of L(0,1) in steel wires for a 1.2 mm thick adhesive sample (Araldite 2017), sandwiched between two sheets of aluminium. In order to obtain a trend, interpolated lines between the experimental data points are also shown in the graph. It can be seen that the scattering of data points is large, and the data for the 1 mm diameter wire show an oscillating behaviour.

One possible explanation is that this behaviour stems from interference between the reflected guided wave and radiated waves scattered from the different layers of the joint, which could be feeding back into the wire waveguide. In order to investigate this, 2D- and 3D-FE modelling has been employed. This is discussed in the following sections.

7.3.2 2D Finite Element Modelling

In the 2D-FE axi-symmetric model the embedding epoxy is modelled as an outer cylindrical layer. As depicted in Fig. 7.7, any radiating wave will be reflected straight back onto the wire surface, and hence interfere with the guided wave. In this respect, the 2D-FE modelling is a worst case study, because in a real joint the radiating waves would also be scattered away from the waveguide, since the adherends are flat rather than circular and concentric (compare with Fig. 7.1). Also, the epoxy resin is modelled as an elastic solid. Therefore, the radiating waves are not attenuated except for beam spreading. In a real epoxy resin, in particular in the early stages of cure where the shear bulk attenuation is high, the radiating waves are attenuated. Hence the interference with the guided wave is less pronounced, since the amplitude of the back-scattered waves is smaller compared to the elastic case.

FE models were run for different radii R of the outer epoxy surface, which correspond in the 2D case to half the joint thickness d, so $R = d/2$ (see Fig. 7.8 for a schematic). The material properties for the model are given in Tab. 7.3. Free boundary conditions were chosen on the outer surface of the epoxy layer.

Table 7.3: Material parameters used for the 2D and the 3D FE analysis.

Material	c_l [m/s]	c_s [m/s]	ρ [kg/m^3]
Steel	5960	3260	7932
Epoxy	2610	1100	1170

Figure 7.9 shows the FE time traces obtained for joint thicknesses ranging from $d = 1.5\,\text{mm}$ to $d = 41\,\text{mm}$. As before, the first signal ("A") corresponds to the incident L(0,1)-mode. All the following signals are reflections from the entry point, from the outer epoxy layer surface, or successive reverberations. We concentrate now on the reflected signals.

It can be seen that for a thin outer epoxy layer with free boundaries ($d = 1.5\,\mathrm{mm}$), the reflected L(0,1), denoted by "B", is small. This is expected since for a vanishing epoxy layer thickness the reflection coefficient should also vanish. On the other hand, if rigid boundary conditions on the outside of the epoxy layer were chosen, the reflection would be large. Then, in the limit of vanishing thickness, the reflection coefficient of L(0,1) would take the value unity (see Sec. 5.6). For increasing epoxy layer thickness ($d = 2.0 - 2.5\,\mathrm{mm}$), the waveform of the reflected L(0,1) mode shows ringing, which suggests the presence of a resonance effect of interfering signals. At even larger epoxy layer thicknesses, a separation into two reflected signals can be observed. At $d = 21\,\mathrm{mm}$, the first of these signals, "C", is equivalent to the entry reflection obtained for the case when the epoxy layer is considered to extend infinitely in the radial direction. The second reflection, "D", is an L(0,1)-mode which has been excited by a radiating wave having been reflected back from the outer surface of the epoxy layer. It should be noted that this signal "D" is not well defined, and that the dashed box in the plot is for illustration only and is not meant to give exact limits to the signal duration. The last plot shows the time trace of the FE model which is equivalent to those which have been used to study the reflection of L(0,1) as presented in Ch. 5. Here, the reflected radiated signals are separated in time from the reflected L(0,1) modes such that they do not interfere any more.

The waves that radiate and are reflected back may be a combination of leaky bulk waves and also surface waves (Rayleigh type waves [65]) that propagate along the free surface of the epoxy. As an example, Fig. 7.10 shows a time trace monitored at the free surface of the embedding epoxy material at $r = 1.5\,\mathrm{mm}$ for an overall joint thickness of 41 mm, as indicated in Fig. 7.8 (point "X"). It can be seen that there is a signal, "A", which could be interpreted as a surface wave, since from monitoring at two different positions a wave speed of approximately $0.96\,\mathrm{m/ms}$ is calculated, and the velocity of a Rayleigh wave on a half-space of epoxy resin with those properties is $1.035\,\mathrm{m/ms}$. However, it should be noted that this signal changes shape as it is monitored further away from the wire and interferes with other signals. Also, since a radiating surface wave propagates radially outward, the amplitude decreases with distance form the wire due to beam spreading. Therefore only a rough estimation of

velocity is possible, and it proved difficult to determine conclusively which radiating modes contributed to the fields in the epoxy layer. Hence the comparison with the Rayleigh velocity can only serve as an indication, and one must therefore for the moment merely accept that there is an interference effect. However, this study is, as mentioned before, a worst case analysis since here all the radiating waves are reflected back on the waveguide surface. It remains to be evaluated if this effect is still significant when the waves are radiated from a wire into a plate-like epoxy layer as depicted in Fig. 7.1. This is discussed in the next section.

7.3.3 3D Finite Element Modelling

In order to evaluate the effect of radiated waves being scattered back from flat boundaries into the waveguide, a 3D FE-model of a steel wire of 0.5 mm radius in a plate-like layer of epoxy was created. A section of the mesh is shown in Fig 7.11(a).

The modelling parameters such as the excitation and the requirements for the element size and time steps are the same as outlined previously in Sec. 5.5; the material properties for all 3D-models are those given in Tab. 7.3. The model is divided into several solid regions made up of brick elements ("HX08", see FINEL manual [78]). The software FINEL supports a region command ("HCIR"), that generates elements over a solid region that lie on a circular arc (the edges of the brick elements are however straight). This is needed to correctly model the wire waveguide.

Figure 7.11(b) shows a more detailed section, showing the mesh geometry for the wire material and the surrounding epoxy in the immediate vicinity of the entry point. The cross-section of the wire is divided into three regions, which are made up of nine elements each. Due to the geometry of the joint, symmetry conditions can be applied and only one quarter of the joint has to be modelled.

The total number of elements required presents a considerable problem. The element size here is governed by the condition that the wire waveguide has to be modelled with sufficient accuracy, which requires 6 elements along the radius in the 3D-FE model. In order to avoid elements with excessive aspect ratios, the element size in

the axial direction was chosen as 0.1 mm, giving an aspect ratio of 5/6. Therefore, to model a wire of 150 mm length with no epoxy loading results in 40500 elements. With epoxy loading, depending on the thickness, d, of the epoxy layer, the number of elements can quickly exceed 250000 elements. Due to the computational difficulty in handling such large numbers of elements, the aluminium adherends were not modelled.

In order to keep the number of elements to a minimum, some of the elements in the epoxy layer were successively stretched by a factor of 1.4 in the lateral direction (y-direction of the schematic in Fig. 7.1) away from the wire. Such elements may not model wave propagation properly, however, the main interest does not focus on the radiating waves propagating in the lateral direction but on the guided wave in the wire. It should be noted that a change in the geometry of the element can cause reflections of a propagating wave due to the change in the impedance of the element. However, for a stretch factor of less than about 1.4, this error can be neglected [78].

Joint thicknesses between 1.5 mm and 3 mm in steps of 0.5 mm have been modelled. Since, due to the large number of elements, bulk epoxy could not be modelled, the reflection coefficients are compared to those from the 2D-FE modelling for bulk epoxy in Sec. 7.3.2.

As an example, Fig. 7.12 shows the time-trace of L(0,1) obtained from the 3D-FE modelling for a 0.5 mm radius wire in a 2.5 mm thick epoxy joint. It can be seen that the resonance effect due to interference of the entry reflection with the back-reflected radiated waves is still significant, even though it is less pronounced than in the 2D FE modelling (compare to the 2.5 mm case in Fig. 7.9).

The comparison of the reflection coefficients obtained using the 3D-FE modelling in different joint thicknesses and the bulk epoxy case obtained using 2D-FE modelling is shown in Fig. 7.13. At lower frequencies, the reflection coefficient for a joint is closer to that for the bulk material when the thickness of the joint is larger. However, for higher frequencies, the reflection coefficient from the joint is generally larger than

that for the bulk material, and still shows an undulating pattern. It is the same form of pattern as was observed in the experiments of Fig. 7.6.

Additionally, in order to complete the picture of the effect of the joint geometry on the guided wave propagation, the attenuation of the guided wave in the embedded section was analysed by monitoring along a line on the axis of the wire. From the amplitude change of the guided mode and the propagation length in the embedded section, the attenuation can be calculated according to Eq. (4.9). This was done using 3D-FE modelling for the joint geometry and using 2D-FE modelling for the bulk epoxy case. Figure 7.14 shows the attenuation dispersion curves obtained in this way together with the curve predicted by DISPERSE for a steel bar embedded in epoxy (the material properties are given in Tab. 7.3). It can be seen that the FE predictions for the bulk case are in accordance with the DISPERSE predictions, however, the attenuation dispersion curve for the joint geometry deviates significantly from the bulk attenuation.

7.4 Summary

The purpose of the study presented in this chapter was to demonstrate the effect of the entry geometry on the entry reflection. 2D- and 3D-FE modelling has shown that a meniscus and the thickness can significantly influence the reflection coefficient of L(0,1). This is due to the fact that radiating waves are reflected back into the waveguide and interfere with the entry reflection. The effect of the joint thickness was also experimentally examined, and the measured reflection coefficients show a similar undulating behaviour as the coefficients obtained from the FE modelling. FE simulations have shown that also the attenuation of L(0,1) is influenced by the thickness of the epoxy layer.

In Ch. 6 it was found that both the reflection and attenuation method can be used for the cure monitoring of bulk samples. However, due to the inherent unpredictability of the joint geometry in automotive joints in the industrial environments, the methods are not practical enough for this particular application. Nevertheless, even

though in this application the method is not suitable for quantitative measurements, it could still potentially be useful for qualitative time monitoring of the changes occurring during the cure cycle.

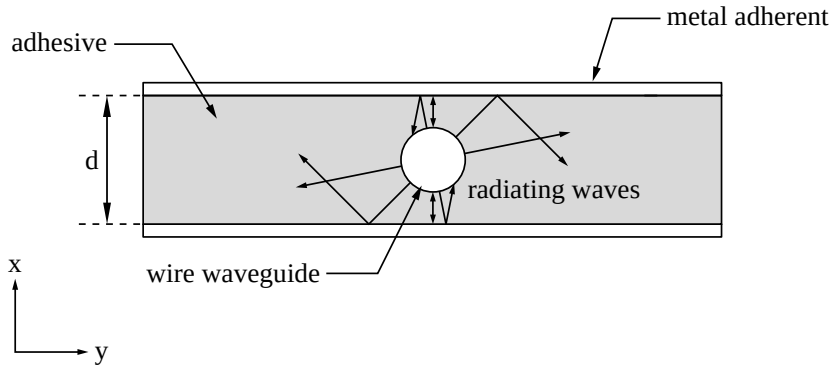

Figure 7.1: Schematic of radiating waves being reflected within the joint with view into the axial direction (z-direction). Note that only some example rays of these waves are shown. Of course, for an order zero mode like L(0,1), the waves radiate uniformly over the circumference of the waveguide.

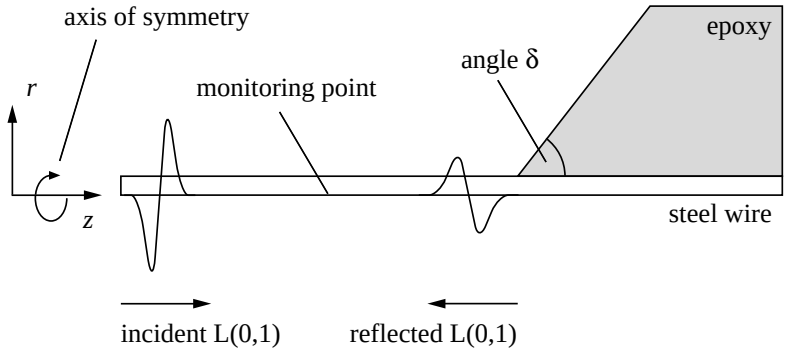

Figure 7.2: Schematic of the Finite Element model to study the influence of a meniscus on the reflection coefficient of L(0,1).

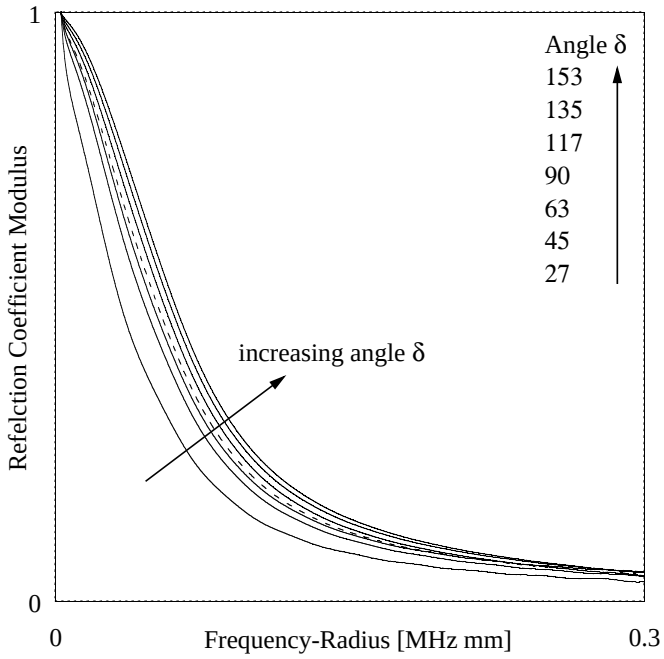

Figure 7.3: Finite Element reflection results for a steel wire embedded in epoxy for different angles δ (see Fig. 7.2). The dashed line corresponds to $\delta = 90°$.

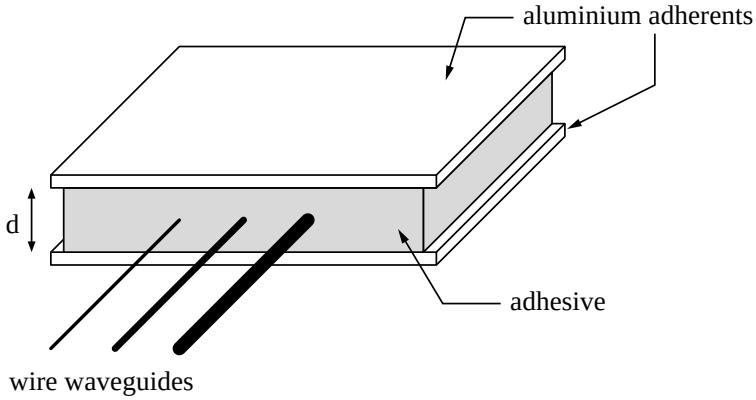

Figure 7.4: Schematic of the experimental set-up for studying the thickness effect. Waveguides of different diameters are placed inside an adhesive joint to measure the entry reflection of L(0,1).

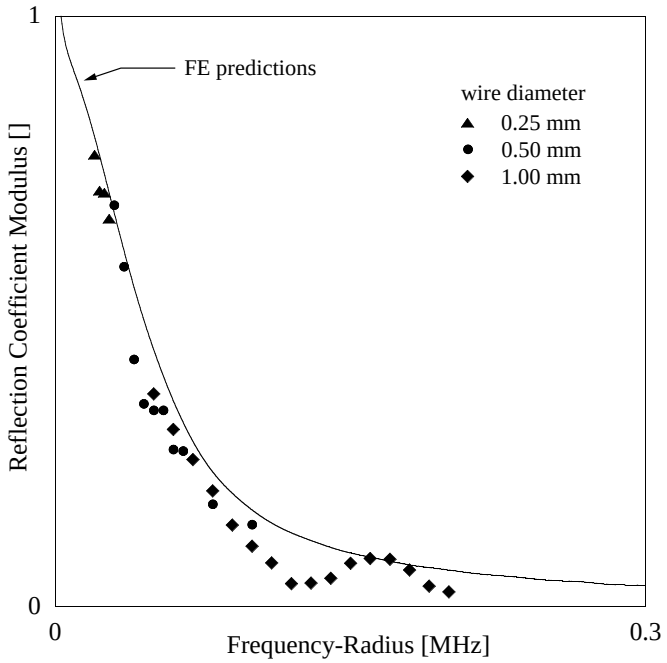

Figure 7.5: Experimental results (points) for steel wires of different diameters in a 3.4 mm thick adhesive joint (Araldite 2013). FE predictions for a steel wire partly embedded in bulk material of epoxy (solid line) are also shown.

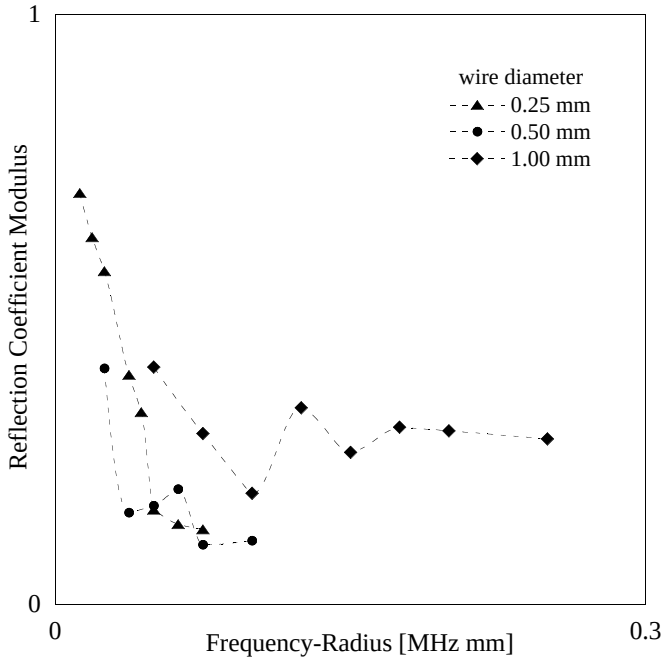

Figure 7.6: Experimental results (points) for steel wires of different diameters in a 1.2 mm thick adhesive joint (Araldite 2017). An interpolated trend-line is shown in dashed lines.

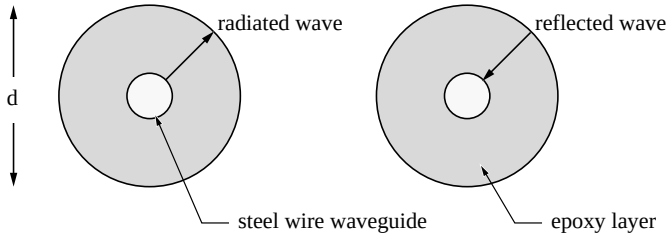

Figure 7.7: Schematic representation of radiating waves being reflected back from the outer surface of a finite epoxy layer onto the waveguide surface with view into the axial direction.

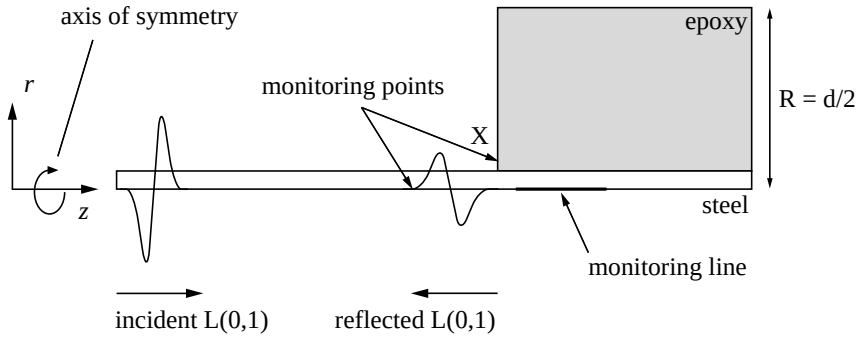

Figure 7.8: Schematic of the 2D-FE model. The outer radius of the epoxy layer, R, corresponds to half the joint thickness. The displacement amplitudes were monitored on the axis of the cylinder and on the free surface of the epoxy layer, at locations indicated by the arrows.

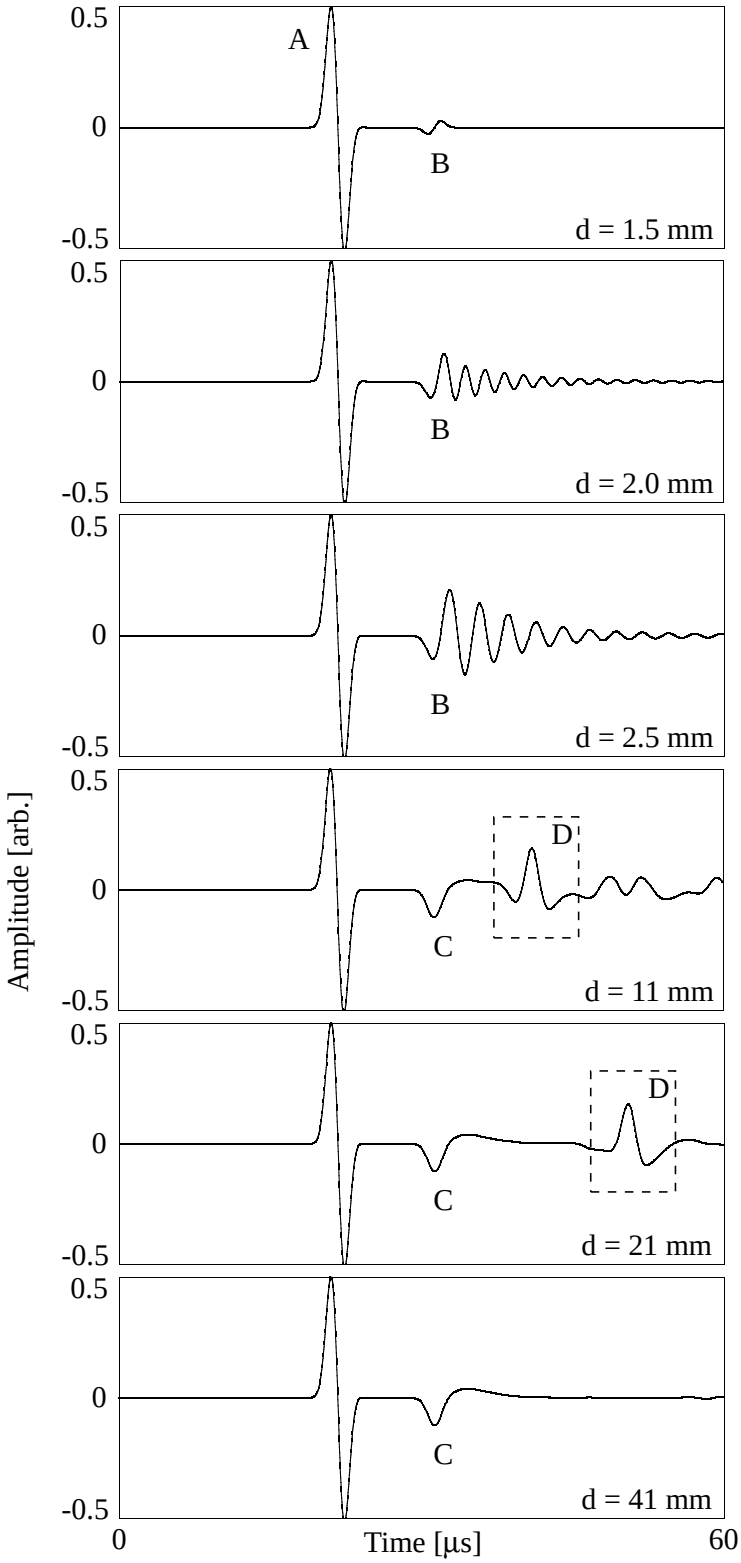

Figure 7.9: FE time traces obtained from the 2D-model for a 0.5 mm radius steel wire embedded in an outer epoxy cylinder of various diameters.

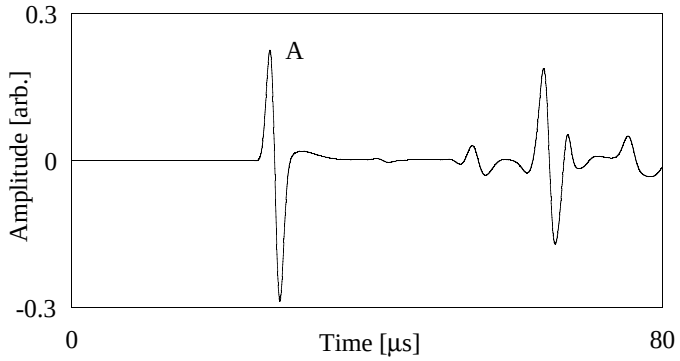

Figure 7.10: FE time traces obtained from the 2D-model for a 0.5 mm radius steel wire embedded in an outer cylinder of epoxy material ($d = 41$ mm). The monitoring point is on the free surface of the epoxy layer at $r = 1.5$ mm, as depicted in Fig. 7.8

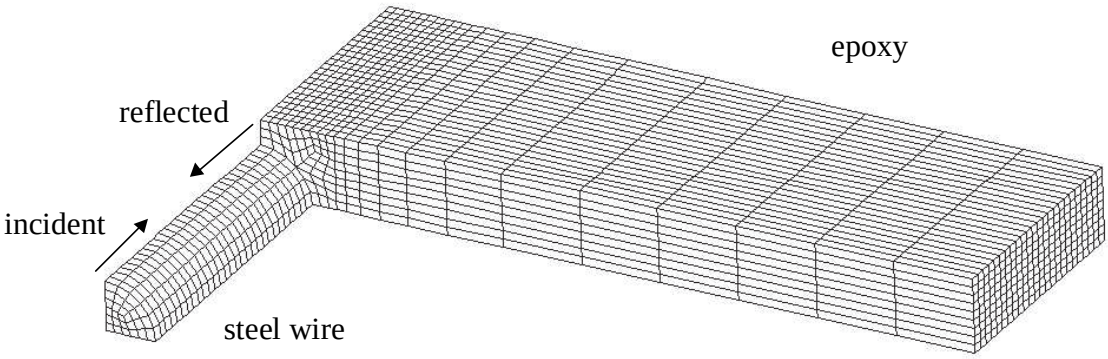

(a)

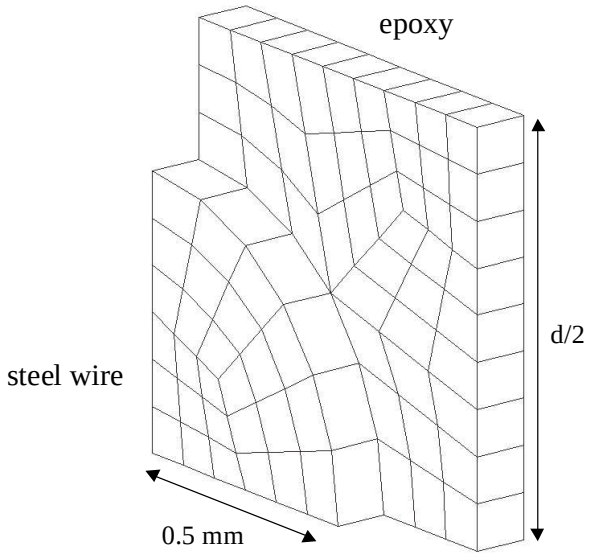

(b)

Figure 7.11: (a) Finite Element mesh for the 3D analysis. (b) Enlarged section of the mesh in the vicinity of the entry point.

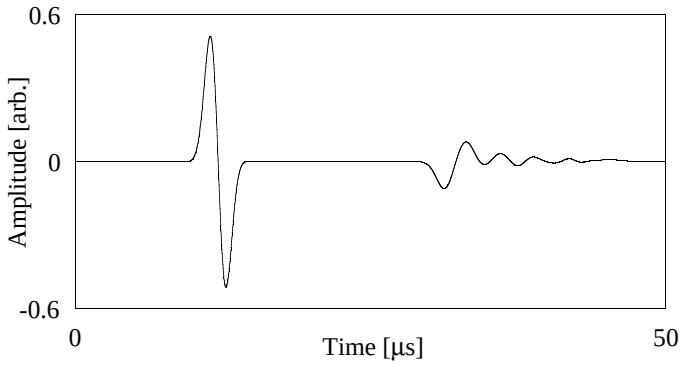

Figure 7.12: 3D-FE time trace of L(0,1) in a 0.5 mm radius steel wire in a 2.5 mm thick epoxy joint.

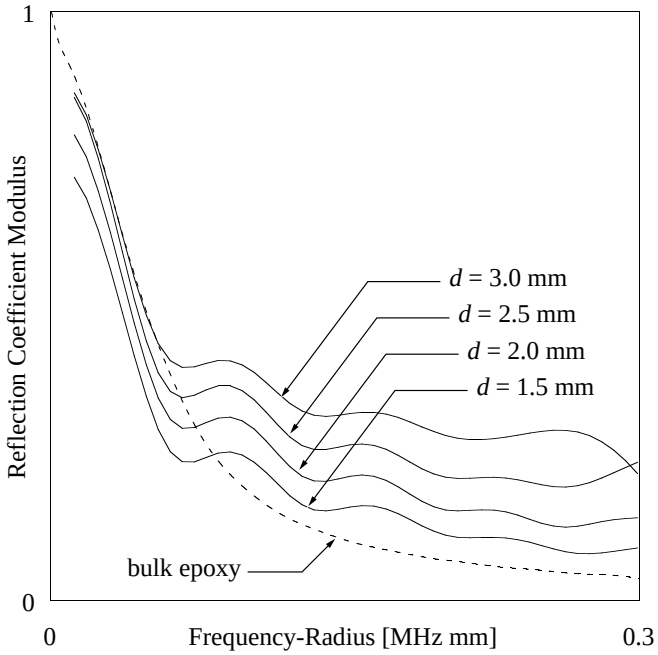

Figure 7.13: FE predictions of the reflection coefficient modulus for L(0,1) in a 0.5 mm radius steel wire embedded in flat epoxy layers of different thicknesses d. The bulk epoxy case modelled using 2D-FE is also shown (dashed line).

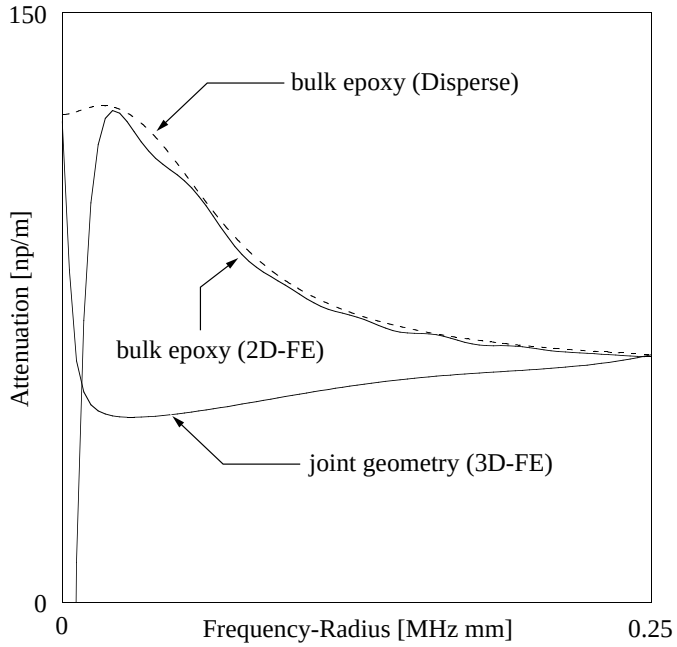

Figure 7.14: Attenuation dispersion curves of L(0,1) in a 0.5 mm steel wire embedded in bulk epoxy (2D-FE) and in an epoxy layer of thickness $d = 1.5$ mm. The DISPERSE prediction for a steel wire embedded in epoxy is also shown (dashed line).

Chapter 8

Conclusions

8.1 Summary

8.1.1 Basic Ideas

This thesis has examined the feasibility of using ultrasonic waveguide techniques for the measurement of the material properties of an embedding medium. Two methods in particular were investigated which have previously not received much attention regarding the quantitative prediction of material properties. The first method is based on the measurement of guided wave attenuation due to the leakage of bulk waves. The second method measures the reflection of a guided wave from the point where the waveguide enters the embedding medium. As was described in Ch. 1, the original motivation for this work comes from automotive industry, which is in need of an on-line monitoring technique to assess and control the curing process of adhesives in automotive joints.

The work has concentrated on ultrasonic wire waveguides, and therefore the theory of bulk waves and guided waves in cylindrical structures was reviewed briefly in Ch. 2. For reasons outlined in that chapter, the fundamental longitudinal mode, L(0,1), and the fundamental torsional mode, T(0,1), were identified as most suitable for testing.

Both magnetostrictive and piezoelectric transduction mechanisms were used to ex-

cite these modes, and they were discussed together with the general experimental set-up for both the attenuation and reflection coefficient measurements in Ch. 3.

8.1.2 Attenuation Method

When a waveguide is embedded in another material, the guided waves may lose energy due to the leakage of bulk waves. The guided wave attenuation over a given embedded length was measured by comparing the amplitudes of the guided waves before and after embedding the waveguide. Under certain conditions, which were described in Ch. 4, the measured attenuation can be related to material properties of the embedding material. Viscous liquids whose material properties are well documented were used to verify this method.

Numerical predictions, which use a solid-like model to describe viscous liquids, showed that the torsional mode attenuation is sensitive exclusively to the shear properties of an embedding material. The attenuation is an integral part of the dispersion curve calculation for the embedded waveguide system, and these calculations were performed with the software DISPERSE. From the attenuation measurement, the shear velocity, or alternatively the shear viscosity, could be calculated, thereby completely determining the shear properties. Experimental results demonstrated the validity of these predictions.

Also the longitudinal mode is, at low frequency-radius products, sensitive only to the shear properties of an embedding material, since here the attenuation is caused mainly by shear leakage. Numerical predictions were used to directly relate the measured longitudinal mode attenuation to the shear viscosity, and the experimental results were in very good agreement with literature data.

At higher frequency-radius products, the L(0,1)-attenuation is additionally caused by longitudinal bulk wave leakage due to the increased radial displacements on the surface of the waveguide. It was shown that, if the shear viscosity of the embedding liquid is known, for example by previous measurement using either the longitudinal mode at low frequency-radius products or the torsional mode, it is possible to

then directly determine the longitudinal bulk velocity from the measured L(0,1)-attenuation at higher frequency-radius products. Tests with distilled water, which has a negligible shear viscosity at room temperature, have shown good agreement with literature data. However, the results obtained using Glycerol were less accurate. Possible sources of error were outlined in the thesis.

8.1.3 Reflection Method

At the point where a waveguide enters an embedding material, a guided wave is reflected and scattered into other modes by mode conversion. This is caused by the change in the surface impedance. The larger this change, the larger is the magnitude of the entry reflection. This can be used to determine the material properties of the embedding medium. Since initially the experimental work concentrated on the longitudinal mode, L(0,1), the theoretical work in this thesis has also focused on this mode. However, most of the theoretical analysis is completely general, and can be easily repeated for the torsional mode.

The entry reflection coefficient of L(0,1) can be determined using Finite Element modelling. However, the computational analysis can be tedious, and problems arise when dealing with embedding materials with small bulk shear velocities. Therefore, an alternative numerical method based on modal analysis was developed in Ch. 5. The scattered field in the free and the embedded part of the waveguide can be represented by a superposition of the modal fields of the modes of the free waveguide and the modes of the embedded waveguide system. In this approach, the mode shapes of the guided waves are used to calculate the scattering coefficients of the modes involved.

First, the S-parameter approach laid out by Auld was compared to an analysis which matches the fields in the free and the embedded part of the waveguide at the interface. Since the solution was restricted to modes incident from the free part of the waveguide, it is sufficient to consider only the fields over the cross-section of the waveguide. Then, a complete modal solution was presented. For this, orthogonality and completeness of the waveguide modes is necessary, and the problems encountered

when considering orthogonality in leaky waveguide systems were discussed.

The modal solution was verified using Finite Element modelling, and very good agreement was obtained. The case where the embedding material is rigid was chosen as a reference case, because orthogonality is given for such a waveguide system. Apart from validating the numerical method, the analysis gave insight into the behaviour of non-propagating and inhomogeneous modes. Then, with respect to the cure monitoring application, the case where the embedding material is an epoxy resin was researched. Several characteristics of the L(0,1)-reflection coefficient in the frequency range of 0–0.3 MHz mm were found. Firstly, the reflection coefficient depends, like the dispersion curves, on the product of frequency and the radius of the waveguide. Secondly, the magnitude of the reflection coefficient is a strong function of the epoxy shear velocity, but is only minimally influenced by the value of the epoxy longitudinal velocity. Therefore, the entry reflection of L(0,1) can be used to determine shear properties of an embedding material. In general, the entry reflection is high at low frequencies and decreases with increasing frequency-radius product.

These predictions were also verified experimentally by measuring the entry reflection for a steel wire partly embedded in a cured epoxy resin.

8.1.4 Application to Cure Monitoring

In Ch. 6, the two measurement methods were successfully applied to the cure monitoring of bulk samples of epoxy resin. The analysis of the reflection coefficient of L(0,1) has shown that the reflection method can only be applied at low frequency-radius products, with a maximum sensitivity at around 0.05 MHz mm for a steel waveguide. On the other hand, the attenuation method can only be applied at higher frequency-radius products in order to avoid the entry reflection. These measurements were conducted at 0.4 MHz mm. At this frequency-radius product, the entry reflection is negligible and the dispersion of L(0,1) is only weak.

With both methods, typical cure monitoring curves were obtained, and it was pos-

sible to accurately determine the epoxy shear velocity of the cured sample. The room temperature curing epoxy resin Araldite 2013 was used for the experiments, and the results of both methods are consistent with each other and with literature data. The reflection method measures cure at the edge of the epoxy sample, whereas the attenuation method measures an average value over the embedded length. This is important because of the temperature variations which may occur at different positions in the sample and the sensitivity of cure to temperature.

One significant advantage of the waveguide method compared to conventional ultrasonic techniques is that the shear properties can be monitored over the whole cure cycle, including the period at the start of the curing process where the bulk shear attenuation is very high. Also, effects such as beam spreading do not occur. For the application in automotive joints, the wire waveguide method is potentially better suited than other cure monitoring methods, which were outlined in Sec. 6.2, because it solves the problem of accessing the joint in the industrial process. The transducers and the testing equipment can be placed outside the curing oven.

The reflection method is more attractive for the application in thin automotive joints. The reason for this is that thin wires have to be used and at the same time lower frequencies are preferred for long range transmission. Hence the frequency-radius product must be small. Also, the calibration procedure is easier for the reflection method.

However, it was found in Ch. 7 that the geometry has a significant effect on both the reflection coefficient and the attenuation. A meniscus at the entry point as well as different thicknesses of an epoxy layer, simulating a joint geometry, were considered using Finite Element modelling. The effect of a meniscus was investigated by modelling the meniscus in the form of a cone with different opening angles, and an estimate of the error in the calculated shear velocity when assuming a square entry geometry was given. Regarding the thickness effect, both a 2D- and a 3D-Finite Element analysis revealed that the waves that radiate away from the wire in the embedded section are scattered back from the boundaries of the joint, thereby

interfering with the entry reflection. Since this effect is significant and there is uncertainty in the thickness of the joint in the industrial conditions, quantitative results cannot be obtained in this case. Nevertheless, the method may still potentially be used for qualitative time monitoring of the cure process.

8.2 Outlook

The work described in this thesis has demonstrated the feasibility of using waveguide methods for the measurement of material properties. Several opportunities for further research emerged in the course of the investigation.

8.2.1 Attenuation Method

The attenuation method has concentrated on the fundamental longitudinal and torsional modes in wire waveguides. The measurement of the longitudinal properties of viscous liquids using L(0,1) at higher frequency-radius products needs further validation, and possible sources of errors which were outlined in the thesis have to be identified conclusively.

8.2.2 Reflection Method

The numerical modelling of the reflection method using the modal analysis should be repeated using the torsional mode. This is mainly for further validation, but also because the torsional mode is better suited than the longitudinal mode for the measurement of shear properties, and future measurements should use this mode.

The assumption of waveguide mode orthogonality in leaky waveguides needs to be addressed for the full modal solution which includes modes that are incident from the embedded part of the waveguide.

8.2.3 Applications

The original application to monitor the cure process of epoxy resins can be further validated by simultaneously measuring the cure using conventional ultrasonic meth-

ods in the same sample. Cure monitoring curves could then be directly compared. These measurements would complement each other since the waveguide method can measure shear properties throughout the cure cycle which is not feasible using conventional methods.

Both methods however have a much wider range of application to the measurement of material properties in general. The properties of any material which changes phase are accessible by these methods, for example solidifying concrete, and in particular the attenuation method can be applied to the process monitoring of liquids. Also highly attenuative materials, whose material properties are difficult to obtain, could be researched. As already mentioned in Ch. 1, the attenuation method has been successfully applied for example to the measurement of soil shear and longitudinal velocities [4].

Appendix A

Propagating, Non-Propagating and Inhomogeneous Modes

Three types of waveguide modes have been mentioned in Ch. 5 which need further explanation: propagating, non-propagating and inhomogeneous modes. Their classification is based on the complex wavenumber in the axial direction, $k = \xi - i\alpha$, according to the following definitions:

- for k pure real → propagating mode,
- for k pure imaginary → non-propagating mode,
- for k complex → inhomogeneous mode.

This means that, in a perfectly elastic waveguide in vacuum, there exist solutions for which the waveguide mode experiences spatial exponential attenuation, arising from a non-zero imaginary part of the wavenumber. Those modes do not propagate energy, and this is analysed in this appendix.

Consider a complex relationship for two modes (μ,m) and (ν,n) as derived by Auld ([65], p. 157), which is very similar to the real relationship of Eq. (5.8):

$$i(k_m - {k_n}^*) \int_S \{\mathbf{v}_m^\mu \cdot \mathbf{T}_n^{\nu *} + \mathbf{v}_n^{\nu *} \cdot \mathbf{T}_m^\mu\} \hat{\mathbf{z}}\, dS = 0. \tag{A.1}$$

Defining

$$P_{m\,n}^{\mu\,\nu} = -\frac{1}{4} \int_S \{\mathbf{v}_m^\mu \cdot \mathbf{T}_n^{\nu *} + \mathbf{v}_n^{\nu *} \cdot \mathbf{T}_m^\mu\} \hat{\mathbf{z}}\, dS, \tag{A.2}$$

this can be written in an abbreviated notation:

$$-4i(k_m - {k_n}^*)P^{\mu\,\nu}_{m\,n} = 0. \tag{A.3}$$

From this, either $k_m = {k_n}^*$, or $P^{\mu\,\nu}_{m\,n} = 0$. This is called the complex orthogonality relationship [65]. Considering a single mode, say (μ,m), this becomes

$$-4i(k_m - {k_m}^*)P^{\mu\,\mu}_{m\,m} = 0, \tag{A.4}$$

where $P^{\mu\,\mu}_{m\,m}$ is the average power flow of that mode (see also Eq. (5.18)). For a propagating mode, where $k_m = {k_m}^*$ (pure real), the average power flow is non-zero and can be normalised to unity. However, for a purely imaginary or complex wavenumber, the imaginary terms do not cancel out:

$$-8\alpha_m P^{\mu\,\mu}_{m\,m} = 0, \tag{A.5}$$

and therefore the power flow must vanish.

The consequence is that inhomogeneous and non-propagating modes do not propagate energy. This is best seen by considering the energy velocity of a guided wave, which is defined as

$$v_e = \frac{P}{E} \tag{A.6}$$

(see, for example, [65]). Here, P is the average power flow (the indices have been omitted for clarity), and E is the total time-averaged energy of the guided wave (see also Appendix B). The energy velocity of non-propagating and inhomogeneous modes is therefore zero. Hence, these modes do not propagate away from the point where they are created, either by direct excitation or through mode conversion, but are merely a local vibrations whose amplitudes decay spatially with $e^{-\alpha z}$.

In general, a given mode can be propagating a higher frequencies and become non-propagating or inhomogeneous at lower frequencies. The frequency at which this transition occurs is called the "cut-off" frequency (see Sec. 5.4 for an example).

Appendix B

Mode Orthogonality in Embedded Waveguides

B.1 Preliminary Considerations

The purpose of the following remarks is to give some insight into the problems encountered when considering mode orthogonality in embedded waveguide systems. Some questions remain unanswered and are subject to further research which is not within the scope of this thesis.

It has to be mentioned that the fields attributed to a given mode may not be limited to the boundaries of the structure which is considered to be the waveguide. As an example, consider a steel plate which is immersed in water. There exists a non-leaky mode, the so-called "Scholte" mode, whose phase velocity is lower than the bulk velocity of water (see Fig. B.1). The modal field in the embedding water half-spaces of this mode decays exponentially in the normal direction, y, away from the plate surface. An argument that the fields in the water actually form part of the guided wave is as follows:

It can be shown that, for a waveguide mode with zero attenuation, the energy velocity is equal to the group velocity, which is defined as

$$v_{gr} = \frac{\partial \omega}{\partial \xi} \tag{B.1}$$

(see [65], p. 201). The energy velocity for guided waves in plates is in general defined over the thickness, d, of the waveguide:

$$v_e = \frac{P}{E} = \frac{\int_{-d/2}^{+d/2} < p > \, dy}{\int_{-d/2}^{+d/2} < e > \, dy}, \tag{B.2}$$

where $<>$ denotes the time average of the quantity inside the brackets over one cycle, p is the power flow density, and e is the total energy density of the guided mode. This definition is appropriate for modes which are in vacuum, and would indeed also be valid if only the fields in the waveguide would form part of the guided wave. However, if in the case of the Scholte mode the fields in the water are part of the same mode, the definition should be changed by adjusting the integration limits to give

$$v_e = \frac{\int_{-\infty}^{+\infty} < p > \, dy}{\int_{-\infty}^{+\infty} < e > \, dy}, \tag{B.3}$$

Since the attenuation of the Scholte mode is zero, the group velocity should, as mentioned above, equal the energy velocity. Figure B.2 shows a comparison between the group velocity, calculated according to Eq. (B.1), and the energy velocities calculated according to the definitions given in Eq. (B.2) and (B.3), respectively. It is evident from this calculation that the integration including the half-spaces to either side of the plate gives the correct solution, and that therefore the fields in the water have to be considered part of the guided wave.

These findings may be closely related to mode orthogonality. The question which arises from this is if the orthogonality relationships for guided waves used in this thesis have to be defined such that they include embedding half-spaces. The above exercise certainly supports this for non-leaky modes. Here, a closed form integration from $-\infty$ to $+\infty$ was possible due to the fact that the fields decay exponentially and vanish at the integration limits. This is not so straightforward for leaky modes, since for embedded plate-like structures, as was mentioned in Sec. 5.3.4, the modal fields actually increase exponentially away from the interface, resulting in a diverging

integral. Also, a similar check using the energy velocity argument is not possible here, since the group velocity definition is not valid for attenuated waves [102]. Because of this problem, orthogonality for leaky modes in cylinders will be discussed in the next section as being defined over the cross-section of the waveguide only. Nevertheless, it has to be acknowledged that orthogonality may have to be defined including the embedding half-spaces.

B.2 Comparison to Mode Orthogonality in Free Waveguides

The real reciprocity relation of Eq. (5.3) is also valid for embedded waveguides. Therefore, to examine waveguide mode orthogonality in embedded waveguides, the same approach as presented in Sec. 5.2.2 can be followed here, and the first part of the analysis is identical.

We step in at Eq. (5.6), which reads:

$$\int_S \frac{\partial}{\partial z} \left\{ \mathbf{v}_n^\nu \cdot \mathbf{T}_m^\mu - \mathbf{v}_m^\mu \cdot \mathbf{T}_n^\nu \right\} \hat{\mathbf{z}} \, dS + \oint_C \left\{ \mathbf{v}_n^\nu \cdot \mathbf{T}_m^\mu - \mathbf{v}_m^\mu \cdot \mathbf{T}_n^\nu \right\} \hat{\mathbf{r}} \, dl = 0, \tag{B.4}$$

For free waveguides and waveguides with rigid boundaries, it was seen that the second integral on the left hand side vanishes because either the stresses or the particle velocities are zero on the waveguide surface. However, in embedded waveguides, the boundary conditions are not so simple, and it cannot be seen directly if the integral vanishes in this case. Therefore, the nature of the line integral in Eq. (B.4),

$$\oint_C \{\cdots\} \, \hat{\mathbf{r}} \, dl, \tag{B.5}$$

has to be examined in more detail. Here, the expression $\{\mathbf{v}_n^\nu \cdot \mathbf{T}_m^\mu - \mathbf{v}_m^\mu \cdot \mathbf{T}_n^\nu\}$ has been replaced by $\{\cdots\}$. The integral is evaluated as follows (omitting the $e^{i\omega t}$-dependence):

$$\oint_C \{\cdots\} \, \hat{\mathbf{r}} \, dl = \int_{\Theta_0}^{\Theta_0+2\pi} \left\{ \mathbf{v}_n^\nu \cdot \mathbf{T}_m^\mu - \mathbf{v}_m^\mu \cdot \mathbf{T}_n^\nu \right\} (R,z) \hat{\mathbf{r}} \, e^{i(\nu+\mu)\theta} \, R \, d\Theta, \tag{B.6}$$

where R is the radius of the waveguide. The integration yields:

$$\oint_C \{\cdots\}\,\hat{\mathbf{n}}\,dl = \begin{cases} 2\pi R\left\{\mathbf{v}_n^\nu \cdot \mathbf{T}_m^\mu - \mathbf{v}_m^\mu \cdot \mathbf{T}_n^\nu\right\}(R,z)\,\hat{\mathbf{r}} & \text{for } \nu = -\mu \\ 0 & \text{for } \nu \neq -\mu. \end{cases} \tag{B.7}$$

Replacing this into equation (B.4), the expression becomes

$$\int_S \frac{\partial}{\partial z}\{\cdots\}\,\hat{\mathbf{z}}\,dS = \begin{cases} -2\pi R\left\{\mathbf{v}_n^\nu \cdot \mathbf{T}_m^\mu - \mathbf{v}_m^\mu \cdot \mathbf{T}_n^\nu\right\}(R,z)\,\hat{\mathbf{r}} & \text{for } \nu = -\mu \\ 0 & \text{for } \nu \neq -\mu. \end{cases} \tag{B.8}$$

Carrying out the differentiation on the left hand side of the equation, the relationship for embedded waveguides becomes

$$\begin{aligned} & i(k_n + k_m) \int_S \{\cdots\}\,\hat{\mathbf{z}}\,dS \\ & \quad = \begin{cases} 2\pi R\left\{\mathbf{v}_n^\nu \cdot \mathbf{T}_m^\mu - \mathbf{v}_m^\mu \cdot \mathbf{T}_n^\nu\right\}(R,z)\,\hat{\mathbf{r}} & \text{for } \nu = -\mu \text{ and } n \neq -m \\ 0 & \text{for } \nu \neq -\mu \text{ and } n \neq -m. \end{cases} \end{aligned} \tag{B.9}$$

It can be seen from this that the angular orthogonality relationship is still valid as in the free and rigid boundary cases. However, the expression on the right hand side does not vanish for two modes of circumferential order zero, and thus orthogonality is not ensured in this case.

B.3 Consequences for Scattering Coefficient Calculation

The question of whether for the orthogonality relation the embedding half-spaces have to be included or if it is valid to define the relationship over the cross-section of the waveguide alone, has a direct influence on the calculation of the scattering parameters when the guided mode is incident from the embedded section of the waveguide.

If the modal fields in the half-spaces form part of the guided wave, then the analysis has to include the free surface of the embedding material. For the modal solution, as presented in Sec. 5.3.4, the boundary conditions have not only to be fulfilled over the cross-section of the waveguide, but on the entire plane at $z = 0$ (see Fig. 5.2).

For this reason, the scattering analysis has been carried out only for modes which are incident from the free section of the waveguide. This is satisfactory from the practical point of view and the scope of this thesis, which encounters only such cases, for example in the cure monitoring application. However, the full scattering solution remains an interesting topic for future work.

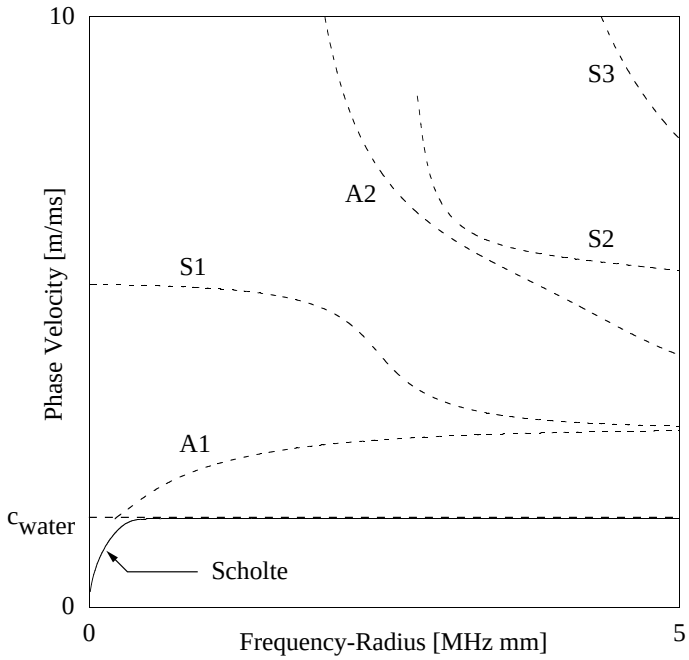

Figure B.1: Phase velocity dispersion curves for a steel plate immersed in water. The non-leaky mode (solid line) below the bulk velocity of water is called a "Scholte mode". The other symmetric (S) and anti-symmetric (A) plate modes are plotted in dashed lines.

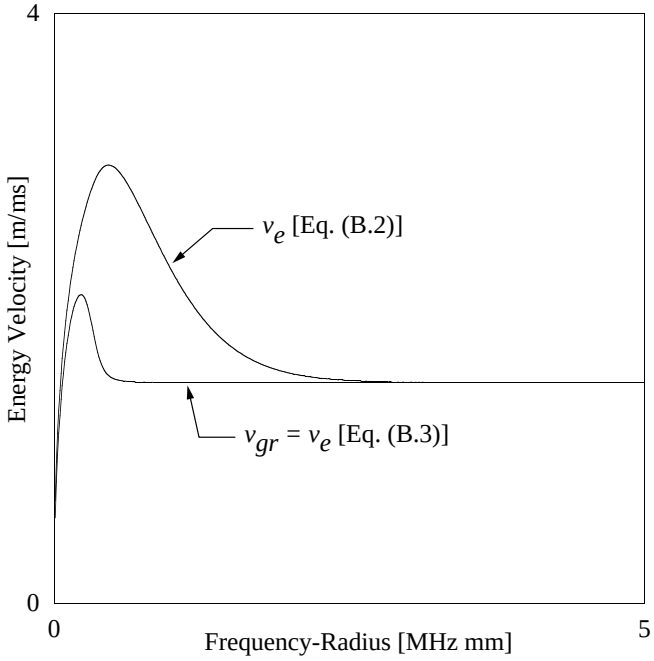

Figure B.2: Energy velocity of the Scholte mode in a steel plater immersed in water, calculated according to Eqs. (B.2) and (B.3). The energy velocity calculated with Eq. (B.3) is identical to the group velocity, which is defined in Eq. (B.1).

Appendix C

Maximum Attenuation in the Hysteretic Damping Model

In order to minimise the modelling effort when considering highly attenuating viscoelastic materials, it is worth considering what the maximum shear bulk attenuation in the direction of propagation could be. As described in Ch. 2, the software DISPERSE adopts a hysteretic damping model [15], where the complex shear velocity is given by the expression

$$c_s = \frac{\omega}{k} = \sqrt{\frac{\mu + i\mu'}{\rho}}. \tag{C.1}$$

Excluding the case where $\mu = 0$, we introduce the dimensionless parameter $\bar{\mu}$, defined by:

$$\bar{\mu} = \frac{\mu'}{\mu}. \tag{C.2}$$

Squaring and transforming Eq. (C.1) yields:

$$k^2 = k_{\mathrm{re}}^2 + 2ik_{\mathrm{re}}k_{\mathrm{im}} - k_{\mathrm{im}}^2 = \omega^2 \frac{\rho}{\mu} \frac{1}{1 + i\bar{\mu}}, \tag{C.3}$$

where the complex wavenumber k has been expressed by its real and imaginary part, k_{re} and k_{im}. Both the real and the imaginary parts of this equation must be equal. The real part gives

$$k_{\mathrm{re}}^2 - k_{\mathrm{im}}^2 = \omega^2 \frac{\rho}{\mu} \frac{1}{1 + \bar{\mu}^2}, \tag{C.4}$$

and the imaginary part gives

$$2k_{\mathrm{re}}k_{\mathrm{im}} = -\omega^2 \frac{\rho}{\mu} \frac{\bar{\mu}}{1 + \bar{\mu}^2}. \tag{C.5}$$

These equations can be combined, and after some algebra, the real part of the wavenumber is found to be of the form

$$k_{\mathrm{re}} = \sqrt{\frac{\omega^2\rho}{2\mu}}\sqrt{\frac{1+\sqrt{1+\bar{\mu}^2}}{1+\bar{\mu}^2}}, \tag{C.6}$$

and the imaginary part becomes

$$k_{\mathrm{im}} = -\sqrt{\frac{\omega^2\rho}{2\mu}}\frac{\bar{\mu}^2}{\sqrt{1+\bar{\mu}^2}\left(1+\sqrt{1+\bar{\mu}^2}\right)} \tag{C.7}$$

The bulk shear attenuation in nepers/wavelength is defined as

$$\alpha\,[\mathrm{np/wl}] = 2\pi\frac{k_{\mathrm{im}}}{k_{\mathrm{re}}}. \tag{C.8}$$

Replacing Eqs. (C.6) and (C.7) into the above expression yields a formula for the attenuation which depends on the dimensionless quantity $\bar{\mu}$ only:

$$\alpha\,[\mathrm{np/wl}] = 2\pi\,\frac{\bar{\mu}}{1+\sqrt{1+\bar{\mu}^2}}. \tag{C.9}$$

The maximum of this expression with respect to the variable $\bar{\mu}$ is 2π. This is also true when the dimensionless parameter $\bar{\mu}$ itself depends on the frequency, ω. Figure C.1 shows a graph of the attenuation in nepers per wavelength as a function of $\bar{\mu} = \mu'/\mu$. It should be noted that in the limit of $\mu \to 0$, the attenuation becomes 2π, which is the same value as obtained for viscous liquids in Sec. 4.3. In the limit $\mu' \to 0$, that means in the zero damping limit, the material is purely elastic, and the attenuation is zero. This analysis can easily be repeated for longitudinal bulk waves, also yielding a maximum attenuation value in np/wl of 2π.

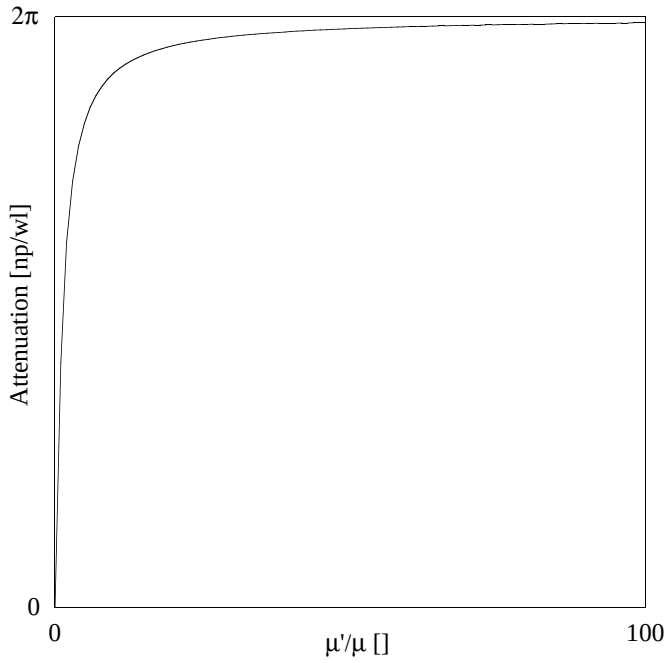

Figure C.1: Shear bulk attenuation in np/wl as a function of the dimensionless variable μ'/μ.

References

[1] I. N. Moody, P. A. Fay, and G. D. Suthurst. *Can adhesives meet the challenge of vehicle bodyshell construction?* Elsevier Applied Science, 1986.

[2] R. T. Harrold and Z. N. Sanjana. Acoustic waveguide monitoring of the structural integrity of composite materials. *Polymer Engineering and Science*, 26(5):367–372, 1986.

[3] R. J. Freemantle and R. E. Challis. Combined compression and shear wave ultrasonic measurements on curing adhesive. *Measurement Science and Technology*, 9:1291–1302, 1998.

[4] R. Long, K. Vine, M. J. S. Lowe, and P. Cawley. The effect of soil properties on acoustic wave propagation in buried iron water pipes. In D. O. Thompson and D. E. Chimenti, editors, *Review of Progress in Quantitative NDE*, volume 21, pages 1310–1317. American Institute of Physics, New York, 2002.

[5] B. N. Pavlakovic, M. J. S. Lowe, D. N. Alleyne, and P. Cawley. Disperse: A general purpose program for creating dispersion curves. In D. O. Thompson and D. E. Chimenti, editors, *Review of Progress in Quantitative NDE*, volume 16, pages 185–192. Plenum Press, New York, 1997.

[6] B. N. Pavlakovic and M. J. S. Lowe. *Disperse Manual - A system for generating dispersion curves.* NDT Laboratory, Imperial College, Web: www.me.ic.ac.uk/dynamics/ndt, 2001.

[7] K. F. Graff. *Wave motion in elastic solids.* Oxford University Press, London, 1975.

[8] B. A. Auld. *Acoustic Fields and Waves in Solids*, volume 1. Krieger Publishing Company, Malabar, Florida, 1990.

[9] L. M. Brekhovskikh and V. Goncharov. *Mechanics of continua and wave dynamics*. Springer, 1985.

[10] P. M. Morse and K. U. Ingard. *Theoretical acoustics*. Princeton University Press, Princeton, 1986.

[11] J. L. Rose. *Ultrasonic Waves in Solid Media*. Cambridge University Press, Cambridge, UK, 1999.

[12] D. Royer and E. Dieulesaint. *Elastic Waves in Solids I - Free and Guided Propagation*, volume 1. Springer, 2000.

[13] P. M. Morse and H. Feshbach. *Methods of theoretical physics*. McGraw-Hill Book Company, 1953.

[14] M. Hayes and M. J. P. Musgrave. On energy flux and group velocity. *Wave Motion*, 1:75–82, 1979.

[15] M. J. S. Lowe. Matrix techniques for modeling ultrasonic waves in multilayered media. *IEEE Transactions on Ultrasonics, Ferroelectrics and Frequency Control*, 42:525–542, 1995.

[16] J. Pochhammer. Über die fortpflanzungsgeschwindigkeiten kleiner schwingungen in einem unbergrenzten isotropen kreiszylinder. *Journal für reine und angewandte Mathematik*, 81:324–336, 1876.

[17] Y.-H. Pao and R. D. Mindlin. Dispersion of flexural waves in elastic, circular cylinder. *Journal of Applied Mechanics*, 27:513–520, 1960.

[18] M. Onoe, H. D. McNiven, and R. D. Mindlin. Dispersion of axially symmetric waves in elastic rods. *Journal of Applied Mechanics*, 29:729–734, 1962.

[19] R. N. Thurston. Elastic waves in rods and clad rods. *Journal of the Acoustical Society of America*, 64:1–37, 1978.

[20] D. C. Gazis. Three dimensional investigation of the propagation of waves in hollow circular cylinders. *Journal of the Acoustical Society of America*, 31(5):568–578, 1959.

[21] J. A. Simmons, E. Drescher-Krasicka, and H. N. G. Wadley. Leaky axisymmetric modes in infinite clad rods i. *Journal of the Acoustical Society of America*, 92:1061–1090, 1992.

[22] M. Viens, Y. Tshukahara, C. K. Jen, and J. D. N. Cheeke. Leaky torsional modes in infinite clad rods. *Journal of the Acoustical Society of America*, 95:701–707, 1994.

[23] M. G. Silk and K. F. Bainton. The propagation in metal tubing of ultrasonic wave modes equivalent to lamb waves. *Ultrasonics*, 17(1):11–19, 1979.

[24] H. M. Bradford. Propagation and spreading of a pulse or wave packet. *American Journal of Physics*, 44(11):1058–1063, 1976.

[25] A. H. Nayfeh. *Wave propagation in layererd anisotropic media with application to composites*. Elsevier, Amsterdam, 1995.

[26] D. N. Alleyne, B. Pavlakovic, M. J. S. Lowe, and P. Cawley. Rapid, long range inspection of chemical plant pipework using guided waves. *Insight*, 43(2):93–96, 2001.

[27] B. N. Pavlakovic, M. J. S. Lowe, and P. Cawley. High-frequency low-loss ultrasonic modes in imbedded bars. *Journal of Applied Mechanics*, 68:67–75, 2001.

[28] M. D. Beard, M. J. S. Lowe, and P. Cawley. Ultrasonic guided waves for the inspection of grouted tendons and bolts. *Journal of Materials in Civil Engineering*, in press, 2002.

[29] B. D. Cullity. *Introduction to magnetic materials*. Addison-Wesley Publishing Company, Reading, Massachusetts, 1972.

[30] J. P. Jakubovics. *Magnetism and magnetic materials*. The Institute of Metals, London, 1987.

[31] F. C. Moon. *Magneto-Solid Mechanics*. Wiley-Interscience, 1984.

[32] G. S. Kino. *Acoustic Waves - Devices, Imaging, and Analog Signal Processing*. Prentice-Hall, Englewood Cliffs, New Jersey, 1987.

[33] W. Boettger, H. Schneider, and W. Weingarten. Tube inspection with an emat system using guided ultrasonic waves. In *4th Conference on NDT 1987*, pages 2305–2313. Pergamon, 1988.

[34] N. S. Tzannes. Joule and wiedemann effects - the simultaneous generation of longitudinal and torsional stress pulses in magnetostrictive materials. *IEEE Transactions on Sonics and Ultrasonics*, SU-13(2):33–41, 1966.

[35] L. C. Lynnworth. *Ultrasonic waveguide experiments booklet*. Panametrics, Inc., 1987.

[36] J. O. Kim, H. H. Bau, Y. Liu, L. C. Lynnworth, S. A. Lynnworth, K. A. Hall, S. A. Jacobson, J. A. Korba, R. J. Murphy, M. A. Strauch, and K. G. King. Torsional sensor applications in two-phase fluids. *IEEE Trans. Ultrason. Ferroelect. Freq. Cont.*, 40(5):563–574, 1993.

[37] L. Laguerre, J.-C. Aime, and M. Brissaud. Magnetostrictive pulse-echo device for non-destructive evaluation of cylindrical steel materials using longitudinal guided waves. *Ultrasonics*, 39:503–514, 2002.

[38] L. C. Lynnworth. *Ultrasonic measurements for process control: theory, techniques, applications*. Academic Press, Inc., San Diego, California, 1989.

[39] J.-C. Aime, M. Brissaud, and L. Laguerre. Spatial analysis of torsional wave propagation in a cylindrical waveguide. application to magnetostrictive generation. *Journal of the Acoustical Society of America*, 109(1):51–58, 2001.

[40] Panametrics Inc. *KT55 Kit*. 221 Cresent Street, Waltham MA, PCI RD Division.

[41] J. Krautkrämer and H. Krautkrämer. *Ultrasonic testing of materials*. Allen and Unwin, London, 1969.

[42] J. M. Allin. *Disbond Detection In Adhesive Joints Using Low-Frequency Ultrasound*. PhD thesis, University of London, 2002.

[43] D. Atkins. *Evaluation of an active acoustic waveguide sensor for embedded structural monitoring*. PhD thesis, University of Strathclyde, 2000.

[44] H. E. Engan. Torsional wave scattering from a diameter step in a rod. *Journal of the Acoustical Society of America*, 104(4):2015–2024, 1998.

[45] A. Demma, P. Cawley, and M.J.S. Lowe. Guided waves in curved pipes. In D. O. Thompson and D. E. Chimenti, editors, *Review of Progress in Quantitative NDE*, volume 21, pages 157–164. American Institue of Physics, New York, 2002.

[46] M. D. Beard. *Guided Wave Inspection of Embedded Cylindrical structures*. PhD thesis, University of London, 2002.

[47] Macro Design Ltd. 16 Palewell Park, East Sheen, London SW14 8JG, UK.

[48] NDT Solutions Ltd. Keele University Science Park, Keele ST5 5SP, UK.

[49] R. Long, K. Vine, M. J. S. Lowe, and P. Cawley. Monitoring acoustic wave propagation in buried cast iron water pipes. In D. O. Thompson and D. E. Chimenti, editors, *Review of Progress in Quantitative NDE*, volume 20, pages 1202–1209. American Institute of Physics, New York, 2001.

[50] P. B. Nagy and R. M. Kent. Ultrasonic assessment of poisson's ratio in thin rods. *Journal of the Acoustical Society of America*, 98(5):2694–2701, 1995.

[51] E. I. Madaras, T. W. Kohl, and W. P. Rogers. Measurement and modeling of dispersive pulse propagation in drawn wire waveguides. *Journal of the Acoustical Society of America*, 97(1):252–261, 1995.

[52] J. O. Kim and H. H. Bau. On line, real-time densimeter - theory and optimization. *Journal of the Acoustical Society of America*, 85(1):432–439, 1989.

[53] C. C. J. Smit and E. D. Smith. The analysis and results of a continuous wave ultrasonic densitometer. *Journal of the Acoustical Society of America*, 104(3):1413–1417, 1998.

[54] R. D. Costley, G. Boudreaux, K. Balasubramaniam, and J. A. Simpson. Waveguide sensor for liquid and slurry properties. In D. O. Thompson and D. E. Chimenti, editors, *Review of Progress in Quantitative NDE*, volume 18, pages 1171–1176. Plenum Press, New York, 1999.

[55] J. O. Kim and H. H. Bau. Instrument for simultaneous measurement of density and viscosity. *Review of Scientific Instruments*, 60(6):1111–1115, 1989.

[56] W. Roth and S. R. Rich. A new method for continuous viscosity measurement. general theory of the ultra-viscoson. *Journal of Applied Physics*, 24(7):940–950, 1953.

[57] R. D. Costley, K. Balasubramaniam, W. M. Ingham, J. A. Simpson, and V. Shal. Torsional waveguide sensor for molten materials. In D. O. Thompson and D. E. Chimenti, editors, *Review of Progress in Quantitative NDE*, volume 17, pages 859–866. Plenum Press, New York, 1998.

[58] J. O. Kim, Y. Wang, and H. H. Bau. The effect of an adjacent viscous fluid on the transmission of torsional stress waves in a submerged waveguide. *Journal of the Acoustical Society of America*, 89(3):1414–1422, 1991.

[59] T.P. Pialucha. *The reflection coefficient from interface layers in NDT of adhesive joints*. PhD thesis, University of London, 1992.

[60] P. B. Nagy and A. H. Nayfeh. Viscosity-induced attenuation of longitudinal guided waves in fluid-loaded rods. *Journal of the Acoustical Society of America*, 100(3):1501–1508, 1996.

[61] Cannon Instrument Company. *VP450 Viscosity Standard*. 2139 High Tech Road, State College, PA, USA.

[62] G. W. C. Kaye and T. H. Laby. *Tables of Physical and Chemical Constants*. Longman, Essex, England, 1995.

[63] E. P. Papadakis. Monitoring the moduli of polymers with ultrasound. *Journal of Applied Physics*, 45(3):1218–1222, 1974.

[64] M. D. Beard, M. J. S. Lowe, and P. Cawley. Development of a guided wave inspection technique for rock bolts. *Insight*, 44(1):19–24, 2002.

[65] B. A. Auld. *Acoustic Fields and Waves in Solids*, volume 2. Krieger Publishing Company, Malabar, Florida, 1990.

[66] P. J. Torvik. Reflection of wave trains in semi-infinite plates. *Journal of the Acoustical Society of America*, 41(2):346–353, 1967.

[67] J. J. Ditri. Some results on the scattering of guided elastic sh waves from material and geometric waveguide discontinuities. *Journal of the Acoustical Society of America*, 100(5):3078–3087, 1996.

[68] E. Le Clézio, M. Castaings, and B. Hosten. Réflexion d'ondes de lamb à l'extrémité de plaque: solution analytique et mesures. In *Proceedings of the 5th Congrès Français d'Acoustique*, pages 177–180, 2000.

[69] J. Zemanek. An experimental and theoretical investigation of elastic wave propagation in a cylinder. *Journal of the Acoustical Society of America*, 51(1):265–283, 1972.

[70] J. J. Ditri. Utilization of guided elastic waves for the characterization of cirumferential cracks in hollow cylinders. *Journal of the Acoustical Society of America*, 96(6):3769–3775, 1994.

[71] H. Bai, A. H. Shah, N. Popplewell, and S. K. Datta. Scattering of guided waves by circumferential cracks in steel pipes. *Journal of Applied Mechanics*, 68:619–631, 2001.

[72] D. N. Alleyne, M. J. S. Lowe, and P. Cawley. The reflection of guided waves from circumferential notches in pipes. *Journal of Applied Mechanics*, 65:635–641, 1998.

[73] M. J. S. Lowe, D. N. Alleyne, and P. Cawley. The mode conversion of a guided wave by a part-circumferential notch in a pipe. *Journal of Applied Mechanics*, 65:649–656, 1998.

[74] D. N. Alleyne and P. Cawley. The interaction of lamb waves with defects. *IEEE Trans. Ultrason. Ferroelectr. Freq. Control*, 39:381–397, 1992.

[75] P. Kirrmann. On the completeness of lamb modes. *Journal of Elasticity*, 37(1):39–69, 1994.

[76] J. E. Murphy, G. Li, and S. A. Chin-Bing. Orthogonality relation for rayleigh-lamb modes of vibration of an arbitrarily layered elastic plate with and without fluid loading. *Journal of the Acoustical Society of America*, 96(4):2313–2317, 1994.

[77] R. Briers, O. Leroy, G. N. Shkerdin, and Yu. V. Gulyaev. Mode theory as a framework for the investigation of the generation of a stonely wave at a liquid-solid interface. *Journal of the Acoustical Society of America*, 95(4):1953–1966, 1994.

[78] D. Hitchings. *FE77 User Manual*. Imperial College, London, 1994.

[79] O. C. Zienkievicz. *The Finite Element Method in Engineering Science*. McGraw-Hill, New York, 1971.

[80] H. J. Bathe. *Finite Element Procedures in Engineering Analysis*. Prentice Hall Inc., New York, 192.

[81] B. J. Hunt and M. I. James. *Polymer Characterisation*. Blackie Academic and Professional, London, England, 1993.

[82] S. Dixon, C. Edwards, and S. B. Palmer. Experiment to monitor adhesive cure using electromagnetic acoustic transducers. *Insight*, 37(12):969–973, 1995.

[83] R. T. Harrold and Z. N. Sanjana. Theoretical and practical aspects of acoustic waveguide cure monitoring of composite materials. In *31st International SAMPE Symposium*, pages 1713–1723, 1986.

[84] R. T. Harrold, Z. N. Sanjana, and R. Brynsvold. Acoustic waveguide cure curves for materials ranging from fast cure resins to slow cure concrete. In D. O. Thompson and D. E. Chimenti, editors, *Review of Progress in Quantitative NDE*, volume 15, pages 2297–2304. Plenum Press, New York, 1996.

[85] Y. Li, G. J. Posakony, and S. M. Menon. Monitoring the cure process of polymer composites and neat resin using an ultrasonic wire waveguide technology. In *43rd International SAMPE Symposium*, pages 937–948, 1998.

[86] G. A. Sofer and E. A. Hauser. Polymerization of thermosetting polymers. *Journal of Polymer Science*, 8(6):611–620, 1952.

[87] J. H. Speake, R. G. C. Arridge, and G. J. Curtis. Measurement of the cure of resins by ultrasonic techniques. *Journal of Physics D: Applied Physics*, 7:412–424, 1974.

[88] J. F. W. Bell. A solid acoustic thermometer. *Ultrasonics*, 6(1):11–14, 1968.

[89] A. M. Lindrose. Ultrasonic wave and moduli changes in a curing epoxy resin. *Experimental Mechanics*, 18:227–232, 1978.

[90] S. I. Rohklin, D. K. Lewis, K. F. Graff, and L. Adler. Real-time study of frequency dependence of attenuation and velocity of ultrasonic waves during the curing reaction of epoxy resin. *Journal of the Acoustical Society of America*, 79(6):1786–1793, 1986.

[91] R. E. Challis, R. P. Cocker, A. K. Holmes, and T. Alper. Viscoelasticity of thin adhesive layers as a function of cure and service temperature measured by a novel technique. *Journal of Applied Polymer Science*, 44:65–81, 1992.

[92] A. Maffezzoli, E. Quarta, V. A. M. Luprano, G. Montagna, and L. Nicolais. Cure monitoring of epoxy matrices for composites by ultrasonic wave propagation. *Journal of Applied Polymer Science*, 73:1969–1977, 1999.

[93] D. D. Shepard and K. R. Smith. A new ultrasonic measurement system for the cure monitoring of thermosetting resins and composites. *Journal of Thermal Analysis*, 49:95–100, 1997.

[94] W. G. McDonough, B. M. Fanconi, F. I. Mopsik, and D. L. Hunston. A role of cure monitoring techniques for on-line process control. In *6th Proceedings of Annual ASM/ESD Advanced Composites Conference*, pages 637–644, 1990.

[95] E. A. Arvay. Aspects of adhesive cure monitoring. In *26th International SAMPE Symposium*, pages 115–125, 1980.

[96] F. I. Mopsik, S. S. Chang, and D. L. Hunston. Dielectric measurements for cure monitoring. *Materials Evaluation*, 47:448–453, 1989.

[97] B. G. Martin. Monitoring the composite cure cycle by dielectric analysis. *Materials Evaluation*, 34:49–54, 1976.

[98] D. E. Kranbuehl, S. E. Delos, and P. K. Jue. Dielectric properties of the polymerization of an aromatic polyimide. *Polymer*, 27:11–18, 1986.

[99] D. J. Dare and D. L. Chadwick. A low resolution pulsed nuclear magnetic resonance study of epoxy resin during cure. *International Journal of Adhesion and Adhesives*, 16(3):155–163, 1996.

[100] G. R. Powell, P. A. Crosby, D. N. Waters, C. M. France, R. C. Spooncer, and G. F. Fernando. In-situ cure monitoring using optical fibre sensors - a comparative study. *Smart Materials and Structures*, 7:557–568, 1998.

[101] R. Lovell and A. H. Windle. Waxs investigation of local structure in epoxy networks. *Polymer*, 31:593–601, 1990.

[102] A. Bernard, M. J. S. Lowe, and M. Deschamps. Guided waves energy velocity in absorbing and non-absorbing plates. *Journal of the Acoustical Society of America*, 110(1):186–196, 2001.

List of Publications

T. Vogt, M. J. S. Lowe, P. Cawley. Cure monitoring using ultrasonic guided waves in wires. In D. O. Thompson and D. E. Chimenti, editors, *Review of Progress in Quantitative NDE*, volume 20, pages 1642–1649. American Institute of Physics, New York, 2001.

T. Vogt, M. J. S. Lowe, P. Cawley. Ultrasonic waveguide techniques for the measurement of material properties. In D. O. Thompson and D. E. Chimenti, editors, *Review of Progress in Quantitative NDE*, volume 21, pages 1742–1749. American Institute of Physics, New York, 2002.

T. Vogt, M. J. S. Lowe, P. Cawley. The scattering of guided waves in partly embedded cylindrical structures. *Journal of the Acoustical Society of America*, 2002, in press.

T. Vogt, M. J. S. Lowe, P. Cawley. Cure monitoring using ultrasonic guided waves in wires. Submitted to the *Journal of the Acoustical Society of America*, May 2002.

T. Vogt, M. J. S. Lowe, P. Cawley. The scattering of ultrasonic guided waves in partly embedded cylindrical structures. Submitted for publication in D. O. Thompson and D. E. Chimenti, editors, *Review of Progress in Quantitative NDE*. American Institute of Physics, New York, August 2002.

T. Vogt, M. J. S. Lowe, P. Cawley. Measurement of the material properties of viscous liquids using ultrasonic guided waves. Submitted to *IEEE Transactions on Ultrasonics, Ferroelectrics, and Frequency Control*, October 2002.

T. Vogt, M. E. Unwin, M. J. S. Lowe, P. Cawley, R. E. Challis. A comparison of ultrasonic compression wave techniques applied to the monitoring of cure in thermosets, in preparation.